Development of a tip-enhanced Raman spectrometer to investigate solid-liquid interfaces

Dissertation
zur Erlangung des Grades
Doctor der Naturwissenschaften
im Promotionsfach Chemie

am Fachbereich Chemie, Pharmazie und Geowissenschaftern
der Johannes Gutenberg-Universität Mainz

Leonie Driessen

geb. in Deurne

Mainz, 2018

1. Gutachter:
2. Gutachter:

Tag der Prüfung: 18.12.2018

I hereby declare that I wrote the dissertation submitted without any unauthorized external assistance and used only sources acknowledged in the work. All textual passages which are appropriated verbatim or paraphrased from published and unpublished texts as well as all information obtained from oral sources are duly indicated and listed in accordance with bibliographical rules. In carrying out this research, I complied with the rules of standard scientific practice as formulated in the statutes of Johannes Gutenberg-University Mainz to insure standard scientific practice.

Abstract

Plenty of bio-medical and industrially relevant processes take place at solid-liquid interfaces. The mechanisms underlying these macroscale solid-liquid interfacial processes are at the molecular scale, i.e. molecules (and/or ions) in the liquid phase interact with atoms or molecules at the solid surface. This dissertation discusses the development of a tip-enhanced Raman spectroscopy (TERS) setup to probe molecules and their interactions with the environment at solid-liquid interfaces. TERS is a surface-sensitive technique that is not only sensitive to small numbers of molecules with a nanometric lateral spatial resolution, but also provides chemical specificity enabling identification of molecules and probing of their interactions with their environment. Furthermore, TERS enables *in situ* investigation of molecules at room temperature, in ambient atmosphere and under atmospheric pressure.

The home-designed solid-liquid TER spectrometer enables the investigation of molecules at the surface of opaque substrates under a 6.6 mm thick layer of water. The TER spectrometer can obtain TERS maps, of which the lateral spatial resolution is 12.6 nm (measured in air).

Solid-liquid TERS has been applied to investigate the interaction between benzene-1,3,5-tricarboxylic acid (BTC) and a monolayer of Cu/Au in air and under water. Spectral changes in TER spectra were observed upon immersing the BTC/Cu/Au substrate in water. The observed spectral changes suggest a change in binding geometry of BTC on the Cu/Au substrate upon water immersion.

The results discussed in this thesis show that the developed solid-liquid TER spectrometer can be used to investigate ensembles of molecules at Au-water interfaces. Further technical improvements will enable the general use of solid-liquid TERS for nanometric investigation of molecules at solid-liquid interfaces.

Zusammenfassung

An fest-flüssig Grenzflächen finden viele biomedizinisch und industriell relevante Prozesse statt. Die Mechanismen, die diesen makroskopischen Prozessen zugrundeliegen, finden auf mikroskopischer Ebene statt. Das heißt, dass Moleküle (und/oder Ionen) in der flüssigen Phase mit Atomen oder Molekülen an der festen Oberfläche interagiern. In dieser Dissertation wird die Entwicklung eines spitzenverstärkten Raman-Spektroskops (TERS) für die Untersuchung von Molekülen und deren Interaktion mit der Umwelt an fest-flüssig Grenzflächen diskutiert. TERS ist eine oberflächensensitive Methode, die in der lage ist eine sehr geringe Menge an Molekülen, mit einer lateralen Auflösung im nanometer Bereich, zu detektieren. Des Weiteren ist es mit dieser Methode, aufgrund der chemischen Spezifität, möglich Moleküle zu identifizieren und ihre Interaktionen mit der Umgebung zu untersuchen. TERS ermöglicht die Untersuchung von Molekülen bei Raumtemperaur, in Umgebungsatmosphäre und bei Luftdruck.

Das maßangefertigte fest-flüssig TER Spektrometer erlaubt die Untersuchung von Molekülen an der Oberfläche von undurchsichtigen Substraten unter einem Wasserfilm mit einer Schichtdicke von 6.6 mm. Des Weiteren können TERS Karten mit einer lateralen Auflösung von 12.6 nm erstellt werden (an Luft gemessen).

Fest-flüssig TERS wurde angewandt um die Interaktion zwischen 1,3,5-Tricarboxybenzen (BTC) und einer Monolage von Kupfer/Gold an Luft und in Wasser zu untersuchen. Durch die Zugabe von Wasser zu dem BTC/Cu/Au Substrat wurden spektrale Änderungen der TERS Spekren beobachtet. Diese Änderungen deuten darauf hin, dass sich die Bindungsgeometrie des BTC Moleküls auf dem Cu/Au Substrat durch das Eintauchen in Wasser ändert.

Die Ergebnisse, die in dieser Arbeit diskutiert werden zeigen, dass das entwickelte fest-flüssig TERS Spektrometer zur Untersuchung von Molekülen an der Au-Wasser Grenzfläche verwendet werden kann. Weitere technische Verbesserungen werden eine weitgreifendere Verwendung des fest-flüssig TERS für Untersuchungen von Molekülen an der Grenzfläche von fest-flüssig Grenzflächen im Nanometerbereich ermöglichen.

Contents

1. Introduction

1.1. Motivation of this work

Solid-liquid interfaces play an important role for plenty bio-medical and industrially relevant processes, e.g. adsorption of (bio)molecules to sensors [1, 2], biofouling on biomedical implants [3], photocatalysis [4], electrocatalysis [5] or electrochemical synthesis of materials [6]. The mechanisms underlying these macroscale solid-liquid interfacial processes are at the molecular scale, i.e. molecules (and/or ions) in the liquid phase interact with atoms or molecules at the solid surface. Many solid-liquid interfacial processes depend on nanoscale structure-activity relationships, e.g. atomic-scale metal structures form active sites for electrocatalysis [5]. Rational design of functional solid-liquid interfaces requires understanding of interfacial molecular processes and nanoscale structure-activity relationships. Ideally, a tool should exist that can be used to probe solid-liquid interfaces at the molecular scale. This tool should fulfill the following specifications:

- **High sensitivity** to detect very low concentrations of molecules at solid-liquid interfaces.

- **Chemical specificity** to identify molecules and probe their interactions with the environment, such as binding to a solid substrate or hydrogen-binding to surrounding water molecules.

- **Surface-sensitivity** to only probe molecules close to or interacting with the solid surface and distinguish them from the bulk contributions of the solid and liquid phases.

- **Nanometric lateral spatial resolution** to distinguish laterally displaced (ensembles of) molecules and to image nanoscale structures at the solid surface.

- Probe molecules at solid-liquid interfaces ***in situ***, which means **under real working conditions** concerning temperature, pressure and surface potential, to study characteristics of molecules in everyday conditions.

Many tools have been developed to investigate molecular processes at solid-liquid interfaces. A technique that is highly sensitive to adsorption of molecules to a solid-liquid interface is surface plasmon resonance (SPR) spectroscopy [7]. SPRs in a thin metallic substrate are changed upon variations in the refractive index of the medium just outside the metal film, e.g. by adsorption of molecules to the metal film [8]. Changes in SPR can be read out by the changes in reflectivity of an incident light beam. However, this technique lacks chemical specificity, because the change of the optical properties of the thin metal substrate is insensitive to what chemical species adsorb to its surface. A way to include chemical specificity is coating the metal substrate with specific binding sites for target molecules [7]. With this approach the technique can be used for sensing and for the investigation of biomolecular interactions. SPR spectroscopy has micrometer lateral spatial resolution, and thereby lacks the nanometric lateral spatial resolution we are aiming for.

Another widely used technique to investigate solid-liquid interfaces is cyclic voltammetry (CV) [9]. CV probes surface reactions involving electron transfer. These reactions involve atoms of the solid surface itself, chemical species from the liquid phase and/or chemical species adsorbed to the surface. In CV the entire electrified surface is probed. Spatial resolution can be improved by using a scanning electrochemical microscope (SECM) [10]. In SECM an ultramicroelectrode is approached to a surface to locally perform CV measurements. The surface area probed by the ultramicroelectrode is in the sub-µm scale, substantially larger than the targeted nanometric resolution in our study. Furthermore, in general, the probed electrochemical behavior of chemical species (e.g. adsorption state to a charged surface or reaction rate of electrochemical reactions) can not be used to identify unknown chemical species. Therefore CV does not provide the chemical specificity we are looking for. It is therefore common practice to combine CV with other methods which have chemical specificity, such as vibrational spectroscopy.

A technique that has both molecular sensitivity and nanometric spatial resolution is fluorescence microscopy. The recent development of several super-resolving fluorescence microscopy techniques, such as stimulated emission depletion microscopy (STED) [11], photo-activated localization microscopy (PALM) [12] and stochastic optical reconstruction microscopy (STORM) [13], was a breakthrough in microscopy for which the 2014 Nobel Prize in Chemistry was awarded. Super-resolving fluorescence microscopy enables far-field microscopy of single fluorescent molecules (fluorophores), with spatial resolutions far below the Abbe diffraction limit. To broaden the applicability of fluorescence microscopy to other species than fluorophores, it is common practice to label (bio)molecules with a fluorescent tags. Adding a fluorescent tag to a molecule brings along the risk of altering the molecule's properties. Furthermore, unlabeled or unknown species in a system go unnoticed in fluorescence microscopy. Therefore fluorescence microscopy does not fulfill the chemical specificity requirement of the tool we are looking for.

Surface science techniques have gained thorough understanding in many nanoscale processes on solid surfaces. However, the majority of surface science techniques are applied under ultrahigh vacuum (UHV) where the influence of the liquid phase on surface processes is excluded. Therefore, surface studies under UHV conditions do not render the same result as processes taking place at solid-liquid interfaces [14]. Several surface science techniques can be applied at (electrified) solid-liquid interfaces [15, 16, 17, 18].
Scanning tunneling microscopy (STM) and atomic force microscopy (AFM) are scanning probe microscopy (SPM) techniques, in which a tip (STM) or cantilever (AFM) with a nanoscale apex probes local density of states underneath the apex of the tip or force between cantilever and sample, respectively [19, 20]. At solid-liquid interfaces the lateral spatial resolution of both techniques can go down to atomic level [21, 22]. However,

in general the extracted local electronic structure or local mechanical properties of a substrate can not be used to identify molecules or the interaction of molecule with their environment.

In transmission electron microscopy (TEM), investigations of solid-liquid interfaces have been enabled by using a hermetically sealed sample cell to prevent evaporation of the liquid inside the high vacuum chamber [23, 17]. TEM uses electrons to probe the structure of nanoscale objects. This technique is usually combined with energy dispersive X-ray spectroscopy (EDS) [24] or electron energy loss spectroscopy (EELS) [25] to probe elemental distribution of the sample. Because of the transmission geometry in TEM, the liquid phase and sample cell need to be electron-transparent. Electron-transparancy is achieved by making the sample very thin: the liquid layer is several µm thick and the sample cell is formed of thin membranes (e.g. of graphene or SiN_x) [17]. A problem in solid-liquid TEM is that the interaction of the electron beam with the solvent can lead to the generation of radiolytic species. Radiolytic species might be highly reactive, such as free radicals, perturbing the sample and sample cell. Furthermore, organic species generally have a bad contrast in TEM, which hinders imaging of organic molecules.

Several X-ray spectroscopies have been adapted to study solid-liquid interfaces [18]. X-ray spectroscopies, such as X-ray absorption spectroscopies (XAS) and X-ray photoemission spectroscopy (XPS), use X-ray photons to excite core-level electrons into valence orbitals or continuum states. The information obtained can be analyzed to obtain information about the chemical environment of the elements under study. Solid-liquid X-ray studies are scarce, because they are mostly based on synchrotron radiation. Furthermore, X-rays and high kinetic energy electrons used in X-ray techniques might damage the surface and molecules under study [18]. X-ray core-level spectroscopies have a sub-nm depth resolution, but their lateral resolution is in the µm-range.

Vibrational spectroscopic techniques can be used to identify molecules and characterize their interaction with the environment by their unique vibrational 'fingerprint', and therefore have chemical specificity. Furthermore, several vibrational spectroscopies, such as infrared reflection absorption spectroscopy (IRRAS) [26], surface-enhanced infrared absorption (SEIRAS) [27], vibrational sum frequency spectroscopy (SFG) [28], surface-enhanced Raman spectroscopy (SERS) [29] and tip-enhanced Raman spectroscopy (TERS) [30], are solid-liquid surface-sensitive. However, in the cases when IR light is used, the investigation of solid-liquid interfaces becomes difficult. Many chemical species, such as water and many solids, strongly absorb IR light. Therefore large portions of IR light are absorbed by penetrating through millimeters of solids or through millimeters of liquid, severely complicating IR spectroscopy at solid-liquid interfaces. IR absorption spectroscopy at solid-water interfaces is only possible with specific technical designs to diminish IR absorption by the environment, such as using a thin layer of water (micrometers thick), an even thinner layer of IR-absorbing solid (nanometers thick) or choosing a solid that is transparent for IR light. In Raman spectroscopy the wavelength of the incoming laser light does not need to match with the energy levels of the probed molecules. Therefore, the wavelength of the laser light can be chosen such that the interaction with the environment is minimal, making Raman spectroscopy at solid-water interfaces feasible. Raman spectroscopy can be performed at solid-liquid interfaces after passing a millimeters thick water layer. Surface-enhanced Raman spectroscopy probes vibrational energies of molecules typically within ~10 nm of a rough(ened) metal substrate. However, this technique lacks nanometric lateral spatial resolution. In tip-enhanced Raman spectroscopy, vibrational energies of chemical species present in the nanometric area underneath the apex of a metallic SPM tip or cantilever are probed. TERS generally has a lateral spatial resolution lower than 10 nm.

In the need for a new technique for label-free *in situ* nanoscale investigation of molecular processes at solid-liquid interfaces we have developed a solid-liquid tip-enhanced Raman spectrometer. Solid-liquid tip-enhanced Raman spectroscopy (S/L-TERS) is capable of retrieving the chemical 'fingerprint' of molecules at solid-liquid interfaces with nanometric lateral spatial resolution. In TERS, light is focused at the apex of a tip. This leads to an enhanced EM near-field underneath the apex of the tip. The Raman scattering signal of molecules in the near-field is enhanced by several orders of magnitude

1.2. Thesis outline

The first part of this dissertation is committed to the description of the technical development of the solid-liquid TER spectrometer: **chapter 2** contains the theoretical background of solid-liquid TERS and the considerations behind choices of experimental conditions used in the solid-liquid TERS setup. **Chapter 3** contains the technical details of the solid-liquid TERS setup and measurement procedure. In the second part of this dissertation, the solid-liquid TER spectrometer is applied to investigate molecules at interfaces. In **chapter 4** TERS results are presented to highlight characteristics of the TERS setup concerning spatial resolution and TERS mapping in air. In **chapter 5** the solid-liquid TER spectrometer is applied to investigate the nucleation and growth of an archetypical metal-organic framework ('CuBTC', consisting of Cu centers linked by benzene-1,3,5-carboxyl) on a metal substrate. In **chapter 6** an outlook on solid-liquid TERS is provided and technical improvements for solid-liquid TERS are proposed.

2. Theory

This chapter is dedicated to the theoretical background of solid-liquid tip-enhanced Raman spectroscopy (S/L TERS). To shorten this chapter to the essence, only those topics that have a practical implication for S/L TERS are discussed. The principles of TERS can to a large extent be explained by the principles of surface-enhanced Raman spectroscopy (SERS). For the interested reader, a thorough and mathematical approach to the Raman effect can be found in the general textbook written by D.A. Long [31], and principles of surface-enhanced Raman spectroscopy have been tackled in detail by E.C. le Ru and P.G. Etchegoin [32].

2.1. Raman spectroscopy

2.1.1. Raman scattering

Raman spectroscopy is a vibrational spectroscopy based on Raman scattering. The discovery of Raman scattering was made by C.V. Raman, for which he gained the 1930 Nobel Prize in Physics. Today Raman spectroscopy is an ubiquitous tool in analytical chemistry to characterize materials as diverse as food, art, biomolecules or minerals [31].

When light interacts with a molecule, approximately one in 10^6 incident photons are Raman scattered [33]. In Raman scattering an incident photon interacting with a molecule is inelastically scattered with either more or less energy than the incident photon, depending on the vibrational energy state of the molecule. If an incident photon interacts with a molecule in its vibrational ground state $v = 0$, there is a chance that the molecule is excited to a vibrational energy state $v = 1,2...$ In this process, called Stokes Raman scattering, the energy difference between the incident and scattered photon is the vibrational energy of the molecule $E_{vib} = E_L - E_S$. When a photon interacts with a molecule in an excited vibrational state, there is a chance that the molecule falls back in its vibrational ground state. In this process, called anti-Stokes Raman scattering, the energy of the scattered photon is increased compared to the energy of the incident photon and $E_{vib} = E_S - E_L$. In figure 2.1 simplified Jablonski diagrams are shown for Stokes Raman scattering, anti-Stokes Raman scattering and elastic Rayleigh scattering. Rayleigh and Raman scattering processes can be visualized in a Jablonski diagram by adding a virtual energy state. Note that scattering is an instantaneous process. Therefore, the virtual energy state in the Jablonski diagram is not a real physical state of the molecule, but rather a quantum mechanical picture of the working principle of Rayleigh and Raman scattering.

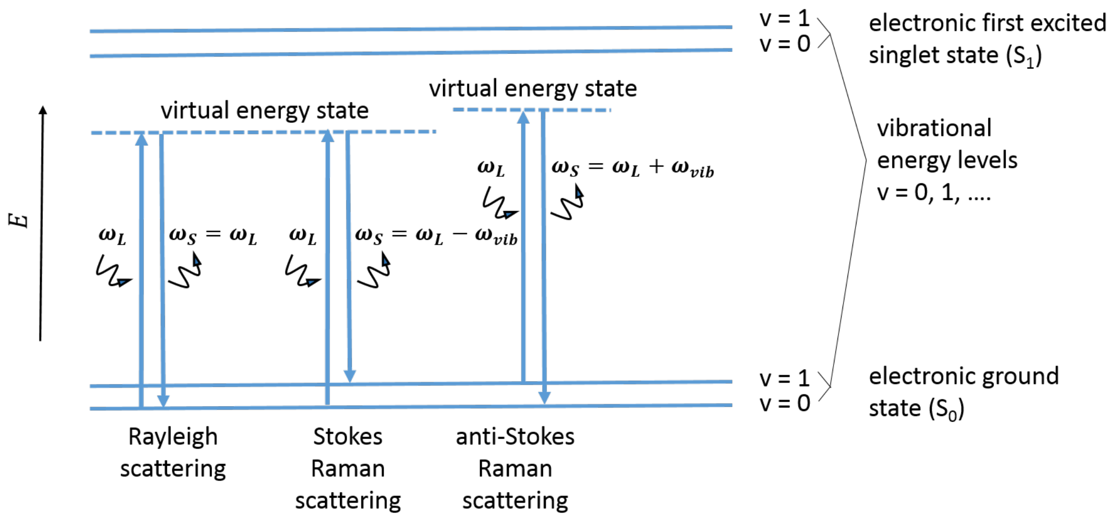

Figure 2.1.: Simplified Jablonski diagrams of elastic scattering (left) and inelastic scattering (center and right). In inelastic scattering, interaction of incident light with a molecule leads to excitation of a molecule from its vibrational ground state $v = 0$ to its vibrational energy state $v = 1,2...$ (Raman scattering), or from its vibrational energy state $v = 1,2...$ to its vibrational ground state $v = 0$ (anti-Stokes scattering).

2.1.2. Raman cross-sections

How strong an object, e.g. a molecule, interacts with light can be quantitative described by the cross section of an optical process. The cross-section σ [m^2] relates the incident power density S_{Inc} [W m^{-2}] at the molecule position to the power (or intensity) of the optical process P [W] [32]:

$$P = \sigma S_{Inc} \tag{2.1}$$

For a scattering process, the cross section has an angular dependency. The angular dependency of Raman scattering has to be taken into account in the definition of the Raman cross-section, because in common Raman spectrometers an objective is used for the detection of scattered radiation. This objective is placed along a certain angle in respect to the sample, thereby only detecting part of the total scattered radiation. The variable $\Omega \equiv (\theta, \phi)$ [sr] contains the two angles necessary to define the direction of scattered radiation in respect to the incident beam direction. The angular dependent scattered power, called the differential scattered power $dP_{Sca}/d\Omega$ [W sr^{-1}], is defined by:

$$\frac{dP_{Sca}}{d\Omega}(\Omega) = \frac{\sigma_{Sca}}{d\Omega}(\Omega) S_{Inc} \tag{2.2}$$

The Raman cross-section of a molecule interacting with incident light depends on the polarizability of the molecule. Polarizability of a molecule can be defined using the classical electromagnetic (EM) theoretical description of the Raman effect. The oscillating electric field of EM radiation interacts with electrons in a molecule, thereby inducing an oscillating dipole moment in the molecule [33]. Polarizability is the proportionality factor relating the magnitude of the induced dipole moment $\vec{\mu}$ [C m] to the strength of the incident EM field $\vec{E}$ [V m^{-1}] [33]:

$$\vec{\mu} = \alpha\vec{E} \tag{2.3}$$

where α [ϵ_0 m^3] is the second-rank Raman polarizability tensor for a specific vibrational mode of the molecule. Polarizability is a measure of the ease of deformation of the electron cloud around an atom or in a molecule.

We will now study the influence of a molecular vibration to α. For this, we will focus one specific normal mode k, which is a vibrational pattern where all atoms in a molecules oscillate at the same frequency ω_k. Q_k(t) [kg$^{1/2}$m] is a single scalar describing atomic displacements from the equilibrium position Q_0 in normal coordinates of all atoms of a molecule for normal mode k. Vibrations of a molecule induce small perturbations of the molecular structure, and thereby also of the polarizability of the molecule. Small perturbations of the polarizability can be approximated by a Taylor expansion:

$$\alpha_k = \alpha_0 + \left(\frac{\partial\alpha}{\partial Q_k}\right)_{Q_k=0} Q_k + ... \tag{2.4}$$

where α_0 is the polarizability at equilibrium and the following term is the first-order perturbation of the polarizability by atomic movements. Second- and further order perturbations are neglected in equation 2.4 (electrical harmonic approximation [32]).

We add time dependence of Q_k, assuming simple harmonic oscillation:

$$Q_k = Q_k^0 \; cos(\omega_k t) \tag{2.5}$$

We add frequency dependence of E:

$$\vec{E} = \vec{E}_0 \; cos(\omega_L t) \tag{2.6}$$

Placing equations 2.4, 2.6 and 2.5 into equation 2.3 and defining $\alpha'_k = \left(\frac{\partial\alpha}{\partial Q_k}\right)_{Q_k=0}$ gives:

$$\vec{\mu} = (\alpha_0 + \alpha'_k \; Q_k^0 \; cos(\omega_k t)) \; \vec{E}_0 \; cos(\omega_L t) \tag{2.7}$$

Using trigonometric identity, equation 2.7 becomes:

$$\vec{\mu} = \alpha_0 \; \vec{E}_0 \; cos(\omega_L t) + \frac{1}{2}\alpha'_k \; Q_k^0 \; \vec{E}_0 \; cos((\omega_k + \omega_0)t) + \frac{1}{2}\alpha'_k \; Q_k^0 \; \vec{E}_0 \; cos((\omega_k - \omega_0)t) \tag{2.8}$$

Equation 2.8 shows the three processes leading to the induced dipole $\vec{\mu}$: the first term leads to Rayleigh scattering with frequency $(\omega_L t)$, the second term leads to Stokes scattering with frequency $\omega_k + \omega_0)t$ and the last term leads to anti-Stokes scattering with frequency $\omega_k - \omega_0)t$. Furthermore, from equation 2.8, it becomes clear that a change in the polarizability ($\alpha'_k \neq 0$) of a molecule by a vibration is a requirement for Stokes and anti-Stokes Raman scattering, i.e. a Raman selection rule. In certain cases, for individual vibrations $\alpha'_k \neq 0$, but due to symmetry of the molecule, the overall change in polarizability is canceled out. The molecules probed by TERS which are presented in this thesis are larger molecules, in which usually for all of their vibrational modes $\alpha'_k \neq 0$ and therefore all vibrational modes are Raman-active. Another molecule discussed in this thesis, water, is small, but not linear and therefore all its vibrations are Raman-active.

As a consequence of the tensorial nature of the polarizability, the light-induced change in polarizability can be different along the various axes of the molecular structure. This means that the Raman cross section depends on both the intrinsic polarizability tensor and the orientation of the molecule or chemical bond with respect to the direction of the incident electric field. In conventional Raman spectroscopy, this effect is in particular important for the interpretation of Raman spectra of materials which present a high degree of order due to the fixed orientations of molecules or atoms [32]. For example, changing the angle of incidence of linear polarized light in Raman spectroscopy of graphene changes the scattered Raman signal and ratio of the raman bands of its phonon modes [34].

Another effect on the Raman cross-section is the resonance condition of a molecule. If a molecule is resonant with the frequency of the incident light, the probability for Raman scattering increases. The resonance condition of a molecule is met when the virtual energy state corresponds to a physical energy state of the molecule. The resonance condition of a molecule leads to a at least four orders of magnitude larger differential Raman cross-section [32]. This thesis does not contain resonant Raman spectroscopy results.

Stokes Raman scattering of a molecule has a larger cross-section than anti-Stokes Raman scattering, because the probability to find a molecule at its electronic ground state S_0, $v = 0$ is higher than at a vibrational energy level S_0, $v > 0$. In this thesis we will only discuss Stokes Raman scattering.

Furthermore, the detected intensity of a Raman scattering signal depends on the number of scatterers (molecules) in the laser focus and on the characteristics of the Raman spectrometer, such as efficiency of the detector, optical alignment and background light.

2.1.3. Interpretation of Raman spectra

In Raman spectroscopy scattered photons are detected as counts on a camera. A grating is used to lead the photons with different energies to different positions on a line on the chip of the camera. In this way a Raman spectrum can be read out, with photon energy on the X-axis and counts on the Y-axis. In both Stokes and anti-Stokes Raman scattering, the difference in energy between the scattered photon and the incident photon is called Raman shift. Monochromatic light is used for excitation, to be able to calculate Raman shifts from the detected scattered photon energies. Usually narrow-bandwidth lasers are used as light source in Raman spectroscopy, because they produce monochromatic light with a high power density. Raman shifts are traditionally plotted in wavenumbers, $\bar{v}$ [cm^{-1}]. The Raman shift of scattered photons is calculated by:

$$\frac{1}{\lambda_L} - \frac{1}{\lambda_S} = \bar{v} \tag{2.9}$$

where λ_L [cm] is the wavelength of the incident photons and λ_S [cm] is the wavelength of the scattered photons. The Raman shift of Stokes scattering is positive and the Raman shift of anti-Stokes scattering is negative because for Stokes Raman scattering $\lambda_S > \lambda_L$

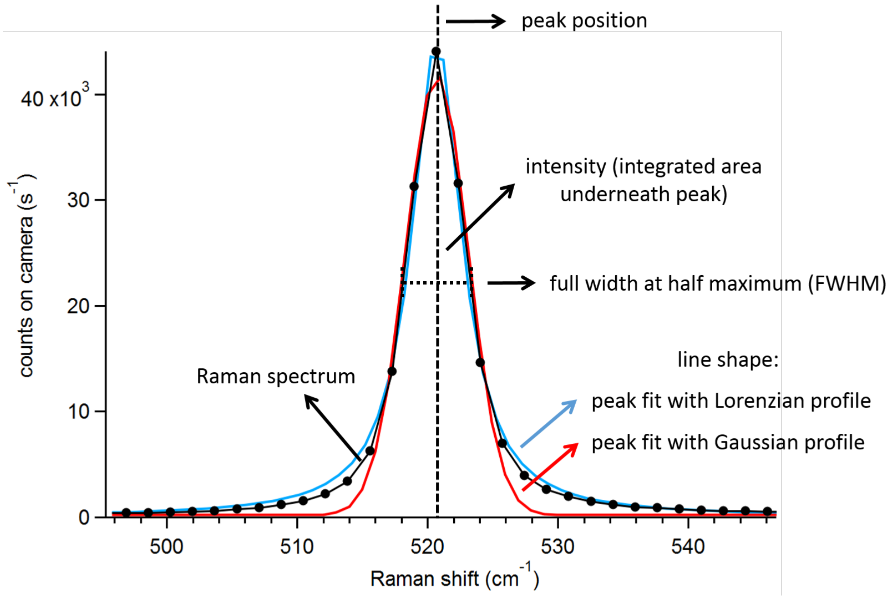

Figure 2.2.: Raman peak characteristics are visualized in a Raman spectrum of a Si wafer: central peak position, intensity, FWHM and line shapes of peak fits.

while for anti-Stokes Raman scattering $\lambda_S < \lambda_L$.
Raman spectroscopy can access a broad energy range, of which the region of 30 - 3600 cm^{-1} is of most interest for the majority of users, because this range covers vibrational modes of molecules and phonon modes of solids [35]. Practically, the lower limit of a Raman spectrum depends on the spectrometer design. In a Raman spectrometer Rayleigh scattered photons are filtered out of the scattered radiation to only detect Raman scattered photons. This is necessary, because the orders of magnitude larger Rayleigh scattering would overfill the sensitive detectors used for Raman spectroscopy and thereby hide the weak Raman scattering signal. The edge or notch filter used to filter out the Rayleigh scattering (and depending on the sample and illumination/detection configuration also reflected light) cuts off the lowest wavenumber region of Raman spectra (position of spectral 'cut-off' depends on filter, usually at about 200 cm^{-1} [35]).

Raman-active vibrational modes of a molecule show up in a Raman spectrum as peaks. The characteristics of the peaks, i.e. (center) position, full width at half maximum (FWHM) and intensity (see figure 2.2), can be used to characterize molecular vibrations and their interactions with the environment, and coherent collective vibrations (i.e. phonons) in solids. A molecular vibration can be modeled as a harmonic oscillator. A harmonic oscillator consists of a particle that experiences a restoring force F when it is displaced from its equilibrium position by distance x:

$$F = -kx \tag{2.10}$$

where k is the force constant (the stiffer the spring, the larger k). Substitution of equation 2.11 into Newton's equation leads to a differential equation of which a solution is:

$$\begin{aligned} x(t) &= Asin(\omega t) \\ \omega &= (k/m)^{1/2} \end{aligned} \tag{2.11}$$

where A is the amplitude of the motion, ω is the angular frequency and m is the mass of the particle. The frequency of the particle is $\nu = \omega/2\pi$. A stronger bond (for example C=C is stronger than C-C) or heavier atoms involved (for example C-Cl is heavier than C-H) both lead to a higher stretching frequency or Raman shift [36]. Interactions of the molecule with its environment can influence the frequency of (some of) the molecule's vibrations. For example, hydrogen-bonding of a carboxyl side group to surrounding water molecules decreases its C=O stretching frequency as the C=O bond is weakened [36].

The reason for broadening of peaks in a vibrational spectrum is the interaction of the molecule with its environment. The interaction of a molecule with its environment leads to a slight change of the energy of a molecular vibration. Furthermore, the interactions of a molecule with its environment leads to a different line shape of the peak. The environment of an atom or molecule in a solid is fixed, and therefore the energy of a vibrational mode is a statistical distribution of interactions with its neighbors, leading to a Gaussian line shape. For a molecule in gas phase, the molecule will collide with many other surrounding molecules leading to exponential vibrational population relaxation. This process leads to a Lorentzian line shape. For a liquid the line shape theoretically can be best described by Voigt profile, which has features of both Gaussian and Lorentzian line shapes. However, in many cases a Lorentzian line shape also works well for fitting Raman peaks of liquids.

2.2. Surface-enhanced Raman spectroscopy

2.2.1. Introduction

Our aim is to probe ensembles of molecules or even single molecules at solid-liquid interfaces. In the scope of this thesis, the liquid phase is water. As explained in section 2.1.1, Raman spectroscopy fulfills two requirements for probing ensembles of molecules at solid-water interfaces: Raman spectroscopy has chemical specificity by resolving the vibrational 'fingerprint' of molecules under study, and the incidence laser light can reach the molecules of interest at the solid-water interface because it is freely propagates through aqueous electrolytes. However, there is one drawback that hinders Raman spectroscopy of ensembles of molecules at solid-liquid interfaces. The Raman cross-section is too small to detect few molecules at an interface by conventional Raman spectroscopy [32]. To enable the detection of a few molecules at a substrate the Raman signal must be amplified. A method to amplify the intensity of Raman scattering by several orders of magnitude is surface-enhanced Raman spectroscopy (SERS).

2.2.2. Enhancement of Raman scattering in SERS

Enhancement of Raman scattering of pyridine molecules at a silver substrate was first noticed by Fleischmann et al. in 1974 [37]. A few years later Jeanmaire and Van Duyne demonstrated that the Raman enhancement of pyridine at a silver substrate was due to roughening of the underlying silver substrate [38]. Shortly after the latter study Moskovits suggested that the Raman enhancement observed in the earlier papers originated from the excitation of surface plasmons in bumps on the roughened silver substrate [39]. These studies were the first to report SERS, which makes Raman spectroscopy of submonolayers of molecules adsorbed to or close to roughened coinage metal surfaces (typically within less than $\sim$10 nm) possible [32].

EM enhancement mechanism
The SERS mechanism is based on the excitation of localized surface plasmons (LSPs) at metallic nanostructures. Plasmons are collective oscillations of electrons. For two EM modes (in this case light and surface plasmons, SPs) to couple, they need to have the same frequency ω (for conservation of energy) and the same wave-vector k (for conservation of momentum). The dispersion relation of light is linear while the dispersion relation of SPs shows a curve where k goes to infinity when the ω reaches the resonance frequency $\omega_s p$ [32, 40]. For the case of propagating light and SPs along an atomically flat surface, the dispersion relations of light and SPs never cross when placed in the same graph, i.e. the momentum of these two EM modes is never the same for a given frequency, therefore these EM modes can not couple. A method to overcome this momentum mismatch is using evanescent light, e.g. produced by attenuated total reflection of light in a Kretschmann or Otto configuration [32]. Evanescent light near the surface of a metal is slower than propagating light, leading to a match of momentum with SPs along an atomically flat surface at a certain frequency. Incident evanescent light of that frequency can couple to SPs, which results in resonant excitation of SPs in the metal. The excited SPs propagate along the surface of the metal, and are therefore called propagating surface plasmons (PSPs). PSPs can be used for imaging nanostructures with a spatial resolution beyond the diffraction limited spatial resolution (Abbe diffraction limit: minimum resolvable distance of $\sim \lambda/2$ of incident light) of light microscopy.

On the contrary to atomically flat metallic surfaces, propagating light can couple to SPs in metallic nanostructures, of sizes much smaller than the wavelength of the propagating light [41]. In the case of a metallic nanostructure, EM modes exist for discrete values of ω. Therefore, dispersion relations, described for the wavevector k(ω), become irrelevant. The excited SPs at the surface of the metallic nanoparticle are localized, therefore these EM modes are called localized SPs (LSPs).

The light-metal nanostructure interaction can be understood as the electric field of the incident light causing separation of free-charge carriers in the metal (see left of figure 2.3) [40]. This separation of charges (dipole) induces a field oscillating with the same frequency as the field of the incident light. This near-field is extremely localized and enhanced, compared to the EM field of the incident far-field light.

Furthermore, the close distance of a molecule to a large polarizable body (nanostructure) leads to the second step in EM enhancement in SERS. The induced dipole of a molecule couples to the induced dipole in the nanostructure. This leads to polarizability derivatives of the nanoparticle-molecule system of typically one to three orders of magnitude larger than the polarizability derivatives of the molecule [42]. The nanostructure serves as an optical transmitting antenna, transferring the near-field to the far-field [42].

EM enhancement is the primary enhancement effect in SERS [32, 42]. Other enhancement

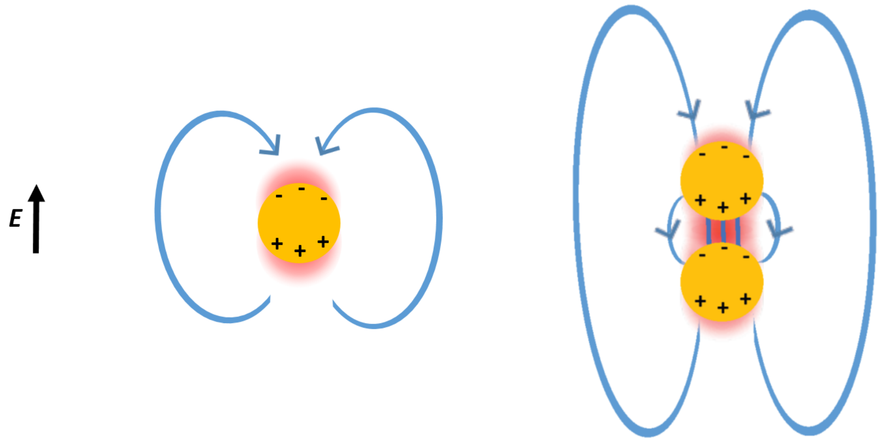

Figure 2.3.: Schematic image of electric field distribution near a metallic nanoparticle (left) and near a dimer of two metallic nanoparticles (right) and resulting field enhancement at the poles of the metallic nanoparticle (left) and in the gap between the nanoparticles (right). Direction of external electric field is indicated by E.

effects, such as the chemical enhancement which is due to binding of the molecule to the metal, become important to explain specific cases of single molecule SERS/TERS. This thesis does not contain results on single molecule SERS/TERS, therefore we will not discuss other enhancement effects here.

Variables influencing SERS enhancement

The enhancement of SERS depends on the efficient coupling of the far-field light to the LSPs in the nanostructure. This can be realized when the wavelength of the incident light matches the plasmon resonance wavelength [43]. The plasmon resonance frequency depends on the dielectric constant of the nanostructure material, the dielectric constant of the surrounding medium and the size and shape of the nanostructure [32]. The material of choice for a SERS substrate is usually Au or Ag, because the LSP resonance frequency of Au or Ag nanostructures is in the visible region, close to the wavelength of incident laser light in Raman spectroscopy [32].

The enhancement of SERS also depends on the shape of the plasmonic nanostructure and polarization of the incident light. Some of the largest known SERS enhancements were observed to come from the near-field in the few nanometer-sized gap between two metallic nanostructures. The large field enhancement in the gap between two metallic nanoparticles is due to dipole-dipole coupling, which can be visualized by drawing the electric field distribution around a dimer of two nanoparticles (see the right of figure 2.3). The induced dipoles in the nanoparticles in the right of figure 2.3 are parallel, as a response on the linear polarization of the incident light. Dipole-dipole coupling of two dipoles strongly depends on the distance r between the dipoles. The interaction energy between two dipoles is proportional to r^{-3} [33], given that the dipoles are parallel.

The right of figure 2.3 also shows another important aspect of the near-field in a nanoparticle gap. The field lines in the gap are straight, from one nanoparticle to the other nanoparticle. This means that the EM field in the gap is polarized, and as such, only molecular vibration which polarizability derivatives are along the gap-direction will be enhanced. This is a SERS selection rule.

SERS enhancement factors
Typically, enhancement factors (EFs) are considered for Raman intensities measured by SERS or TERS. The enhancement of the field of the incident light E_L in the near-field E_{Loc}, is described by the field enhancement g, $g = E_{Loc}/E_L$. In the same way as the intensity I of EM radiation is proportional to the square of the EM field strength, $I \propto E^2$, Raman enhancement is calculated as the square of g. In SERS, g consists of the enhancement of the incident light $g_i n(\omega_L)$ and radiation enhancement of the Raman scattered light $g_s c(\omega_S)$, where ω_L and ω_S are the frequencies of the incident light and Raman scattered light, respectively. The overall field enhancement g can be written as:

$$EF = g_i n(\omega_L)^2 g_s c(\omega_S)^2 = \frac{E_{Loc}(\omega_L)^2}{E_L(\omega_L)^2} \frac{E_{Loc}(\omega_S)^2}{E_L(\omega_S)^2} \tag{2.12}$$

Generally in Raman spectroscopy, the vibrational energy is much smaller than the energy of the incident light. Therefore, the incident light only looses a small amount of energy to the molecular vibration (in Stokes Raman scattering) and the wavelength of Raman scattered light can be considered very close to the wavelength of the incident light. Assuming $\omega_L \approx \omega_S$, equation 2.12 can be further simplified to:

$$g^4 \approx \frac{E_{Loc}(\omega_L)^4}{E_L(\omega_L)^4} \tag{2.13}$$

Equation 2.13 is the famous g^4 approximation for EM enhancement in SERS.

SERS hot-spots
The enhancement of Raman scattering of a monolayer of molecules on a rough coinage metal substrate is not evenly distributed over the substrate. Experimental studies showed that enhanced Raman intensity originates from a small number of SERS 'hot-spots' on the substrates [44]. Futhermore, SERS enhancement varies largely from spot-to-spot. A striking example of this was shown by Fang et al. in 2008, by measuring SERS of a benzenethiolate monolayer on silver [45]: 24 percent of the total SERS intensity originated from only ~63 out of one million benzenethiolate molecules on the substrate.

2.3. Tip-enhanced Raman spectroscopy at the solid-gas interface

2.3.1. Development of TERS

SERS shows large Raman scattering enhancements, but using SERS for chemical imaging with a nanometric spatial resolution is difficult, because of the practical difficulty to get the molecule(s) under study into the near-field in proximity of a metallic nanostructure. Furthermore, SERS is restricted to metallic surfaces. Nanometric chemical imaging of surfaces is enabled by fixing a metallic nanostructure to a tip or cantilever and scanning this probe over a surface, similar to other scanning probe microscopies (SPM). This idea was first described by Wessel in 1985 [46] and in the year 2000 tip-enhanced Raman spectroscopy (TERS) was practically proven by four independent research groups [47, 48, 49, 50]. In TERS a tip, usually made of Au or Ag, with an apex radius of about 20 nm is used as a single hot-spot for Raman enhancement [42] (see image 2.4), contrary to the many hot-spots inside the laser focus on common SERS substrates. Due to mechanical control over the positioning of the tip, the hot-spot for Raman enhancement can be positioned nearby (an ensemble of) molecules of interest, thereby circumventing the difficulty of bringing the molecule(s) of interest into the hot-spot on SERS substrates. Bringing the hot-spot to molecules adsorbed at a substrate, by approaching the tip to a distance of $\sim$1 nm away from the substrate (see image 2.4), largely enhances the Raman scattering intensity of these molecules. The enhancement factor of TERS compared to conventional Raman spectroscopy is around 10^3 to 10^6 [51]. The lateral spatial resolution of TERS in the ambient is typically similar to the radius of the tip apex [42], although spatial resolutions of 1.7 nm [52] and 0.5 nm [53] have been reported.

2.3.2. Enhancement of Raman scattering in TERS

The same plasmon-enhancement principles of SERS apply for TERS, where the apex of the tip is the plasmonic nanostructure (see section 2.2.2 for the explanation of plasmon-enhancement in SERS). Focusing light to the apex of the TERS tip leads to the excitement of localized surface plasmons (LSPs) at the surface of the tip, which induce an enhanced local EM field (near-field) around the apex of the tip (see figure 2.4). Like in the case of SERS, the local field enhancement depends on the wavelength and polarization of the incident light, dielectric constant of the tip material, dielectric constant of the surrounding medium and shape of the tip (see section 2.2.2).

In TERS, the gap-mode configuration for EM field enhancement, as explained for SERS in the right of figure 2.3, can be applied. To model the gap-mode configuration for TERS, the tip is replaced by a metal nanosphere above a metal substrate [54] (see figure 2.4). The induced dipole in the metal nanosphere creates an image dipole in the metal substrate. The EM field of the induced dipole in the nanosphere and the EM field of the image dipole superimpose, leading to an enhanced near-field and improved spatial resolution in the gap. As explained for the gap-mode configuration in SERS, the strength of the local enhanced EM field in the gap increases with a decreasing gap distance [1, 55].

Ideally, the enhanced near-field is confined underneath the apex of the TERS tip, as this is the position of the tip that is brought close to molecule(s) of interest. For TERS in side-illumination geometry p-polarized incident laser light forms an intense near-field beneath the apex of the tip, while s-polarized incident laser light does not enhance the field beneath the tip (see image 6.32 in [56]). The reasons for this are that the direction of the induced dipole in the tip apex should be along the tip axis to have the most dense electric field lines of the induced dipole coming out at the apex of the tip (in the same way as shown schematically for gap-mode SERS in the right of figure 2.3). Furthermore, the lightning rod effect plays a role in the efficiency to couple light to the tip. The conical shape of the metallic tip can be modeled as a cascade of spheres of decreasing sizes [57]. Upon coupling

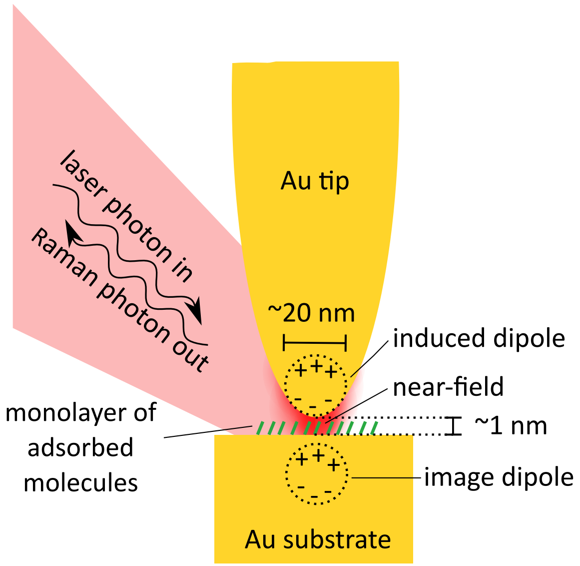

Figure 2.4.: Schematic representation of formation of enhanced EM near-field in gap-mode tip-enhanced Raman spectroscopy (TERS) in backscattering geometry with a Au tip and Au substrate.

with incident light, these spheres will have induced dipoles pointing in the same direction as the polarization of the light. In case of p-polarized light, the dipoles of the different spheres couple, leading to amplification of the near-field in the gaps between the smallest particles. This process is so-called cascade enhancement [57]. The gap between the smallest particles is in case of gap-mode TERS the gap between tip and sample (between induced dipole in the apex of the tip and image dipole in the substrate). Cascade enhancement can enhance the near-field by a factor of several hundred compared with the field of the incident light. Another effect on the EM near-field is the amount of metal in the laser focus. The conical shape of the TERS tip makes the diameter of the tip decrease from several hundred µm to ~ 40 nm. The diameter of the laser focus is several hundred µm. Therefore, the hundreds of µm of metallic tip in the laser focus will add up to the lightning rod effect.

2.3.3. TERS spectral interpretation

Several 'issues' make the interpretation of TER and SER spectra more complicated than that of conventional Raman spectra. TER and SER spectra come with a broad continuum background, of which its maximum energy can change from TERS tip to TERS tip and from SERS substrate to SERS substrate. Furthermore, the peak intensity ratios in single TER or SER spectra can differ as well when changing to another TERS tip or to another SERS substrate. Very recently, Lin et al. [58] showed that the shape of the broad background and the peak intensity ratio are both connected to the LSP resonance. At the LSP resonance frequency the SERS background (which is partly due to photoluminescence [59]) is high and the SERS peaks are high, compared to non-resonant regions in the SERS spectrum where the background and SERS peaks are low. Lin et al. proposed a scaling method where the SERS or TERS background serves as an internal standard for the plasmon resonance dispersion. By applying their scaling method, they could retrieve the same SERS and TERS spectra while varying SERS substrates and TERS tips.

2.3.4. Scanning probe microscopy and TERS tips

In TERS, the spatial positioning of the tip with respect to the substrate is typically controlled by either an atomic force microscopy (AFM) or scanning tunneling microscopy (STM) [60].
Commercial AFM and STM systems are designed for raster scanning of substrates, which can be used for TERS mapping.
For AFM-TERS, the most common method to fabricate TERS-active tips is covering commercial AFM cantilevers with a Au or Ag film. The latter is performed by thermal evaporation of Au or Ag in vacuum [61].
In STM-TERS, the tip is usually made out of a Au or Ag wire which is electrochemically etched into a cone shape [61].

In general, STM has a higher resolution than AFM. STM can only be applied on conductive substrates, while AFM can be used on insulating substrates as well.

2.4. TERS at the solid-liquid interface and electrochemical TERS

2.4.1. Development of solid-liquid (electrochemical) TERS

In 2009, almost ten years after the first TERS reports, a proof-of-principle study of TERS at the solid-liquid interface was published by the Zenobi group [30]. Since then, mainly three groups, Van Duyne [62], Ren [63] and Domke [64] have been working on developing solid-liquid (electrochemical) TERS. Moving from solid-gas (or solid-vacuum) TERS to solid-liquid TERS is technically challenging, for several reasons which are explained in the following sections.

2.4.2. Illumination geometry for solid-liquid TERS

There are various illumination geometries to focus laser light to the apex of a TERS tip at the solid-liquid interface (see the illumination geometries for solid-liquid TERS used to date in figure 2.5). All these geometries are used in backscattering geometry, where the same objective is used to focus the incident light to the tip and collect scattered light. The choice of illumination geometry of a TERS setup depends on the opacity of the substrates to be investigated and the efficiency to couple light to the tip.

In bottom-illumination (left in image 2.5) laser light is focused on the tip in transmission mode. In this illumination geometry, oil-immersion objectives can be used [30], which have a higher numerical aperture than in air and liquid-immersion objectives, which increases both the efficiency of coupling light to the tip and detection efficiency. Using radially polarized light leads to a better coupling efficiency of light to the tip in this

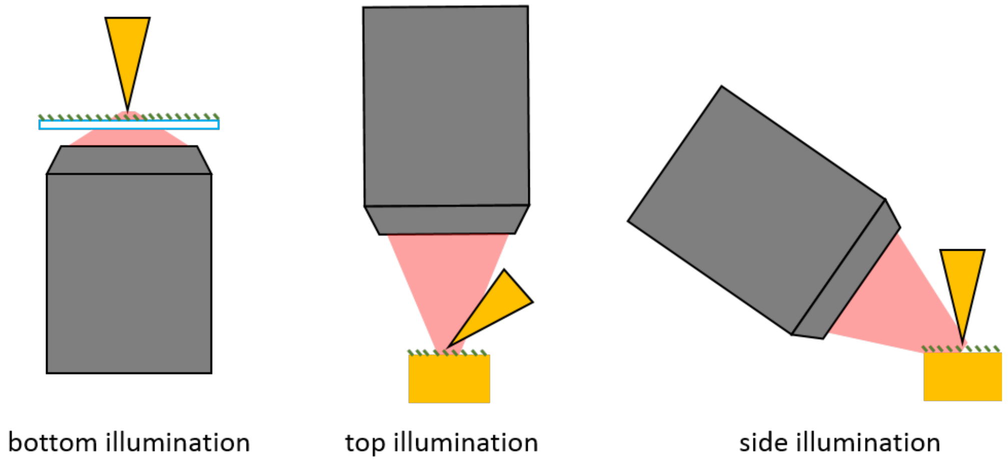

Figure 2.5.: Illumination geometries for tip-enhanced Raman spectroscopy at the solid-liquid interface.

geometry [65]. Bottom-illumination TERS can only be used for transparent substrates. Glass substrates, optionally with a 6 - 10 nanometers thick Au layer to enable gap-mode TERS, have been used for solid-liquid AFM-TERS [30, 66] and ITO substrates have been used for electrochemical AFM-TERS [62] with this illumination geometry. The limited choice of transparent substrates limits the applicability of bottom-illuminated TERS.

Side- and top-illuminated TERS can be used for both transparent and opaque substrates. This makes side- and top-illuminated TERS versatile for the choice of substrate material and substrate thickness. Thick and opaque substrates are especially important in electrochemical TERS, where ideally a several millimeter thick metal (single crystal) substrate is used to secure a homogeneous surface potential, as opposed to few nanometer thick metal layers.

As explained in section 2.3.2 the polarization of light influences the coupling of light to the tip. For side-illumination p-polarized light has to be used to create a near-field between tip and sample. In top-illumination the tip should be inclined to avoid shadowing effects. A drawback of side- and top-illumination is the use of long-working distance, in-air objectives with smaller NA (typically less than 0.55). Touzalin et al. [67] used a water-immersion objective in top-illumination, to increase coupling efficiency of light to the tip and detection efficiency of scattered photons. However, as TERS is a molecule-sensitive technique, all parts touching the liquid phase have to be thoroughly cleaned to remove (mainly carbonaceous) contamination. Thorough cleaning procedures using strong acids (for a detailed cleaning procedure, see section 3.5) can not be performed with an objective, and therefore the objective is a possible source of contamination if immersed inside the liquid phase in solid-liquid TERS. Furthermore, the small working distance of water-immersion objectives makes the TERS setup design difficult.

If an in-air objective is used for side-illuminated solid-liquid TERS, the laser light has to pass several interfaces of media with different refractive indices before reaching the apex of the TERS tip, compared to solid-air TERS. The introduction of these interfaces (air-water or air-glass and glass-water) distort the laser focus in two ways: the focal length increases and the focus gets less sharp. A way to minimize focus distortions is to decrease the path length of the laser beam inside the liquid phase. The latter has been shown in an electrochemical STM-TERS study [63] where the apex of the tip was placed ∼1 mm away from a glass window. Another way is to actively precompensate for focus distortions by adaptive beam shaping, for example with the help of a spatial light modulator (SLM) [68, 69]. A SLM is an electronic mirror consisting of liquid-crystalline pixels that can be tuned independently to actively shape the phase and amplitude of (parts of) a light beam.

2.4.3. SPM base and tips for solid liquid TERS

The choice of SPM for solid-liquid TERS follows different requirements than the coice of SPM for in-air TERS. Some of these considerations are discussed here.
In STM the tip holder does not touch the liquid phase, which makes the chance on contamination smaller than when using AFM, where the tip holder touches the liquid phase. An STM tip does not touch the sample, as in the case of contact-mode AFM, therefore the chance to pick up molecules with an STM tip is smaller than with AFM. In general, knowledge about solid-liquid (electrochemical) AFM is less abundant than knowledge about solid-liquid (electrochemical) STM.

Both AFM- and STM-TERS tips need an extra treatment before they can be successfully used in solid-liquid TERS experiments. For the use of AFM-TERS tips in a liquid environment, extra protective layers underneath and/or on top of the Au or Ag film have to be added to protect against delamination of the Au or Ag film [66]. For the use in water various coatings have been successful, such as Cr - Au - Ag [66].
For use of STM-TERS tips in a liquid environment, the liquid phase might introduce Faradaic leakage currents. The latter leads to electrons passing the liquid directly instead of tunneling between the tip and the sample, preventing a stable gap distance between tip and sample. A way to avoid Faradaic leakage currents is insulation of STM tips, except for their apex. Tip insulating procedures that have been successful in TERS in aqueous solutions are coating with Zapon lack [64], coating with polyethylene glue [63] or deposition of a silica shell [70]. Fluorescence of tip-insulating materials at the wavelength of the incident laser beam should be avoided, as it might overwhelm the much smaller TERS signal.

3. Home-designed solid-liquid TERS setup: instrumentation and data acquisition

This chapter contains technical details of our home-designed solid-liquid TERS setup. The beam path design of the TERS setup and sample cells designs for solid-liquid TERS are described in detail. Furthermore, procedures essential for a successful TERS experiment are shared: fabrication of TERS-active tips, cleaning procedures, procedures to check for tip-cleanliness during TERS experiments and TERS data processing.

3.1. Beam path

The beam path of the solid-liquid TERS setup is schematically drawn in figure 3.1. The TER spectrometer is mounted on an optical table with active vibration isolated legs (CleanTop, TMC).

Beam path for TER spectral acquisition
The incident beam path starts with a HeNe laser (LSRP-3501, REO, 632.8 nm, 35 mW maximum output power, linearly polarized) and a laser clean-up filter (MAXLINE LL-632.8-25.0M, Semrock). Two optical density (OD) filters are used to control the power of the laser light reaching the sample: an OD 1 filter is placed on a flippable post directly after the laser. After the first mirror (all mirrors are type BB1E02 by Thorlabs GmbH) the beam encounters a wheel with OD filters (FW212C, Thorlabs; filters with OD between 0.1 and 1.3). After the filter wheel, the laser beam encounters a dichroic beamsplitter (LPD01-633RU-25, Semrock; incidence angle 45°; edge filter with cut-off at 156 cm^{-1}), that reflects 633 nm light. The beam enters an objective (LMPLFLN, Olympus, air objective, magnification 50x, numerical aperture 0.5, working distance 10.6 mm). An optical beam expander (BE052-A, Thorlabs) is used to overfill the entrance of the objective.
The detection path starts with the collection of scattered (and reflected) light by the same objective as the incident beam path (backscattering geometry). The scattered light follows the same beam path as the incident light, in the opposite direction. The Raman scattered light is transmitted by the dichroic beamsplitter while (most of) the Rayleigh scattered and reflected light of 633 nm is reflected by the dichroic beamsplitter. A long-pass edge filter (LP02-633RE-25, Semrock; incident angle 0°; transition width at 79 cm^{-1}) is added to filter out any residual Rayleigh scattered light while Raman scattered light is transmitted. A lens is placed in front of the spectrograph (iHR 550, Horiba; focal length 550 mm, gratings of 600, 1200 and 1800 g/mm, resolution) to focus the beam on the entrance slit of the spectrograph, thereby filling the diffraction grating. After diffraction of the light by the grating the light is detected as counts on the detection chip of the CCD camera (Symphony II, Horiba; 1024×256 pixels, liquid nitrogen-cooled).

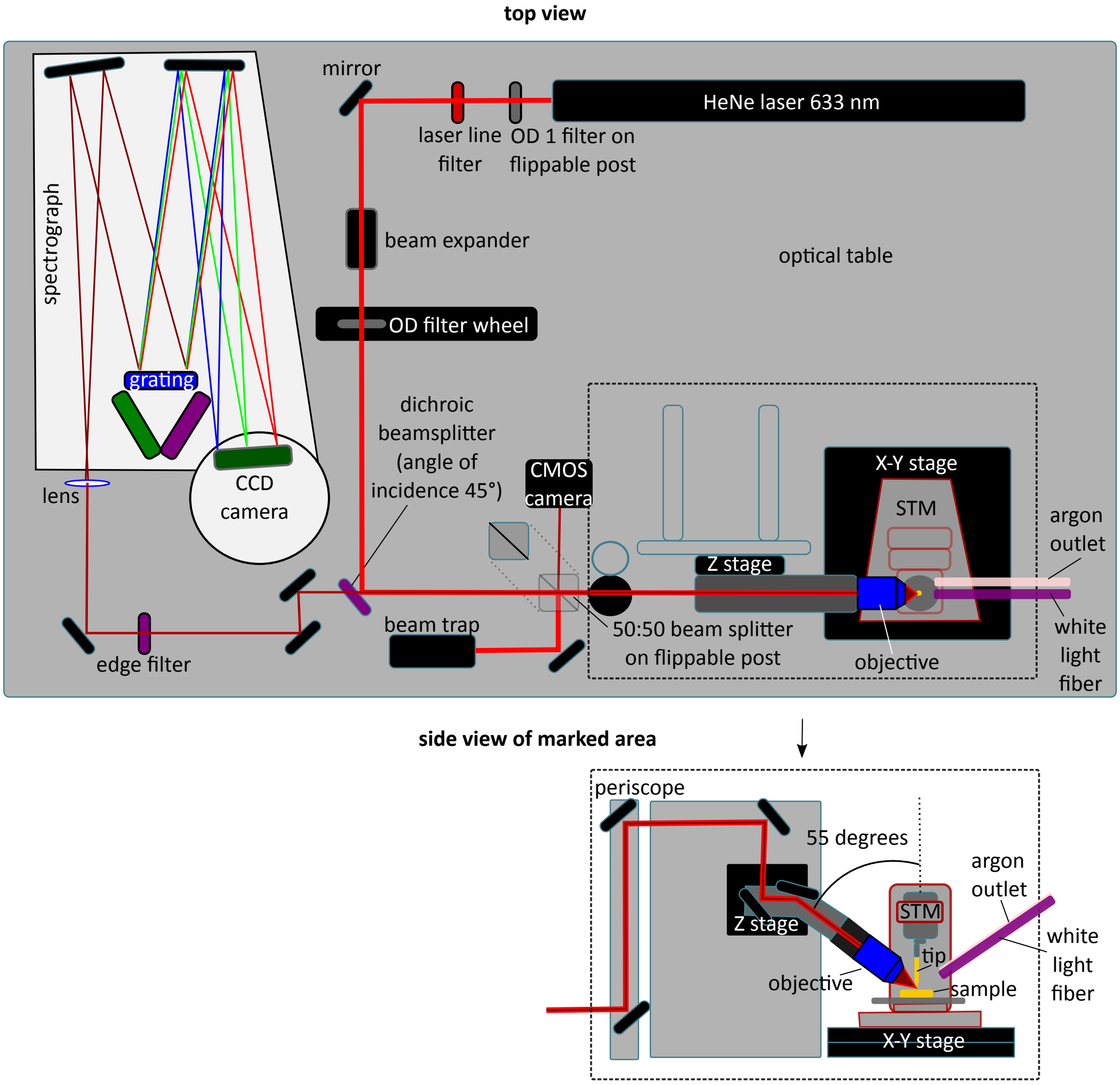

Figure 3.1.: Schematic drawing of the TERS beam path.

Beam path for focusing and focusing procedure

To enable a TERS measurement, the apex of the TERS tip (typically of a diameter of a few tens of nanometers) must be placed inside the focus of the beam after the objective. Several elements in the TERS setup enable quick focusing of the beam to the TERS tip. The mechanical movement of the tip-sample junction (STM) and of the beam focus are enabled by two piezo-stages (custom-made by Steinmeyer Mechatronik GmbH, former Feinmess Dresden GmbH), respectively. The objective is mounted on a single-axis piezo stage that controls the vertical positioning of the objective with a ∼3 nm stepsize without losing the alignment of the incident beam. The STM (to which the TERS tip and sample are mounted) is moved laterally by a x,y-piezo stage with a ∼3 nm stepsize. The vertical nanometric positioning of the objective and the horizontal nanometric positing of tip-sample junction enable focusing of the incident beam to the apex of the tip with excellent precision.

A white light path is implemented in the TERS setup for focusing purposes. The use of white light for focusing instead of the laser light decreases the chances of heat damage to the sample due to elongated focused laser radiation. A white light fiber (KL 1600 LED, Schott) is pointing towards the sample, mirroring the angle of the incident laser light to the sample. In this geometry of the white light fiber, the white light is reflected by the sample and enters the objective. During the focusing procedure, an additional beamsplitter (CM1BS013, Thorlabs; polarization insensitive, 50:50) is added in front of a CMOS camera (EoSens MC 1362, Mikrotron). This beamsplitter enables the (simultaneous) detection of reflected white light and of reflected laser light by the CMOS camera, which is used as a feedback during focusing.

The coarse focusing procedure starts by bringing the apex of the TERS tip into the focus of the objective by using the white light path. Whenever the TERS tip is in the white light path, a shadow is seen on the CMOS camera. Then the piezostages are moved until a clear image of the apex of the tip (and, depending on the reflectivity of the sample also a clear mirror image of the tip in the sample) are visible with the CMOS camera. For the fine focusing of the laser light to the tip, the white light is turned off and the laser is turned on (placing the OD filters such that the power of the laser beam in the focus of the objective is ∼150 µm to avoid heat damage of the sample). In this configuration, 50% of the incident laser light is transmitted by the 50:50 beamsplitter towards the tip and sample (the other 50% is absorbed by a beam trap; BT600/M, Thorlabs). In the detection path, 50% of the laser light reflected by the tip and sample reaches the CMOS camera. The image of the reflected laser light in the CMOS camera is used as a feedback for fine focusing of the laser light to the TERS tip.

Alignment procedure

TER scattering is a weak process, therefore alignment of the beam path in the TERS setup is important to ensure collection of as many scattered Raman photons as possible. The TERS beam path is aligned by turning the mirrors. After every mirror an iris diaphragms (ID8/M, Thorlabs; not shown in figure 3.1) is placed to indicate the desired beam path. The alignment of the beam through the pinholes is checked either by eye or by a power meter (S130VC, Thorlabs Gmbh; Slim Silicon Power Head, 200-1100 nm, 5mW/50mW; connected to a multimeter). In the incident beam path, the objective is

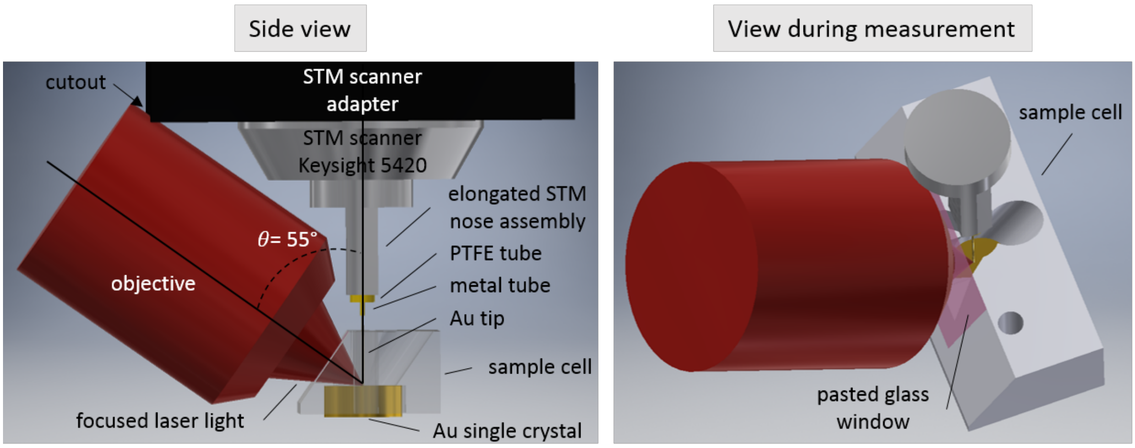

Figure 3.2.: Schematic representation of solid-liquid TERS measurement geometry. (left) Side view of solid/liquid TERS measurement geometry. In this representation the sample cell is made transparent to show the focus of the laser light to the tip-sample junction. (right) View point to the tip-sample junction during a solid/liquid TERS experiment.

the most sensitive optical element to alignment. The beam should enter the objective straight and (over)fill the objective to create a focus with high power density essential for TERS. Also in the the detection path the angle of incidence of the beam on several optical elements influences their efficiency. The dichroic beamsplitter and edge filter transmit scattered light and reflect Rayleigh scattered light most efficiently at an angle of incidence of 45° and 0°, respectively. Furthermore, the scattered beam must enter the lens in front of the spectrograph at 0° to ensure an efficient filling of the grating in the spectrograph leading to efficient detection of scattered photons by the CCD camera. However, Raman scattered light is so weak that it is not visible by eye or measurable with a common power meter. In backscatting geometry, the incident beam path and detection beam path overlap. Therefore, the alignment of the incident beam path also sets the alignment of the detection path from the objective until the dichroic beamsplitter. The detection path between the dichroic beamsplitter and the spectrograph is aligned by placing a Si wafer in the focus of the objective and using the Raman signal of a Si detected by the CCD camera as feedback.

3.2. Illumination geometry of solid-liquid TERS setup

The left window of figure 3.2 shows a schematic representation of the side-illumination TERS measurement geometry. This geometry is a back-scattering geometry where the angle of incidence = angle of detection = θ. The placement of the objective at θ = 55° with respect to the sample surface normal, is based on the following considerations. Both the coupling of light to the TERS tip and TERS detection depend on θ.
For efficient detection of TERS, the directionality of the radiation from the tip-sample junction has to be considered. The radiation intensity of the junction between a Au

nanoparticle and a metal substrate is largest at $\theta \approx 55\,^\circ$ [71].
To form an enhanced near-field in the tip-sample junction in side-illuminated TERS, the incident laser light needs to be p-polarized (explained in section 2.3.2 of chapter 2). At $\theta = 90^\circ$ the incident light has the largest p-polarized component compared to $\theta < 90^\circ$. However, in the geometry of figure 3.2, $\theta = 90^\circ$ could lead to a large part of the incident light being cut off by sample (and sample cell) instead of illuminating the apex of the tip, thereby decreasing the coupling efficiency of incident laser light to the tip. Therefore, a compromise has to be found where incident light can be efficiently coupled to the apex of the tip and the incident laser light has a large p-polarized component.
By placing the objective in the S/L TER spectrometer at $\theta = 55^\circ$, the coupling of incident light to the tip and the TERS detection efficiency are optimized.

To fit the objective underneath the STM scanner and STM scanner adapter in the S/L TERS spectrometer, two changes have been made to the commercial Keysight 5420 STM. The STM scanner adapter has a round cutout at the side to make space for the objective (at the place of the arrow in the left window of figure 3.2). Furthermore, the STM nose assembly is elongated by 7.6 mm compared the a standard Keysight STM 5420 scanner, to shorten the distance from STM nose to sample surface in the side-illuminated TERS geometry of figure 3.2. With a shorter STM nose to sample distance, shorter tips can be used which increases tip stability during STM-TERS experiments. Note that TERS tips in the TERS configuration of figure 3.2 still have to be $>$ 9 mm, which is much longer than the conventional STM tips of ∼2-3 mm. The reason for this relatively long STM nose to sample distance is preventing the STM nose assembly from touching the liquid layer in the S/L TERS sample cell.

3.3. Sample cell design for solid-liquid TERS

The S/L TERS sample cells are designed to contain an up to 6.6 millimeters thick water or aqueous electrolyte layer and to block only a minimal part of the incident light at $\theta = 55^\circ$. The window of the sample cell is placed in the normal of the beam direction to minimize asymmetry of the focus due to optical aberrations of the air-glass and glass-water interfaces. The assembly of sample cell, tip and objective as seen during a TERS experiment is shown in the right of figure 3.2.
Sample cells have been designed for two different substrates: for metal single crystal disks of 10 mm diameter and 4 mm height and for planar samples with various dimensions, respectively. The technical drawing of a S/L TERS sample cell for a single crystal disk is shown in figure 3.3. The sample cell is placed on top of a single crystal, with an 8×0.5 mm O-ring (FFKM75, perfluoroelastomer; acid- and heat resistant material; DTH Dichtungstechnik GmbH) in between to avoid water leakage (see figure 3.4). A glass window (coverslip 22×22 mm^2, 170 µm thick, Carl Roth, see figure 3.4) is pasted at the sample cell with UV glue (Loctite 3321). The sample cell contains two holes for clamping it on to the conventional STM 5420 and 5500 sample plates. To avoid damage to the metal single crystal, the single crystal has to be positioned on the sample plate first, then the O-ring is placed on top, and then the sample plate is placed on top and softly clamped to the sample plate. The sample cell leaves ∼0.2 mm of the bottom of the metal single crystal free (see right window of figure 3.4) to enable contacting an electrode and thus

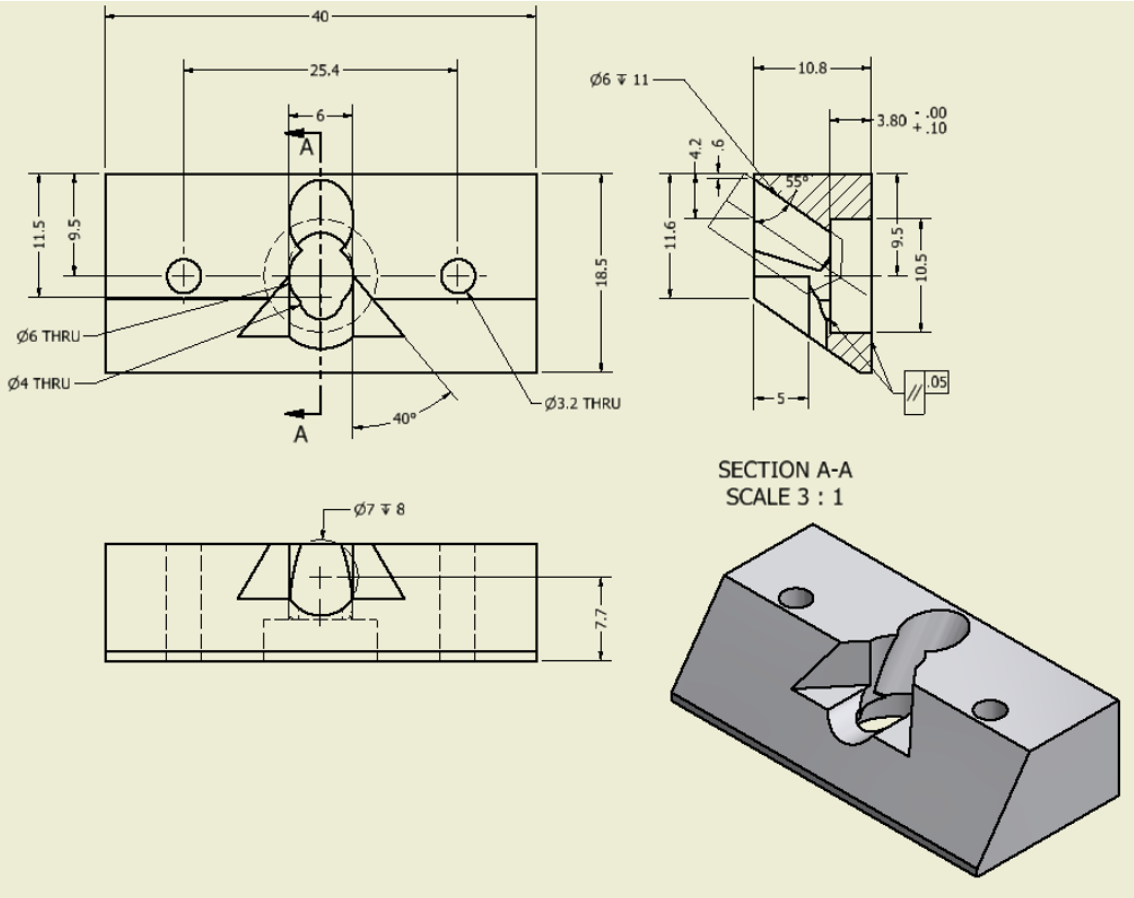

Figure 3.3.: Sample cell design for S/L TERS on single crystal disk electrodes of 10 mm diameter and 4 mm height. The sample cell is made out of PCTFE.

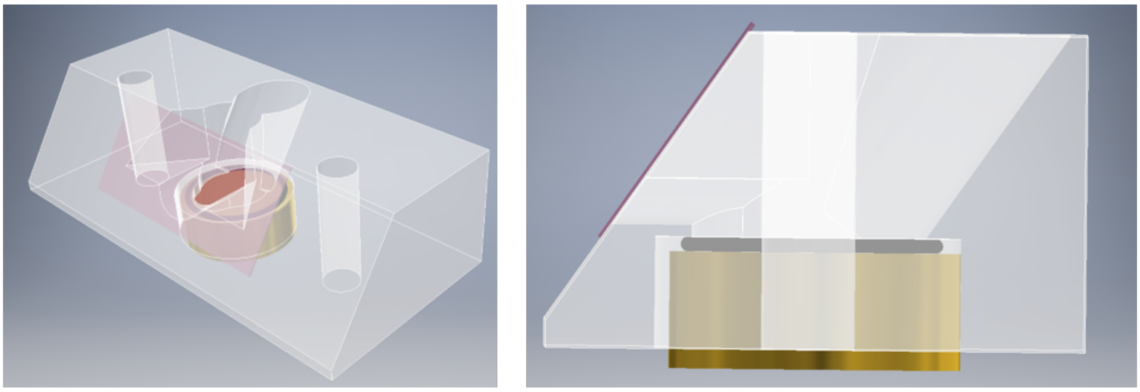

Figure 3.4.: (left) Assembly of S/L TERS sample cell (see figure 3.3 for technical drawing), placed on a single crystal, with a sealing O-ring in between. A glass window (pink) is glued on the sample cell. (right) Side view of assembly of S/L TERS sample cell and single crystal sample. The O-ring seals the water/electrolyte reservoir.

closing the STM electronic circuit.

The S/L TERS sample cell design for a single crystal disk sample has been adapted to be used for planar samples, such as cover slips or Au/mica electrodes. A sample cell design for S/L TERS on a planar sample is shown in figure 3.5. There are three adaptations of the metal single crystal sample cell to fit planar samples. First, a chamber was drilled to fit a planar sample with a minimum length×width of 10×10 mm and a maximum length×width of 16×17 mm. To stably clamp a planar sample onto the sample plate with this cell, the height of the sample should be $<$ 4 mm. To clamp samples with a height of $<$ 3.4 mm, an extra part has to be used as a spacer ('part 2' in figure 3.5). This sample cell was used to clamp Au/mica substrates of ~0.3 mm. An assembly of sample cell and Au/mica sample is shown in figure 3.6. If samples thicker than 0.5 mm should be clamped with the cell, the height of the spacer ('part 2' in figure 3.5) should be reduced accordingly for stability. Second, one of the holes to clamp the sample cell on the sample plate was replaced by a U-shape open to the side of the sample cell to enable sliding of the sample cell assembly onto the clamping position on the sample plate. This facilitates clamping the sample cell assembly to the sample plate. Third, two small holes are drilled through the top of the sample cell to enable connecting a (spring-loaded) electrode to the sample surface from the top without touching the liquid phase.

TERS sample cells were fabricated by the in-house fine-mechanical workshop according to my designs. The sample cells were milled out of PCTFE (polychlortrifluorethylen, Kel-F), bought from Duelplast GmbH, Germany. PCTFE was chosen for two reasons: PCTFE is resistant against oxidation by the strong acids we use in the cleaning procedures and PCTFE is hard enough to mill small (<1 mm) details, compared to the more commonly used PTFE (polytetrafluoroethylen, Teflon) which is too soft for milling small details.

Part 1

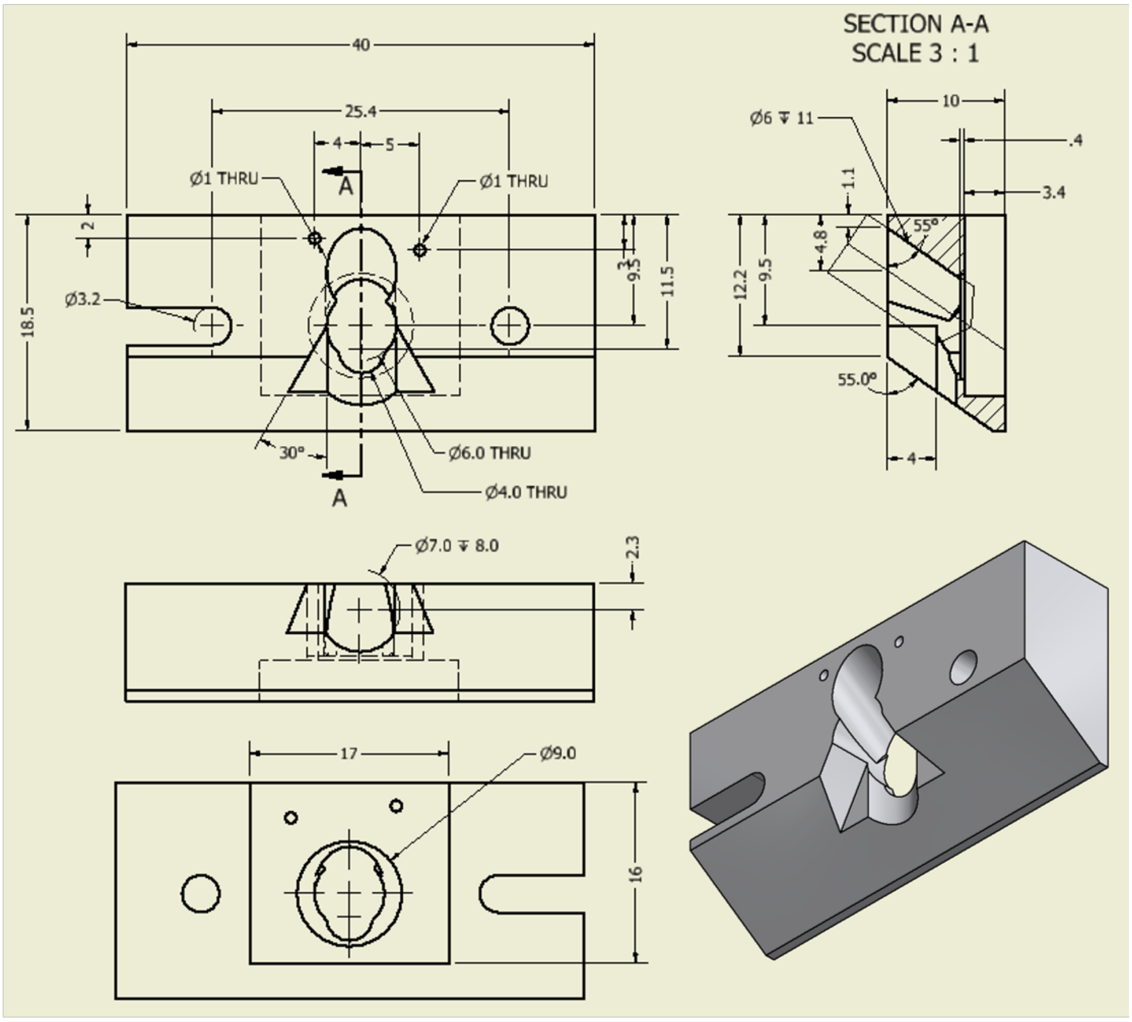

Part 2

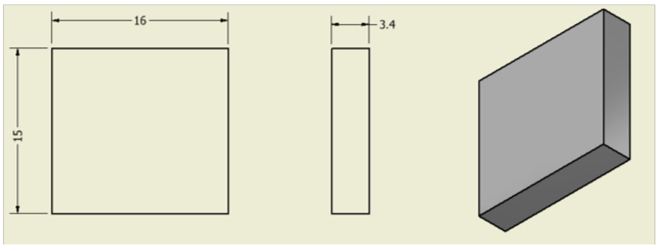

Figure 3.5.: TERS in liquid sample cell design for flat samples with minimal length×width of 10×10 mm, and maximal length×width of 16×17. Sample cell consists of a PCTFE part (part 1) and aluminium spacer (part 2).

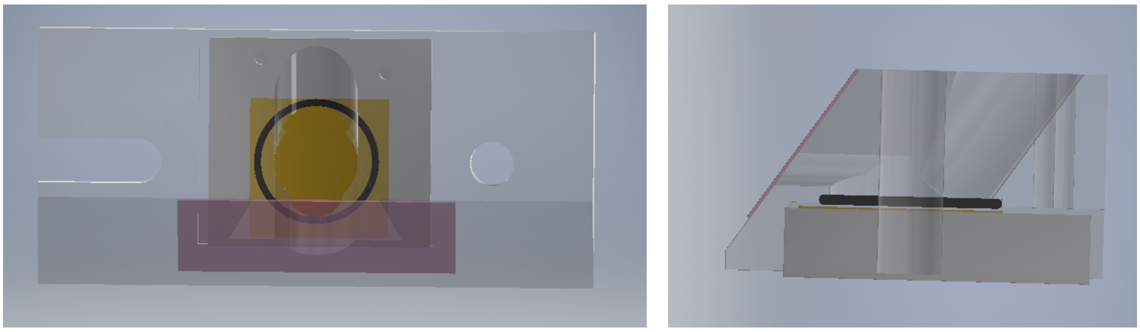

Figure 3.6.: (left) Assembly of S/L TERS sample cell (see part 1 in figure 3.5 for technical drawings), placed on a Au/mica substrate on a spacer (see part 2 in figure 3.5 for technical drawings), with an O-ring between the sample cell and the Au/mica to seal the water reservoir. A glass window (pink) is glued on the sample cell. (right) Side view of assembly of S/L TERS sample cell with Au/mica sample.

3.4. Tip preparation for solid-liquid TERS

To fabricate TERS-active tips (sharp symmetrical pencil-shaped Au tips) electrochemical etching was applied [72]. The ∼ 2 mm long end of a ∼17 mm long Au wire (0.25 mm diameter, 99.995%, Mateck GmbH) was placed in a 1:1 solution of ethanol:fuming HCl in the center of a circular Au counter electrode (CE; 1.0 mm diameter, 99.995%, Mateck GmbH) such that a meniscus was formed (see schematic representation of tip-etching procedure in figure 3.7). This was done by dipping the ∼ 3 mm long end the Au wire in the solution and pulling it out again to keep the ∼ 2 mm long end in the solution. The CE was bent in a circular shape, by the use of a PTFE mold. The Au CE was placed horizontally, just underneath the surface of the etching solution (see figure 3.7). A variable voltage generator of a home-build etching device was used to apply a constant voltage of 2.4 V between the tip and the CE. The applied potential to the Au wire leads to the formation of $AuCl_4^-$, which dissolves in the etching solution [72]:

$$\begin{aligned} Au + 4Cl^- &\longrightarrow AuCl_4^- + 3e^-, \\ Au + 2Cl^- &\longrightarrow AuCl_2^- + e^-, \\ AuCl_2^- + 2Cl^- &\longrightarrow AuCl_4^- + 2e^- \end{aligned} \tag{3.1}$$

Etching occurs fastest in the meniscus formed by the Au wire/liquid/air interface [72]. Once the Au wire at the meniscus becomes too thin to hold the lower ∼ 2 mm of the wire, the lower part of the wire falls off. The tip is connected to a lifting magnet, which is lifting the tip from the etching solution once the current through the electronic circuit is below a threshold value (set in the home-build etching device). Quickly lifting the tip from the solution once the tip etching is completed prevents over-etching of the sharp tip end, which is a prerequisite for TERS-activity of Au tips. Etching times were approximately 6 min per tip.

The Au wire is cleaned with absolute ethanol before etching. After etching, the tip is

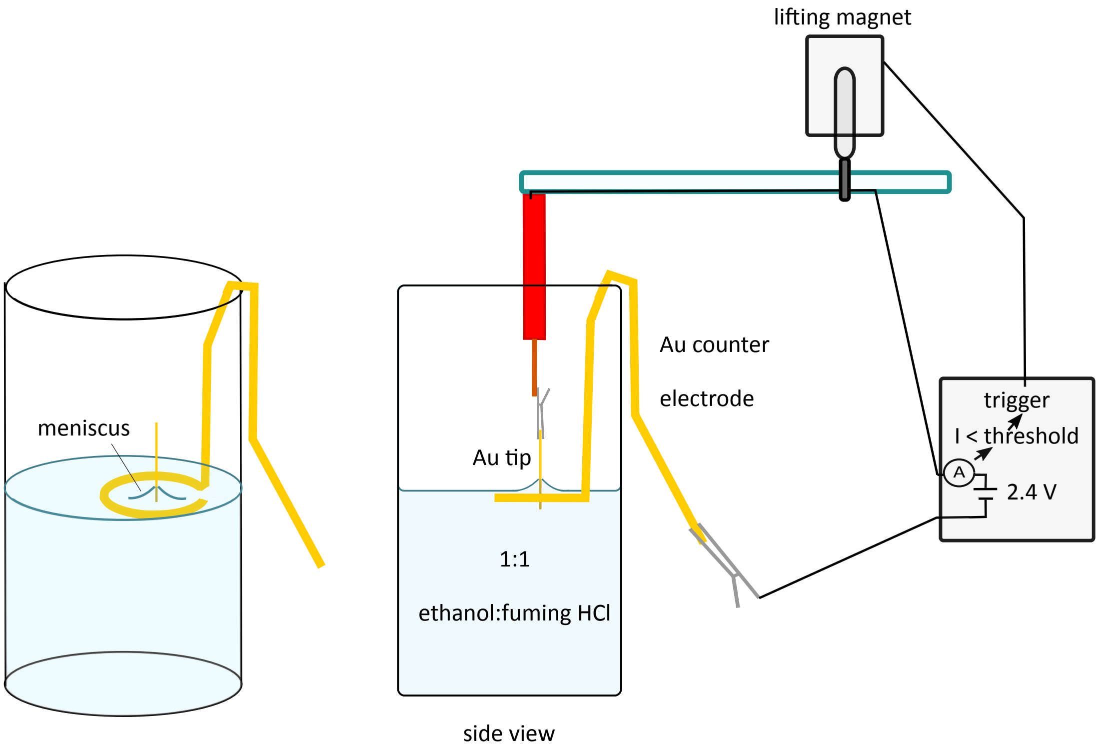

Figure 3.7.: Schematic representation of etching procedure to produce Au TERS tips.

carefully cleaned with ultrapure water: the Au wire, with the etched tip pointing downwards, is hold by tweezers. A wash bottle with ultrapure water is used to add water to the middle of the Au wire in a drop-by-drop manner for ∼10 seconds. The tip is quickly turned around and placed in a piece of foam to dry (in air).

Adding an electrolyte in S/L STM-TERS would lead to Faradaic leakage currents from the side of the Au tip to the sample, disabling a stable electron tunneling between tip and sample. To avoid Faradaic leakage currents from the Au TERS tip in aqueous electrolyte, the tips were coated with Zapon lack (CLOU, Germany). In the coating procedure, a TERS tip, with its etched end upwards, is hold by tweezer and pushed into a droplet of Zapon lack at around 10 mm below the etched end. Then the tip is slowly pulled down, through the droplet of Zapon lack and out of the Zapon lack droplet. The tip is dried in air positioned with its etched tip upwards for several minutes. The pulling and drying procedure was repeated three times to thicken the Zapon coating, thereby lowering the chance on holes in the Zapon coating on the tip.

3.5. Cleaning procedure for (solid-liquid) TERS

TERS is a single molecule-sensitive technique, therefore all glassware, PTFE, PCTFE and FFKM75 parts must be thoroughly cleaned before each experiment and gloves have to be worn when handling the parts. Organic contamination is oxidized by boiling the

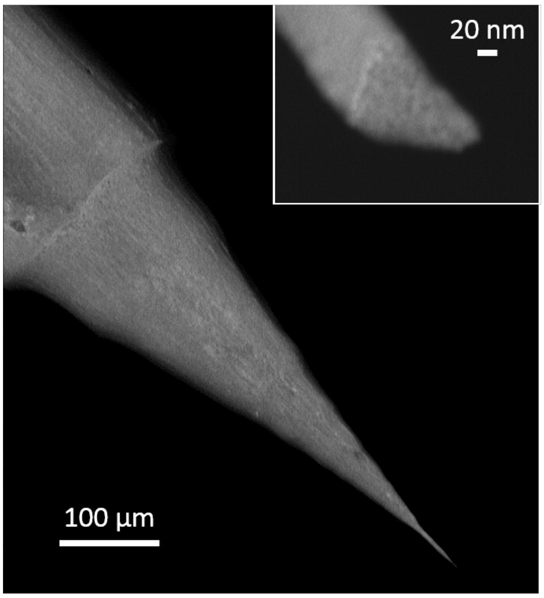

Figure 3.8.: Scanning electron microscopy (SEM) image of etched Au TERS tip.

parts in a 3-5 L glass beaker with 30% nitric acid solution for 20 minutes or by leaving the parts overnight in Piranha solution (sulfuric acid 95% : hydrogen peroxide, 3 : 1). Afterwards the parts are rinsed with copious amounts of ultrapure water (resistivity >18 MΩ/cm from a Milli-Q Integral 3, Merck Millipore). Then a glass beaker containing the parts is filled with ultrapure water and brought to the boiling point. The procedure is repeated for three times, with rinsing the parts with ultrapure water after each boiling step. The parts are left in a clean glass beaker filled with ultrapure water and covered with parafilm until the parts are used, which could be several days. Before using the parts they are dried in an oven at 110°C. This oven is cleaned and only used for drying cleaned glassware, to avoid contamination.
The epoxy glue of the glass window of the sample cell is dissolved in aceton, before cleaning the cell by acid and water.

3.6. Processing of (enhanced) Raman and scanning tunneling microscopy data

To analyze (enhanced) Raman spectra, Raman peaks were fitted with Lorentzian line shapes to extract positions, intensities and FWHM of Raman peaks. The large background signal in SERS and TERS complicates peak fitting. If only one band was fitted, a linear background was fitted (see for example the TERS spectra in figure 4.2). If the entire spectrum was analyzed, background subtraction and scaling were used as described by Lin et al [58]. The background and scaling procedure is explained in Appendix chapter B. In this thesis, all shown TER spectra are raw data (no background of scaling procedure used), except Raman spectrum C in figure 5.3 and all TERS and SERS spectra shown in

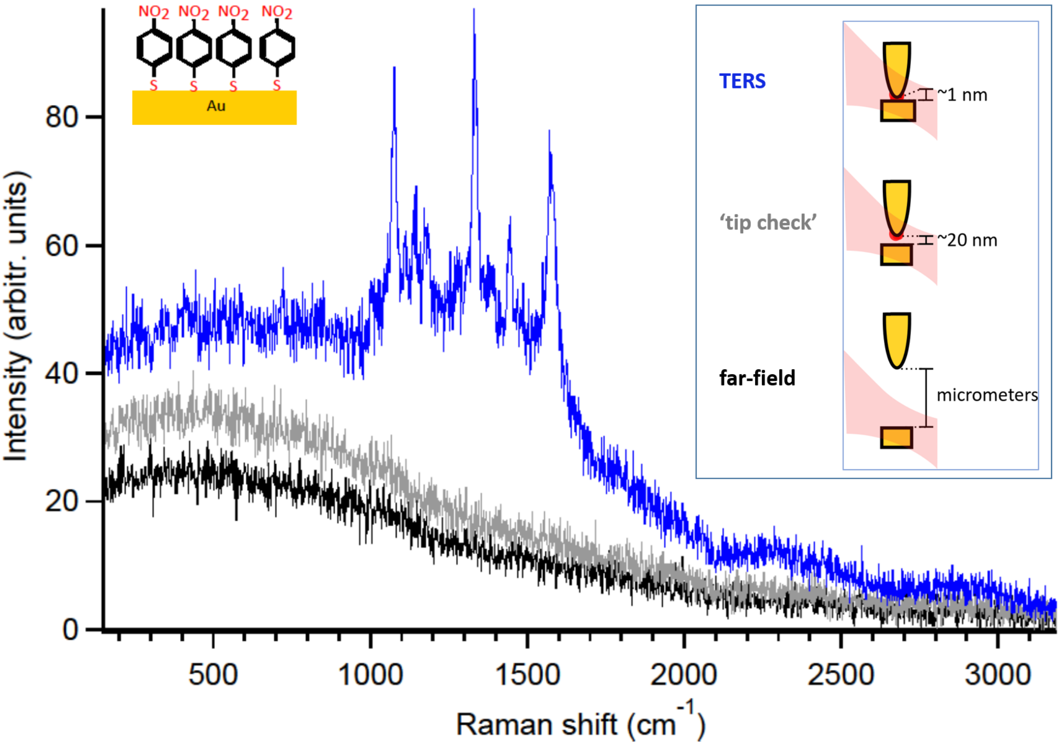

Figure 3.9.: Tip-enhanced resonance Raman spectrum of nitrothiophenol at Au(111)/air interface: tip in tunneling position with setpoint 0.05 nA and bias 0.3 V (blue spectrum), tip retracted 20 nm (grey spectrum) and tip retracted 3 µm (black spectrum). Laser power: 0.61 mW, acquisition time: 2 s. All spectra are averaged over 6 spectra and not background subtracted (raw data).

figure 5.8 and figure A.1. Background subtraction and scaling of the spectra in figure 5.8 and A.1 is discussed in detail in appendix chapter B.
Cosmic ray features ('spikes') in Raman spectra were removed by hand. Raman peaks were fitted using the peak fitting procedure of IGOR Pro.
Image processing of scanning tunneling microscopy images was performed with Gwyddion version 2.47, by using the functions: *level data by mean plane subtraction*, *align rows by their median* and for some images *2D FFT filtering* was used.

3.7. Checks for far-field Raman signal and tip-cleanliness in TERS

In TERS the laser is focused on the apex of the tip, but as the tip is ∼1 nm from the substrate, this means that the laser is also focused at the substrate. Therefore, detected TERS signal also contains far-field Raman signal from the laser focus at the substrate. Furthermore, depending on the roughness of the metal substrate and the cleanliness of the tip, there might be (contagious) SERS signals as well. To discriminate between these effects, and thereby ascertain that the enhanced Raman signal is due to the introduction of a clean tip, a far-field Raman check and tip-cleanliness check are performed in every TERS experiment.

Figure 3.9 shows an example of a far-field Raman check of TERS of nitrothiophenol adsorbed on Au(111), in air. The blue spectrum in figure 3.9 was collected when the TERS tip was in tunneling condition above the nitrothiophenol/Au substrate and the black spectrum in figure 3.9 was collected when the TERS tip was retracted by 3 µm from the nitrothiophenol/Au substrate. In the TER spectrum of nitrothiophenol/Au a broad continuous background and clear Raman peaks of nitrothiophenol appears, while in the far-field Raman spectrum of nitrothiophenol/Au only a continuous background appears. The enhancement of the Raman intensity of the TER spectrum of nitrothiophenol/Au is due to approaching the tip to the substrate.

The next check in a TERS experiment is the cleanliness of the tip. If surface adsorbates would stick to the tip apex or to another SERS-active nanostructure at the surface of the tip, this might lead to a TERS or SERS signal additional to the TERS signal of adsorbates at the substrate. A TERS/SERS signal of tip-adsorbates would show up in every TERS spectrum, regardless of the position of the tip with respect to the substrate. This might lead to erroneous interpretations, e.g. while chemical mapping a substrate by TERS. Tip cleanliness during a TERS experiment can be checked by retracting the tip only far enough to move the near-field around the tip apex away from the molecules adsorbed on the substrate, while still keeping the tip apex in the laser focus to collect TERS/SERS from the tip. In gap-mode STM-TERS, it has previously been shown that retracting the tip 20 nm from the substrate diminishes the TERS intensity to $< 1\%$ of the TERS intensity in tunneling contact [54]. Therefore, a SERS signal obtained while the TERS tip is 20 nm retracted from the substrate indicates the presence of adsorbates in the near-fields around the tip apex or in near-fields of other nanoscale surface structures om the tip surface. The grey spectrum in figure 3.9 was collected when the tip was retracted 20 nm from the nitrothiophenol/Au substrate. This 'tip-check' spectrum shows a continuum background due to presence of the Au substrate and tip in the laser focus, but no Raman peaks can be distinguished from the noise. The 'tip-check' spectrum (grey spectrum in figure 3.9) was collected after the TER spectrum of nitrothiophenol/Au (blue spectrum in figure 3.9), therefore the tip can be considered free of nitrothiophenol during the collecting of the TER spectrum.

Another method to check the cleanliness of a TERS tip is measuring TERS while the TERS tip is approached to a clean substrate. A tip check after a nitrothiophenol/Au TERS measurement would then be measuring TERS while the tip is approached to a clean Au substrate. If the control TERS experiment on the clean substrate does not show Raman peaks, the cleanliness of the TERS tip is confirmed.

4. TERS mapping

One of the strengths of TERS is chemical mapping of surfaces with nanometric laterial resolution. TERS mapping enables characterization of surfaces which possess nanoscale domains or structures, but lacks contrast when measured with scanning probe microscopy [73, 74]. Some mixed self-assembled monolayers (SAMs) are examples of such surfaces [73, 74]. Adsorbing a SAM with functional terminal groups to a substrate is an immediate and simple way to alter the physicochemical properties of the substrate. Understanding under which conditions mixed SAMs form nanoscale patterns at the substrate is of use for rational design of patterned functional surfaces. TERS maps provide feedback for the synthesis of patterned SAM surfaces.

Our TER spectrometer is capable of acquiring TERS maps. To acquire a TERS map, the software of the STM (Picoview) triggers the software of the spectrograph (Labspec). In Picoview different mapping grids can be chosen and STM images can be acquired simultaneously (scan-to-point modus).

Before discussing TERS maps of mixed SAMs in section 4.3, first the lateral spatial limits of TERS mapping in our TER spectrometer are investigated. The upper limit of the lateral size of a TERS map depends on the size and intensity profile of the laser focus on the substrate, which is experimentally shown in section 4.1. In section 4.2 the spatial resolution of TERS measured with our TER spectrometer is investigated to set the lower limit for the step size (pixel size) for the collection of TERS maps.

4.1. Size of laser focus

To abolish the influence of the laser focus on a TERS map, the laser focus should be larger than the mapping area. Furthermore, the laser focus should be 'plane', meaning that TERS intensity from all the spots on the substrate inside the laser focus should be similar. To find out the size and intensity distribution of the laser focus in our TER spectrometer, a TERS map of a homogeneous TERS-active substrate was collected. As a substrate, we chose a self-assembled monolayer (SAM) of alkanethiols/Au(111). The adsorption behavior of alkanethiols on Au is extensively studied [75]. Thiols bind to Au with a high affinity [75]. Therefore, alkanethiols are expected to form a homogeneous monolayer on a atomically flat Au(111) substrate, as shown schematically in the left upper corner of figure 4.1 for butanethiol/Au. The TERS intensity measured on a homogeneous monolayer of butanethiol/Au(111) should essentially be the same for all lateral positions of the TERS tip on the substrate, and only depends on the laser focus.

In figure 4.1 a TERS map of 3×3 µm measured on a butanethiol/Au(111) is shown. The most intense TER spectrum is measured in the pixel numbered with 1, but pixels at a distance of 0.75 µm to 1.5 µm (pixel 2) still show 74% of the TERS intensity of pixel 1 (see spectrum 1 and 2 in figure 4.1). Laterally moving further than 1.5 µm

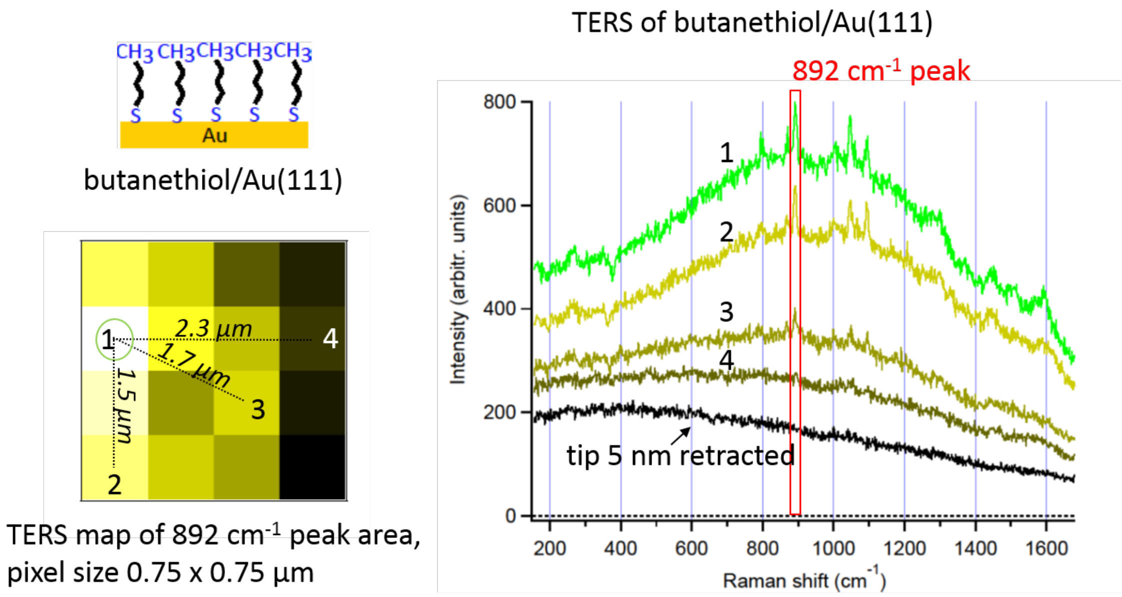

Figure 4.1.: (left) TERS map (4×4 pixels of 0.75 µm) of peak area of 892 cm^{-1} peak of butanethiol/Au(111)/mica. (right) Corresponding TER spectra of numbered pixels in the TERS map (left). Black spectrum (lowest spectrum) is a TER spectrum while the tip was 5 nm retracted. Laser power 0.6 mW, 10 s, 1.0 nA, 0.2 V. Spectra are averages of 5 spectra.

away from the pixel with the most intense TER spectrum leads to a decrease in TERS intensity to 43% of the TERS intensity of pixel 1 (see for example spectrum 3 in figure 4.1). The TERS intensity in a spot that is laterally 2.3 µ away from the most intense TER spot is almost vanished, to 11% of the TERS intensity of pixel 1 (see spectrum 4 in figure 4.1). Spectrum 4 still shows a broad continuum background compared to the spectrum where the TERS tip is 5 nm retracted from the substrate (the black spectrum in figure 4.1. The estimated laser focus size (FWHM) based on the TERS map in figure 4.1 has a radius of no less than 0.75 µm. The radius of the laser focus measured by the intensity profile of a TERS map is larger than the radius of the focus of 507 ± 80 nm obtained by pictures of the laser focus taken by the CMOS camera in our TER spectrometer [69]. The estimated laser focus size shows that TERS mapping of squared surface areas up to ∼1×1 µm should not show a larger than 50% change of TERS intensity between different pixels caused by the intensity profile of the laser focus. Note that for this estimation the center of the laser focus is in the middle of the TERS map.

4.2. Measuring the spatial resolution of TERS

The lateral spatial resolution of TERS determines the lower limit of the pixel size in TERS mapping. A common way to check the spatial resolution of TERS, is collecting TER spectra while scanning the TERS tip laterally over a carbon nanotube physisorbed to a flat substrate [76]. Carbon nanotubes are chosen for this, because of their 1-dimensional nature and because the large resonant Raman cross-sections of their phonon modes results in a high signal-to-noise ratio [77]. TER spectra are collected while scanning the TERS tip laterally over the carbon nanotube. Raman bands in the collected TER spectra are fitted to withdraw the peak intensities. Peak intensities are plotted against lateral position of the tip to calculate the TERS lateral spatial resolution. Various definitions of the TER lateral spatial resolution exist [66]. In this dissertation work, the lateral spatial resolution of TERS is defined as the lateral movement of the tip in which the intensity of a Raman vibration goes from the intensity in the far-field to the maximum intensity in the near-field.

Results of a method to check the lateral spatial resolution of our TER spectrometer are shown in figure 4.2. Simultaneous TER spectral acquisition and STM imaging were applied on a sample of multi-walled carbon nanotubes (MWCNT) adsorbed at a Au(111)/mica substrate. The STM topography image in the bottom of figure 4.2 shows the position of a MWCNT with a diameter of ∼8 nm. The grey, brown and black arrows on top of the STM topography image show the positions of the tip where TER spectra were collected. The left window in figure 4.2 shows two representative TER spectra in black and brown, which were acquired at the positions indicated by the black and brown arrows in the bottom STM image in figure 4.2, respectively. The black spectrum is a near-field spectrum of the MWCNT, where two Raman peaks appear at 1330 and 1590 cm^{-1}. The peak at 1330 cm^{-1} is assigned to vibrations of disordered SP^3-hybridized carbon ('D-band') and the peak at 1590 cm^{-1} is assigned to SP^2-hybridized, graphite-like carbon ('G-band') [78]. The D-band and G-band are also visible in the far-field in the brown TERS spectrum, although much less intense than in black spectrum. The blue fits of the 1330 and 1590 cm^{-1} peaks in the black spectrum are examples of the peak fitting procedure with a linear background to extract the peak intensities. The integrated peak areas of the D- and G-band of the TERS spectra collected by two line-scans over the MWCNT (along the red line drawn in the STM image in the bottom of figure 4.2) are shown by the blue traces in the right window of figure 4.2. To this graph, a STM-topography profile along the TERS line-scan is added. The lateral spatial resolution of the TERS tip measured in this way is 12.6 nm. However, it should be noted that if a smaller step size (the TERS step size in this experiment was 12.6 nm) would be used, the measured TERS resolution might be smaller.

4.3. TERS mapping of a binary SAM

Introduction

In this section, the TERS mapping capability of the TER spectrometer is shown by TERS mapping of a binary SAM. For single component thiolated SAMs, the almost-covalent bond of the thiol groups to Au (∼50 kcal/mol) stears the formation of a densily packed SAM where thiol molecules stand up on the Au surface [79]. The clear understanding of single-component SAMs has lead to a good control over the fabrication of homogeneous SAMs. However, as soon as a binary SAM is produced, the control over the surface homogeneity is lost. TERS was proposed as a method to gain nanoscale feedback on the fabrication of binary SAMs, which contains parameters such as the ratio between the two

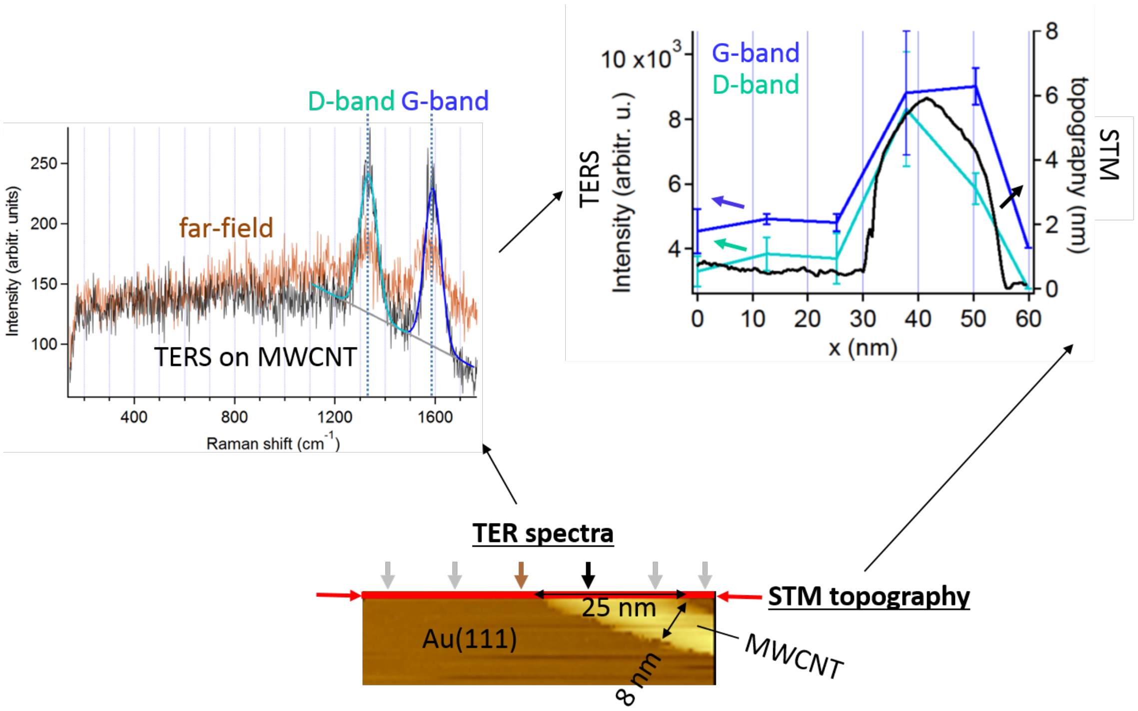

Figure 4.2.: (bottom) STM topography image with colored arrows to display the positions where TERS spectra were acquired of which two representative TER spectra are shown (left window). The bands at 1330 and 1590 cm^{-}1 in the collected TER spectra of two line scans along the red line in the bottom STM image were fitted and the integrated peak areas are plotted against measurement position (right window). A STM topography profile along the red line of the STM image is added for comparison in the right window.

thiolated species, annealing time and annealing temperature.
We investigated a binary SAM of octanethiol and nitrothiophenol on Au(111). Mixtures of an alkanethiol with a conjugated thiol have shown domain formation in SAMs in previous investigations [80]. Therefore, the mixture of octanethiol and nitrothiophenol was chosen as a good starting point to study the influence of the ratio octanethiol:nitrothiophenol, annealing time and annealing temperature on domain formation.

Sample preparation

SAM of octanethiol/Au(111) and SAM of nitrothiophenol/Au(111): 150 nm Au was evaporated (Edwards FL400 Auto 306 thermal evaporator) on top of cleaved mica sheets (Plano GmbH, Germany). Au/mica substrates were flame annealed for > 6 minutes, cleaned with ultrapure water and dried in an oven. The samples were immersed either in 0.5 mM octanethiol in toluene or in 0.5 mM nitrothiophenol in ethanol for several hours. Then the samples were thoroughly cleaned with the used solvent (toluene or absolute ethanol) and dried under an argon stream.
Binary SAM of octanethiol and nitrothiophenol*: A piece of Au(111) on mica was immersed in a toluene solution which contains 30% octanethiol and 70% nitrothiophenol for 24 hours at 60 °C. The surface was then removed from the thiol solution, rinsed with toluene and underwent annealing. The annealing process involved the immersion of the substrate in argon gassed toluene at 60 °C for 40 days. After annealing, the substrate was taken out of the annealing solution and rinsed with toluene.
* Binary SAMs were prepared by Nikolaos Nianias, Supramolecular Nanomaterials and Interfaces Laboratory, EPFL, Switzerland.

Results

With our TER spectrometer, TERS maps are collected by moving the TERS tip to different spots on the sample, while residing inside the laser focus. In the right top panel of figure 4.3 TER spectra of SAMs of octanethiol/Au(111) (blue spectrum) and nitrothiophenol/Au(111) (red spectrum) are shown. Both TER spectra are representative spectra when a TERS-active tip was approached to the SAMs. TER spectra with similar peak positions to the purple spectrum in the right top panel of figure 4.3 were collected on some places on binary octanethiol/nitrothiophenol SAMs.
The TERS maps of the 1345, 1454 and 1534 cm^{-1} peak intensities of the binary SAM (bottom of figure 4.3) show the heterogeneous distribution of the purple TERS spectral profile on the mixed SAM substrate. None of the spectra of the TERS maps showed the same profile as the TER spectra of SAMs of octanethiol/Au(111) and nitrothiophenol/Au(111). To confirm that the contrast of the TERS maps of the binary SAM is due to the sample, and not due to the technique, a TERS map of nitrothiophenol/Au(111) was acquired as a reference. The nitrothiophenol/Au(111) TERS map of the 1330 cm^{-1} peak intensity shows some contrast, but this is less compared to the contrast of the binary SAM TERS maps.
The TERS maps of the 1345, 1454 and 1534 cm^{-1} peak intensities of the binary SAM are not exactly the same (see bottom of figure 4.3), which means that the ratio between 1345, 1454 and 1534 cm^{-1} peak intensities varies in the pixels of the TERS map of the binary SAM.

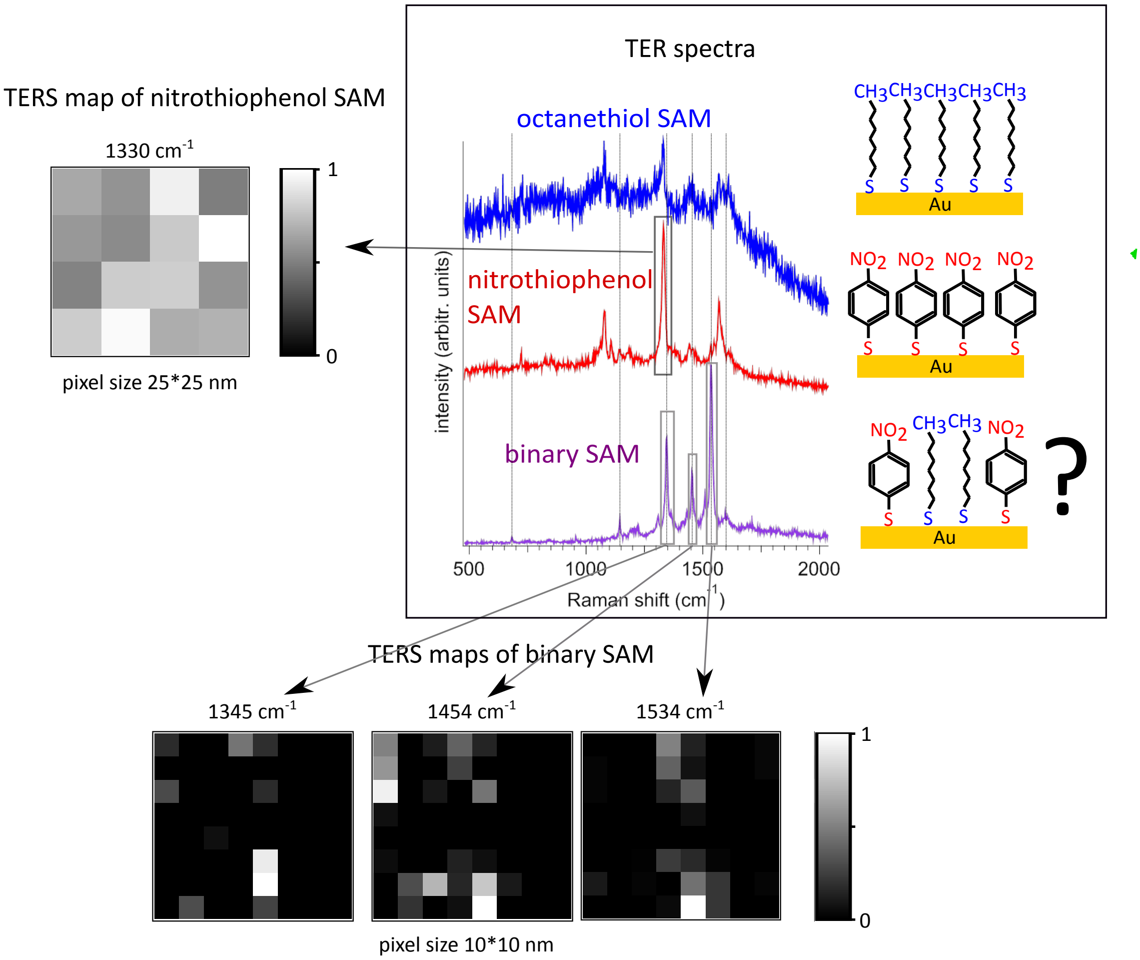

Figure 4.3.: (right top panel) TER spectra of octanethiol/Au(111), nitrothiophenol/Au(111) (laser: 0.13 mW, 5 s, STM: 0.1 nA, 0.04 V) and a mixture of octanethiol and nitrothiophenol/Au(111) (laser: 0.61 mW, 2 s, STM: 0.1 nA, 0.4 V), with corresponding schematic representations of the SAMs on Au substrates. (left) TERS map of the integrated area of the 1330 cm^{-1} peak of TERS spectra of a nitrothiophenol SAM/Au(111). (Bottom) TERS maps of the integrated area of the 1345, 1454 and 1534 cm^{-1} peaks of a binary SAM of octanethiol and nitrothiophenol on Au(111). In all TERS maps, a TER spectrum was collected in the middle of every of the 8×8 pixels. All TERS maps are normalized to the most intense pixel.

Discussion

Mixing two thiolated species to form a binary SAM on Au(111) could lead to several scenarios: (1) The two thiolated species would phase-separate and form domains; (2) the thiols would fully mix, and no domains would form; (3) the two thiols undergo a reaction, which would lead to (several) new chemical species; (4) the thiols are (partly) lost from the surface due to annealing; (5) one of the thiols has a much larger affinity for the substrate and therefore only one of the thiols binds to the substrate.

None of the pixels of TERS maps of the binary SAM show a spectrum similar to the TERS spectra of octanethiol or nitrothiophenol. Therefore, the last scenario of one species having a higher affinity to bind to the Au substrate than the other species, is ruled out. Furthermore, the formation of domains larger than the lateral spatial resolution of 12.6 nm of the TER spectrometer is ruled out. Even more, if domains smaller than 12.6 nm would form, a linear combination of the TER spectra of octanethiol and nitrothiophenol would be expected to appear in some of the measured pixels of the TERS map of the binary SAM. The TER spectral profile which is heterogeneously distributed on the mixed SAM substrate (purple TER spectrum in figure 4.3) is not a linear combination of the TER spectra of octanethiol and nitrothiophenol. Therefore also the formation of domains with a diameter of less than 12.6 nm is ruled out.

The purple TER spectrum in figure 4.3 might be a new chemical species. Searching literature did not yet give us insight into the chemical species causing the purple TER spectrum. The varying ratio between 1345, 1454 and 1534 cm^{-1} peak intensities in the TERS map of the binary SAM might be due to different orientations of the new chemical species [81]. Another possibility is that nitrothiophenol and octanethiol interact so strong, that their Raman peaks are shifted. Annealing did not empty the substrate, as the purple spectrum shows up in many spots on the substrate. However, partial loss of thiols from the substrate due to annealing could not be ruled out. Less molecules in the focus would lead to a smaller TERS signal, which could be a reason that TERS spectra of the individual thiolated species could not be resolved from the signal to noise ratio, with the used laser power and acquisition time. A partial loss of thiolated species from the Au substrate might let the residing thiolated species at the substrate lay more flat. This might reduce or vanish some of the Raman bands, because TERS is only sensitive to a molecule's change in polarizability in the direction along the tip axis.

Outlook

The source of the measured TERS spectral profile heterogeneously distributed over the substrate could not be assigned. To clarify the influence of annealing on both thiolated species on Au(111), TERS should be measured from reference samples of nitrothiophenol/Au(111) and octanethiol/Au(111) which underwent the same annealing procedure as the binary substrate.

5. Nucleation of CuBTC MOF on a metal substrate

5.1. Introduction

Metal-organic frameworks (MOFs) have emerged as new three-dimensional functional designer materials. MOFs consist of a three-dimensional network of organic linkers coordination bound to metal ions creating well-defined pores. These pores can be used for applications ranging from gas storage and separation to sensing, catalysis and electrical energy storage [82, 83]. To be able to make use of the mentioned applications in nanoscale devices, porous MOF nanomodules could be added on the devices. As these nanomodules will be hard to position in a controlled way to the nanodevice (top-down approach), they would ideally be produced directly at the device by molecular self-assembly (bottom-up approach). For the local self-assembly of MOF nanomodules the nucleation of MOF growth at the substrate has to be well understood. How does a MOF nucleate at a substrate? At which substrates can a MOF nucleate? How does the nucleation of MOF influence the homogeneity of the final MOF film or pattern?

We limited our study to the surface nucleation and growth mechanisms of one of the best studied MOFs: $Cu_3(BTC)_2$ (HKUST-1, CuBTC MOF)[84]. CuBTC MOF consists of a network of Cu ions linked by benzene-1,3,5-tricarboxylic acid (BTC, trimesic acid, TMA, see figure 5.1). A common way to nucleate CuBTC MOF growth at a substrate is by adsorbing a self-assembled monolayer (SAM) to the substrate [85]. Munuera et al. used a patterned SAM substrate to nucleate CuBTC MOF thin films on desired places only at the substrate. They used atomic force microscopy to show that CuBTC MOF nucleates at carboxyl-terminated regions and not at CH_3-terminated regions [86]. The termination of the SAM can not only influence the nucleation, but can also determine with which crystal facet a MOF crystal grows on the substrate [87, 88, 85]. This is contradictory to later reports of other research groups, which were following the published protocols for CuBTC MOF oriented growth on top of SAMs resulted in growth of several crystal facets [89, 90]. As the nucleation mechanism on top of a SAM is not clear and as a SAM layer could possibly interfere with the functionality of a MOF nanostructure, our aim is to understand the nucleation of MOF on a metal substrate directly, without any anchoring layer in between. There is a very limited number of studies reporting on the nucleation mechanism of CuBTC MOF grown at a metal substrate directly. Earlier work from our group reports that CuBTC MOF nucleates at polycrystalline Cu substrates by applying a potential of > 0 V to the Cu substrate vs. a Cu reference electrode [91]. From the same study followed that the first step during electrochemical nucleation of CuBTC MOF is the adsorption of BTC to the Cu surface at potentials of < 0 V vs. Cu. The Buck group has shown that CuBTC MOF nucleates at an electrochemically deposited monolayer of Cu on Au(111) [92, 93]. In the reports of the Buck group the first step was deliberately adsorbing a monolayer of BTC to the Cu monolayer/Au(111). Summerfield

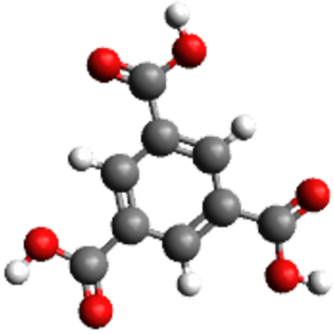

Figure 5.1.: The molecular structure of benzene-1,3,5-tricarboxylic acid consisting of carbon (grey), oxygen (red) and hydrogen (white).

et al. [89] found that CuBTC MOF nucleates at Au(111), and nucleation follows after accumulation of physisorbed material. Biemmi et al. [87] reported that CuBTC MOF does not nucleate at polycrystalline Au. However, it might not be correct to compare the reports of Summerfield et al. [89] and Biemmi et al. [87], because these studies use a different preparation of the Au substrates and a different procedure of CuBTC nucleation. Summerfield et al. used Au(111) substrates as they received them from their supplier, while Biemmi et al. cleaned their polycrystalline Au substrates with piranha solution and afterwards 20 minutes by oxygen-plasma. Furthermore, both reports use a different method to grow CuBTC: Summerfield et al. used a dipping scheme for layer by layer growth , while Biemmi et al. left their substrates in a filtrated solvothermal synthesis mixture.

The nucleation mechanism of CuBTC MOF on top of a metal substrate is still unclear, although the first step seems to be adsorption of BTC [91, 89, 92, 93]. Therefore, in this chapter the adsorption of BTC to a metal substrate will be investigated. For this, we use a well-defined Cu substrate, which is prepared by under potential deposition (UPD) of a monolayer of Cu on Au. UPD deposited Cu also has the advantage that SO_4^{2-} ions from the UPD solution adsorb on the Cu monolayer. These adsorbed SO_4^{2-} ions are expected to shield the Cu monolayer from adsorption of oxygen when the sample is taken out of the oxygen-free UPD solution into the oxygen containing ambient atmosphere [94]. This is expected to diminish oxidation of the Cu monolayer. BTC molecules will displace the adsorbed SO_4^{2-} ions, when the sample is left in a BTC containing solution [94].

In section 5.2 the experimental details of the preparation of samples and of cyclic voltammetry experiments applied in this chapter are described. In section 5.3 the interaction of BTC with its environment (defined here as water, air or Cu ions) is investigated by applying conventional Raman spectroscopy. In section 5.4 the adsorption geometry of BTC on a well-defined Cu layer was investigated by TERS in air and in water.

5.2. Experimental details

Sample preparation

Benzene-1,3,5-tricarboxylic acid (BTC; Alfa Aesar, 98%), Cu(II) sulfate pentahydrate (Aldrich), sulfuric acid (Merck, Suprapur, 96%) absolute ethanol (Sigma Aldrich, 99.9%) were used as received. Ultrapure water (resistivity >18 MΩ/cm) was taken from a Merck MilliQ Integral system.

Cu/Au/mica substrates were prepared by cleaving mica sheets (Plano GmbH, Germany) and evaporating 150 nm Au on top (Edwards FL400 Auto 306 thermal evaporator). Au/mica substrates were flame annealed for 6 minutes, cleaned with ultrapure water and dried in an oven before copper under potential deposition (CuUPD). CuUPD on top of Au/mica substrates was performed as described by Cebula et al. [94]. A three electrode setup in a homebuild glass H-cell connected to a potentiostat (Solartron SI 1286). The reference electrode was a Cu wire that was left for ∼15 seconds in 25% nitric acid in water and afterwards put shortly under a stream of ultrapure water, before inserting it in the electrolyte (10 mM $CuSO_4$ - 50 mM H_2SO_4 aqueous solution). The counter electrode was a platinum wire that was annealed by a torch and cleaned with ultrapure water before inserting it in the electrolyte. The electrolyte was degassed by bubbling with 6N argon for at least 20 minutes. Cu was deposited at a potential of 0.01 V vs. a Cu reference electrode for 65 seconds.

After CuUPD the CuUPD/Au/mica substrate was immediately transferred to a degassed 1 mM BTC/water solution. After 10 minutes, the substrate was removed from the BTC/water solution and thoroughly cleaned with ethanol and dried under argon.

Density functional theory calculations

Gas phase density functional theory (DFT) calculations were performed by Denis Andrienko (Max Planck Institute for Polymer Research, Mainz, Germany). More information on DFT calculations can be found in Appendix chapter D.

5.3. Interaction of BTC with its environment

Introduction

To support the interpretation of TERS results of BTC adsorbed to CuUPD/Au under water in section 5.4, in this section the interaction of BTC with other BTC molecules, water molecules and with Cu ions was studied by conventional Raman spectroscopy.

In pure BTC, the carboxyl groups facilitate self-assembly in two dimensions [95]. First, a two-dimensional structure is formed by intermolecular hydrogen-bonding between carboxyl groups, as shown in figure 5.2A. Hydrogen-bonding of all three carboxyl groups of BTC to carboxyl groups of other BTC molecules forms an infinite two-dimensional hexagonal structure. The cavities of this hexagonal structure are filled by interpenetration of other hexagonal networks (see figure 4 in [95]), thereby forming a three-dimensional structure.

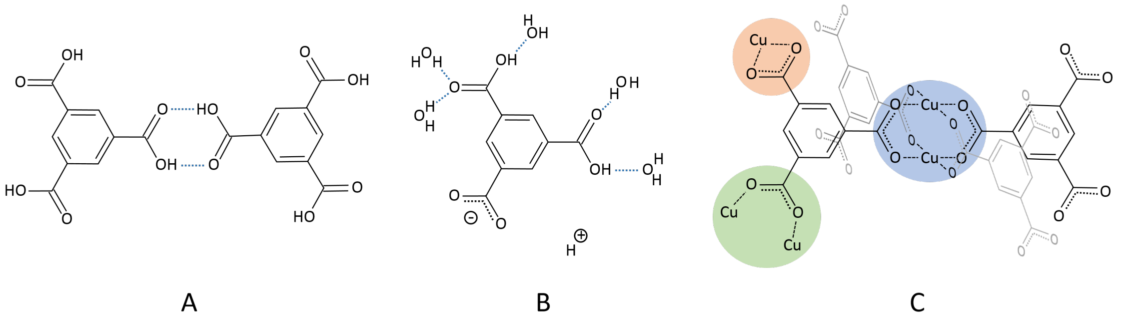

Figure 5.2.: Interactions of carboxyl groups of BTC with their environment. (A) Intermolecular hydrogen-bonds between carboxyl groups of BTC. (B) Hydrogen-bonding between BTC and water, and formation of carboxylate. (C) Different coordination bonds between carboxylate and Cu: (orange) carboxylate as a bidentate chelating ligand, (green) as a bidentate bridging ligand and (blue) as a bidentate bridging ligand inside a CuBTC MOF paddlewheel .

When BTC encounters water molecules, carboxyl groups of BTC hydrogen-bind to water (see figure 5.2B). However, these hydrogen bonds are not sufficient to efficiently dissolve the hydrophobic benzene ring of BTC in water in water. BTC dissolves in water by a maximum of 11 mmol per kg water at 298 K [96]. The pKa values of the three carboxyl groups of BTC are 2.1, 4.1 and 5.2 [97]. The pH of a saturated BTC in water solution at room temperature was 2.5. At this pH 73 % of the dissolved BTC molecules contain one deprotonated carboxyl group, while the rest of the BTC molecules are fully protonated.
There are various possibilities for coordination bonds between BTC and Cu ions, as shown in figure 5.2C. Carboxylate serves as a bidentate chelating ligand when two oxygens of one carboxylate bind to one Cu ion (see the orange circle in figure 5.2)C) and as a bidentate bridging ligand when two oxygens of one carboxylate bind to two Cu ions (see the green circle in figure 5.2C) [98]. The carboxylates of BTC inside CuBTC MOF act as bidentate bridging ligands to form the so-called 'paddlewheel' structure (see the blue circle in figure 5.2)C. A CuBTC paddle-wheel is formed when one Cu ion is bound to one of the oxygen atoms of carboxylates of four different BTC molecules, while another Cu ion binds to the other oxygen atom of those carboxylates [84].

To study the interaction of BTC molecules with the mentioned environments, Raman spectra of BTC powder, BTC dissolved in water and CuBTC MOF were collected. Furthermore, gas-phase DFT calculations were performed to link the vibrational modes of BTC to their corresponding Raman peaks. To imitate BTC in the different environments, BTC molecule(s), water molecules and Cu ions were fixed in space in the gas-phase DFT calculations.

Results

The interaction of BTC with other BTC molecules was investigated by the Raman spectrum of BTC powder (spectrum A in figure 5.3). BTC powder contains interpenetrating two-dimensional hexagonal networks of hydrogen-bonded BTC molecules [99]. To assign the peaks of the Raman spectrum of BTC powder a Raman spectrum of a BTC molecule hydrogen-bound to three other BTC molecules was calculated by DFT (spectrum B in figure 5.3). As these hydrogen-bonded two-dimensional networks are large, the BTC molecules on the edges of the network are negligible in the Raman spectrum of BTC powder. Therefore only the vibrations of the BTC molecule in the middle of the BTC tetramer are shown in the DFT calculated spectrum. The peak positions of the gas-phase DFT calculated Raman spectrum of BTC in the middle of a BTC tetramer correspond well with the peak positions of the experimental Raman spectrum of BTC powder, except for the large peak at 2920 cm^{-1} in the DFT calculated spectrum, where there is no peak visible in the experimental spectrum of BTC powder. Note that in our case, only the peak positions of the gas-phase DFT calculated Raman spectrum can be compared with the experimental Raman spectrum, because the width and peak area of these gas-phase DFT calculated peaks do not have a physical meaning (an explanation can be found in Appendix chapter D). Furthermore, gas-phase DFT calculated Raman peak positions generally are overestimated. Therefore, DFT calculated Raman peak positions are scaled, based on experimental Raman spectra. Details on the scaling of DFT calculated Raman spectra can be found in Appendix chapter D.

To investigate the interaction of BTC with Cu ions, a Raman spectrum of CuBTC MOF was acquired (spectrum C in figure 5.3). BTC inside CuBTC MOF is coordination-bound with three carboxylates to Cu ions (see figure 5.2C). The Raman spectrum of BTC bound with every carboxylate to a Cu atom was calculated by gas-phase DFT (spectrum D in figure 5.3) to assist in the assignment of the experimental Raman peaks to vibrations of CuBTC MOF. The peak positions of the measured Raman spectrum of CuBTC MOF overlap well with the peaks of the gas-phase DFT calculated spectrum, except for the broad peak around 200 cm^{-1} and the two overlapping peaks at 460 and 502 cm^{-1} in the experimental Raman spectrum where there are no corresponding peaks in the DFT calculated spectrum. Furthermore, at 3098 cm^{-1} the DFT calculated spectrum shows a peak while in the experimental Raman spectrum there is no corresponding peak observed.

The interaction of BTC with water was investigated by acquiring a Raman spectrum of a saturated solution of BTC in water. As BTC dissolves only by a maximum of 11 mmol/kg water at 298 K [96], the Raman spectrum of a saturated solution of BTC in water contains large peaks for the vibrations of water. These Raman peaks of water overlap with the Raman peaks of BTC, thereby complicating the analysis of Raman peaks of BTC. This complication was solved by retracting a Raman spectrum of ultrapure water from the Raman spectrum of a saturated aqueous solution of BTC, which both were measured in the same sample cell and with the same settings for the laser power and acquisition time. The Raman spectrum of a saturated solution of BTC in water, after retraction of a Raman spectrum of ultrapure water, is spectrum E in figure 5.3. For assigning the Raman peaks of BTC in water, a Raman spectrum of a BTC molecule with two water molecules hydrogen-bound to every carboxyl group was calculated by gas-phase DFT (spectrum F in figure 5.3). The peak positions of the gas-phase DFT calculated spectrum of BTC with six water molecules shows a good agreement with the peak positions of the experimental Raman spectrum of BTC in water. The large peak at 2830 cm^{-1} in the DFT calculated spectrum of BTC with six water molecules did not appear

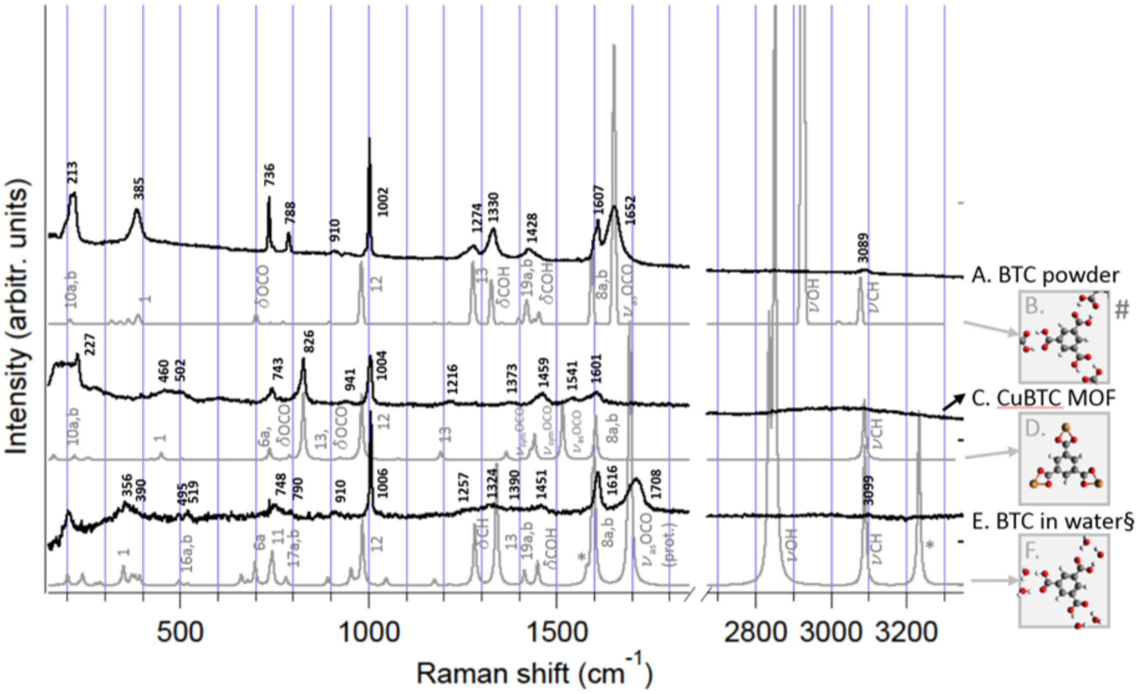

Figure 5.3.: Experimental Raman spectra and corresponding DFT calculated Raman spectra. From top to bottom: (A) BTC powder and (B) DFT calculated spectrum of a fully protonated BTC molecule intermolecularly hydrogen bonded via its carboxyl groups to three other BTC molecules. (C) CuBTC MOF and (D) DFT calculated spectrum of fully deprotonated BTC with every carboxylate bound to a Cu atom. (E) BTC dissolved in water and (F) DFT calculated spectrum of fully protonated BTC with six water molecules. The shoulder and peak marked with * are water vibrations.

Laser power and measurement times are for the spectrum of BTC powder 21 mW, 3 s, for CuBTC MOF 1.9 mW, 20 s and for BTC in water 19 mW, 150 s. Peaks were fitted with Lorentzian functions to extract the mentioned peak positions. Experimental Raman spectra were normalized to the peak area of the 1000 cm^{-1} peak. The spectra are offset for clarity.

In the DFT calculated Raman spectrum of the BTC tetramer, marked with #, only the Raman bands of the BTC molecule in the middle of the tetramer are shown, because this molecule resembles the large majority of BTC molecules inside a large two-dimensional hexagonal structure which are bound to three other BTC molecules, compared to the minority of BTC molecules at the side of the structure which are only bound to one or two other BTC molecules.

§ From the Raman spectrum of BTC in water a Raman spectrum of ultrapure water was retracted.

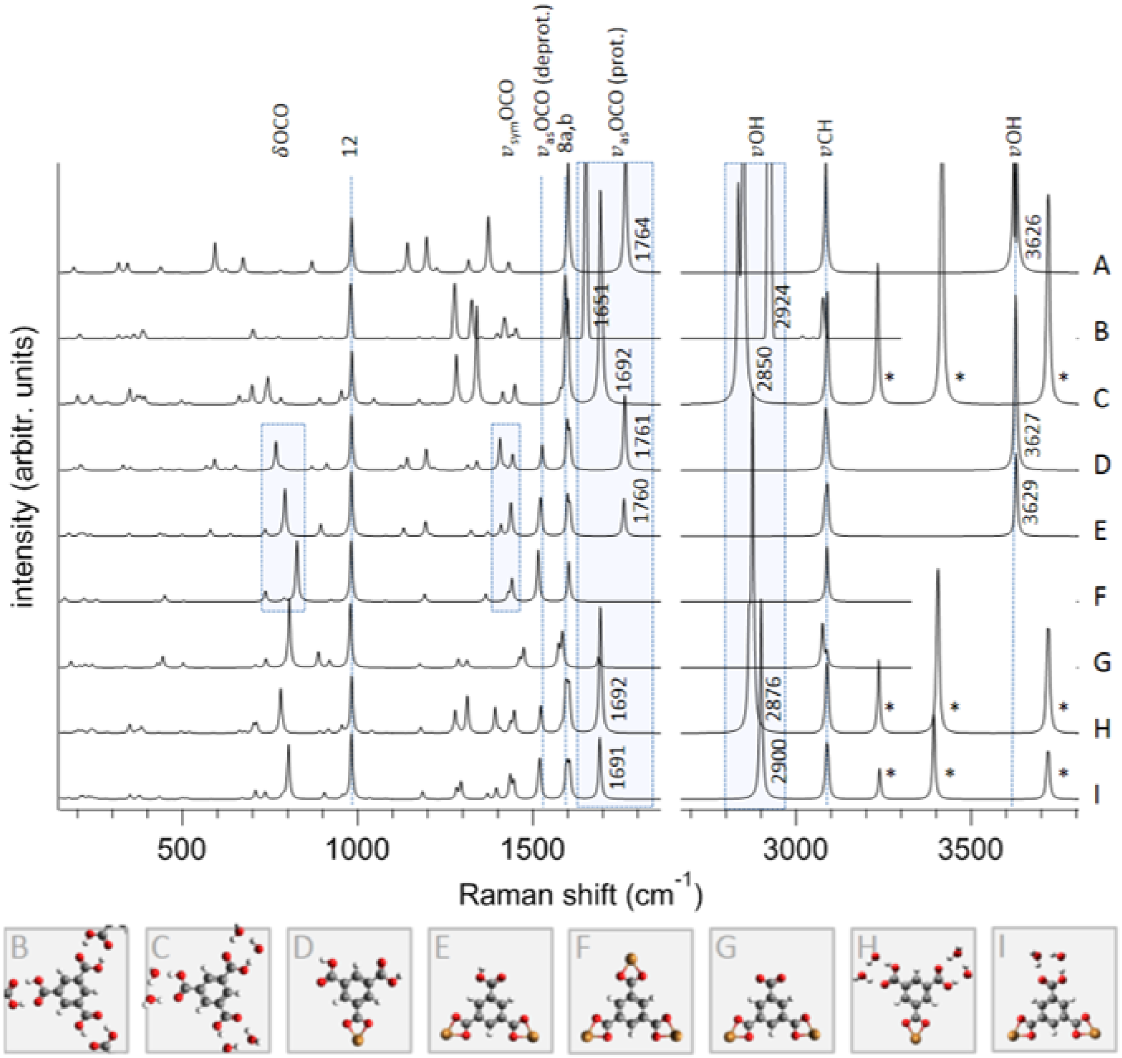

Figure 5.4.: Overview of DFT calculated Raman spectra of (A) BTC monomer, (B) BTC hydrogen-bonded to three other BTC molecules, (C) $BTC_1(H_2O)_6$, (D) BTC_1Cu_1, (E) BTC_1Cu_2, (F) BTC_1Cu_3, (G) deprotonated BTC_1Cu_2, (H) $BTC_1Cu_1(H_2O)_4$, (I) $BTC_1Cu_2(H_2O)_2$. Peaks marked with an asterisk are νOH vibrations of water.

Table 5.1.: Overview of DFT calculated Raman vibrations of BTC interacting with water and Cu and their corresponding Raman activities.

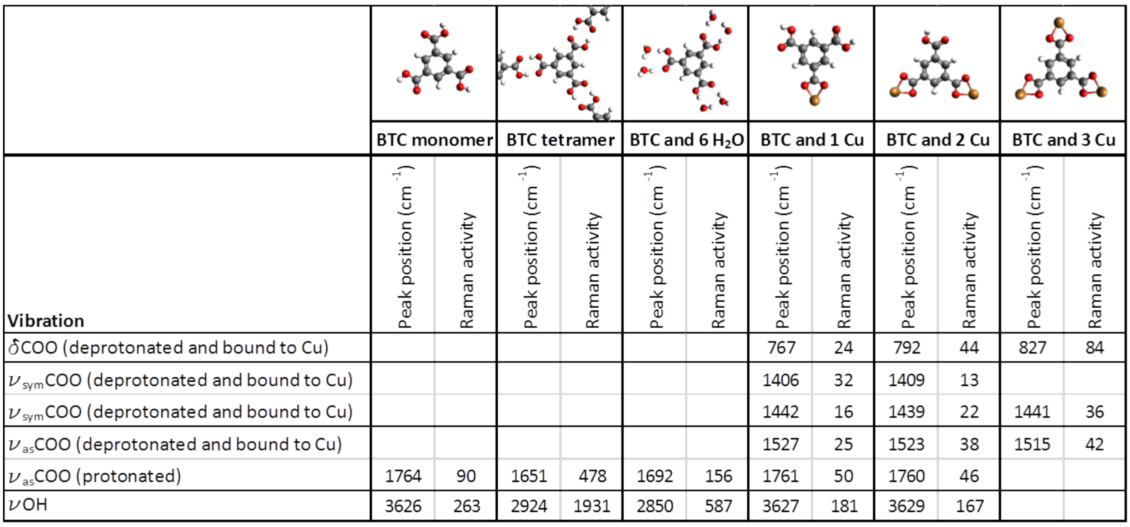

	BTC monomer		BTC tetramer		BTC and 6 H_2O		BTC and 1 Cu		BTC and 2 Cu		BTC and 3 Cu	
Vibration	Peak position (cm^{-1})	Raman activity	Peak position (cm^{-1})	Raman activity	Peak position (cm^{-1})	Raman activity	Peak position (cm^{-1})	Raman activity	Peak position (cm^{-1})	Raman activity	Peak position (cm^{-1})	Raman activity
δCOO (deprotonated and bound to Cu)							767	24	792	44	827	84
ν_{sym}COO (deprotonated and bound to Cu)							1406	32	1409	13		
ν_{sym}COO (deprotonated and bound to Cu)							1442	16	1439	22	1441	36
ν_{as}COO (deprotonated and bound to Cu)							1527	25	1523	38	1515	42
ν_{as}COO (protonated)	1764	90	1651	478	1692	156	1761	50	1760	46		
νOH	3626	263	2924	1931	2850	587	3627	181	3629	167		

in the experimental Raman spectrum of BTC in water. Furthermore, the first peak in the experimental Raman spectrum, at 200 cm^{-1}, was not analyzed further, because its position might be erroneous due to the close proximity to the edge filter cutoff at 150 cm^{-1}.

Discussion

By analyzing the Raman spectra in figure 5.3, we observe general features which indicate how BTC interacts with its environment. The most obvious difference in the Raman spectra of BTC powder, CuBTC MOF and BTC in water are the large peak at 1652 cm^{-1} in the spectrum of BTC powder and the large peak at 1708 cm^{-1} in the spectrum of BTC in water, where there is no peak in this region in the spectrum of CuBTC MOF. These peaks were assigned to a ν_{as}C-O_2 vibration of carboxyl based on gas-phase DFT calculations. In the spectrum of CuBTC MOF, the peak at 1541 cm^{-1} was assigned to a ν_{as}C-O_2 vibration of carboxylate bound to Cu. In gas-phase DFT calculated Raman spectrum of a monomer BTC (see spectrum A in figure 5.4) the ν_{as}C-O_2 vibration of its carboxyl groups appears at 1764 cm^{-1}. In the gas-phase DFT calculated Raman spectra, hydrogen bonding with water redshifts the ν_{as}C-O_2 vibration of carboxyl groups of a BTC monomer by 72 wavenumbers to 1692 cm^{-1} (see spectrum C in figure 5.4), while hydrogen bonding with carboxyl groups of other BTC molecules redshifts the ν_{as}C-O_2 vibration by 113 wavenumbers to 1651 cm^{-1} (see spectrum A in figure 5.4). In the gas-phase DFT calculations, deprotonation of carboxyl and binding to Cu redshifts the ν_{as}C-O_2 vibration even further, by 249 wavenumbers to 1515 cm^{-1} (see spectrum A in figure 5.4).
Another observation is that the interaction with Cu makes a peak appear at 826 cm^{-1} in the Raman spectrum of CuBTC MOF, assigned to mode 13 (in Wilson notation [100]) and OCO bending (scissoring) of carboxylate bound to Cu.
The vibrations at 460 and 502 cm^{-1} in the Raman spectrum of CuBTC MOF were assigned

to Cu-O stretch vibrations [101]. However, it is not straightforward to specify which Cu-O vibrations cause these peaks in the experimental Raman spectrum of CuBTC MOF, because Cu-O stretch vibrations show Raman peaks in a large spectral interval [101].
Some vibrations of BTC are not much influenced by its interaction with the environment. The benzene ring C-C stretch vibrations at 1002 and 1607 cm^{-1} in the Raman spectrum of BTC powder, vibration 12 and 8a,b in Wilson notation respectively [100], only show minor shifts when BTC interacts with water (1006 and 1616 cm^{-1}, respectively) or Cu (1004 and 1601 cm^{-1}, respectively [101]). Also the position of the CH stretch vibration at 3089 cm^{-1} in the Raman spectrum of BTC powder is not much influenced by changing the environment to water (3099 cm^{-1}).

Conclusion

Raman spectra of BTC powder, CuBTC MOF and BTC dissolved in water and corresponding gas-phase DFT calculated Raman spectra show that BTC interacts strongly with its environment. BTC interacts mainly by its carboxyl groups with other BTC molecules, Cu ions and water, resulting in large shifts of Raman peak positions assigned to carboxyl . The benzene ring vibrations of BTC show only minor shifts by changing the environment of BTC.

5.4. Binding geometry of BTC on CuUPD/Au

Introduction

To investigate the interaction between BTC and a Cu substrate, a well-defined Cu substrate was produced by electrochemical under potential deposition (UPD) of a monolayer of Cu onto a Au(111) substrate [94]. Earlier studies reporting on the adsorption of BTC monolayers on CuUPD/Au(111) show that BTC coordination-binds to a Cu substrate by two deprotonated carboxyl groups in air [92, 93, 94]. The benzene ring of BTC stands upright and is tilted 50 degrees away from the orientation perpendicular to the surface [94]. Furthermore, x-ray photoelectron spectroscopy under ultrahigh vacuum (UHV) revealed that carboxylates bind to a CuUPD/Au(111) substrate in a bidentate fashion, i.e. both oxygens of carboxylate bind to Cu [102, 93, 94]. Scanning tunneling microscopy in air revealed that BTC adsorbs on CuUPD/Au(111) in a row-structure to match the crystal lattice of the Cu crystal facet underneath [94]. The distances between BTC molecules in these row-structures are too large for hydrogen bonding between carboxyl groups of adjacent BTC molecules [94]. When Cu_2O is present at the Cu surface, n-alkanoic acids bind to the Cu substrate as a unidentate ligand, i.e. with only one of the oxygens their carboxylate bound to Cu [103]. The conclusions of the latter report are based on reflection-absorption IR spectra.
Surface enhanced Raman (SER) spectra of BTC on polycrystalline Cu under water showed that the conformation of the benzene ring of BTC was upright to the surface [104]. However, the latter report did not conclude on the exact adsorption geometry of BTC on polycrystalline Cu.
The mentioned reports that conclude on the adsorption geometry of BTC on CuUPD/Au(111) are performed in air or under ultrahigh vacuum (UHV). However, the

synthesis of CuBTC MOF takes place in solution. Therefore in this chapter the influence of a liquid environment on the adsorption of BTC on a Cu substrate was studied *in situ*. Does water have an influence on the binding geometry of BTC on Cu?

Quality of the CuUPD/Au substrates

Cyclic voltammetry (CV) and STM imaging were applied to check the quality of the Au substrates and amount of Cu deposited to define the CuUPD substrates. The left diagram in figure 5.5 shows CVs of the two different Au substrates which were used for all further experimental data shown in this chapter. The CVs were taken in the CuUPD electrolyte referenced to the Cu/Cu^{2+} Nernst potential in the solution. The black graph is a CV of annealed Au/mica and the blue graph is a CV of a roughened Au electrode. The CV of Au/mica shows two sharp reduction peaks at 0.241 and 0.033 V and two sharp oxidation peaks at 0.087 and 0.248 mV. The CV of the roughened Au substrate shows a broad reduction peak at 0.181 V and broad oxidation peak at 0.205, which are at different potentials compared with the CV of Au/mica. The CV of the roughened Au substrate also shows a vague shoulder in the reducing sweep at 0.035 V, and a small and broad oxidation peak at 0.061 V. The sharp peaks in the CV of Au/mica correspond to the two-stepped processes of deposition and stripping of Cu on top of Au(111) in a CuSO$_4$ electrolyte [105]. The broad reduction and oxidation peaks and the small reduction shoulder in the CV of the roughened Au electrode resembles the CV of CuUPD on polycrystalline Au in a CuSO$_4$ electrolyte [106]. Broadening of the peaks of the CV of CuUPD on polycrystalline Au is due to the disordered nature of the Cu layer [106].
The deposition of a monolayer of Cu on the Au substrates was performed in two steps. First a potential sweep from 0.3 to 0.01 V was performed (not shown here) and after that the substrate was kept for 65 seconds at 0.01 V (see the right diagram of figure 5.5). The measured current during the deposition steps corresponds to the number of deposited Cu atoms on the Au substrate. A full monolayer of Cu on Au(111) needs 440 C/cm^2 of charge transferred [107]. The Au(111)/mica substrate was covered with 0.4 monolayer (ML) of Cu during the linear voltage sweep. After that the deposition at 0.01 V Cu added Cu to a total of 0.9 ML, which is very close to the expected full monolayer. The roughened polycrystalline Au substrate was covered with 0.4 ML Cu during the linear voltage sweep. The deposition at 0.01 V added Cu up to a total of 3.1 ML, which is larger than the expected 1 ML of Cu/Au. Exceeding the 1 ML of Cu/Au at the roughened polycrystalline Au is not surprising, as the roughening increased the surface area of the electrode. The surface area of the roughened Au electrode is several times larger than the geometric surface area of 7.1 mm^2 based on the diameter of the Au disk. As the maximum coverage of Cu at the Au surface after under potential deposition is 1 ML, the roughening procedure made the surface area of the polycrystalline electrode at least 3.1 times larger. We can not conclude on the coverage of Cu at the polycrystalline Au substrate.
After CuUPD, the CuUPD/Au substrates were left in 1 mM BTC in water for 10 minutes. Afterwards the substrates were thoroughly cleaned in a stream of absolute ethanol for 60 seconds, dried with argon and clamped in the TERS or SERS cell. Before TER spectra were recorded from the BTC/CuUPD/Au(111) substrate a STM image was recorded (see figure 5.6). The image shows terraces with a height of 0.3 nm, which is close to the height

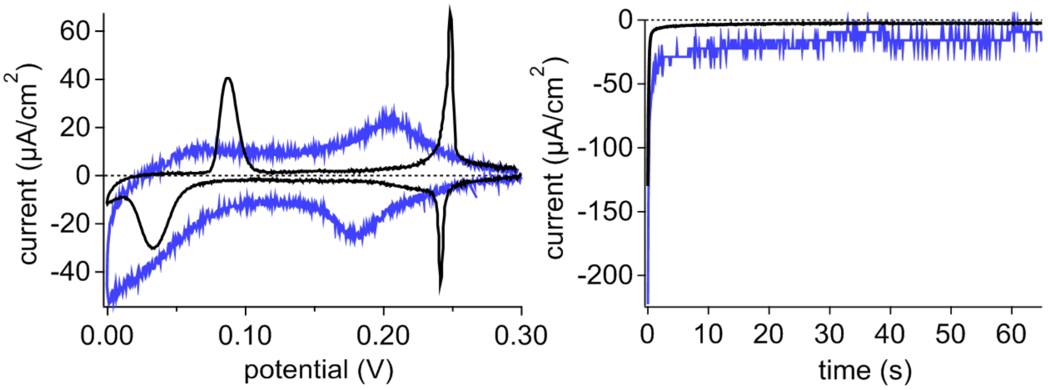

Figure 5.5.: Left: Cyclic voltammograms of Au/mica substrate (black) and roughened Au substrate (blue) in aqueous electrolyte of 50 mM H_2SO_4/10 mM $CuSO_4$. Potential is referenced to the Cu/Cu^{2+} Nernst potential in the solution. Scan speed is 5 mV/s. Right: Current during Cu under potential deposition on top of Au/mica substrate (black) and roughened Au substrate (blue). Current in both diagrams is normalized to the surface area of the electrode.

of Au(111) monoatomic steps of 0.235 nm [108].

TERS of BTC/CuUPD/Au

Introduction

TER spectra of BTC/CuUPD/Au were collected to investigate the adsorption state of BTC on CuUPD/Au(111). TERS can provide information on surface adsorption of molecules in several ways. If a molecule chemisorbs to a substrate, TERS can directly probe the bond between molecule and substrate [109]. However, the Raman peak of this bond might have a low intensity or might overlap with other bands, which complicates its interpretation. Furthermore, TERS is sensitive to the orientation of molecules in the tip-sample gap [81, 110]. The enhanced EM field between tip and sample in TERS is pointed along the axis of the tip, as explained in section 2.3.2. Therefore TERS is only sensitive to molecular vibrations that have components of the polarizability tensor changing in the direction parallel to the surface normal. Polarizability tensors of surface-adsorbed molecules, e.g. calculated by DFT, can be used to link changes in Raman peak ratios or (dis)appearance of Raman peaks in a TER spectrum to reorientations of the molecules in respect to the surface normal. In this section, the influence of the environment (air or water) on the adsorption state of BTC on CuUPD/Au is investigated. To this end, TER spectra were collected while the substrates were immersed in air or water. TERS peaks are assigned to molecular vibrations with the help of literature and gas-phase DFT calculations.

Data processing of TER spectra

Figure 5.7 shows TER spectra of a BTC/CuUPD/Au(111) measured in air (lower green

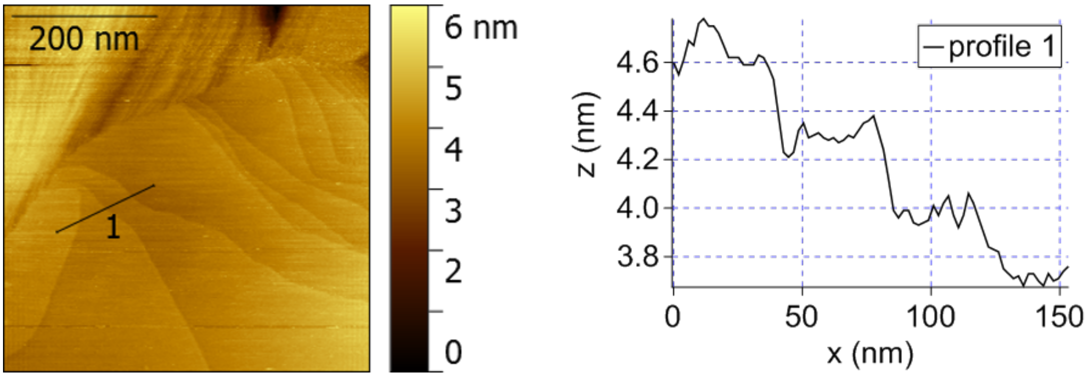

Figure 5.6.: Left: STM image of BTC/CuUPD/Au(111) substrate before TERS spectra were collected. STM details: PtIr mechanically cut tip, setpoint 10 pA, bias 500 mV, image 500 x 500 nm. Right: Height of profile 1 in the STM image on the left.

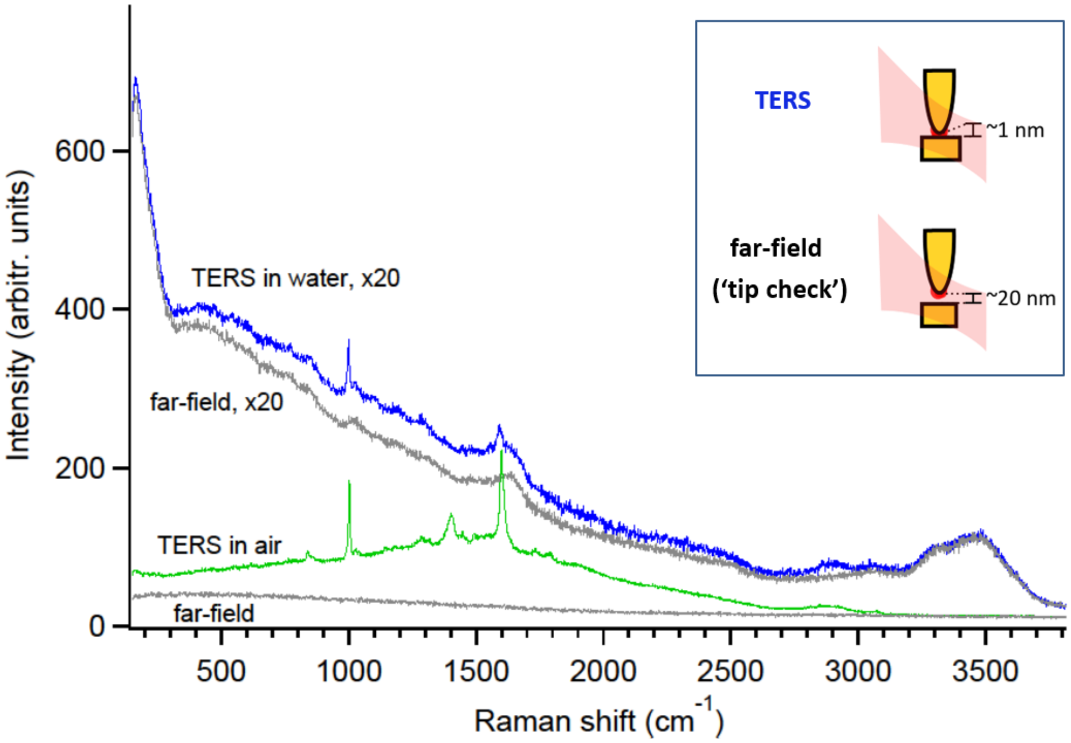

Figure 5.7.: Tip-enhanced Raman spectra of BTC/CuUPD/Au(111) in air (green spectrum; STM settings 0.05 nA and 0.1 V) and in water (blue spectrum; STM settings 0.2 nA and 0.1 V). Grey spectra are corresponding far-field Raman spectra with the tip 20 nm retracted from the substrate. All spectra are normalized to 0.13 mW power and 10 s acquisition time (water spectra X20).

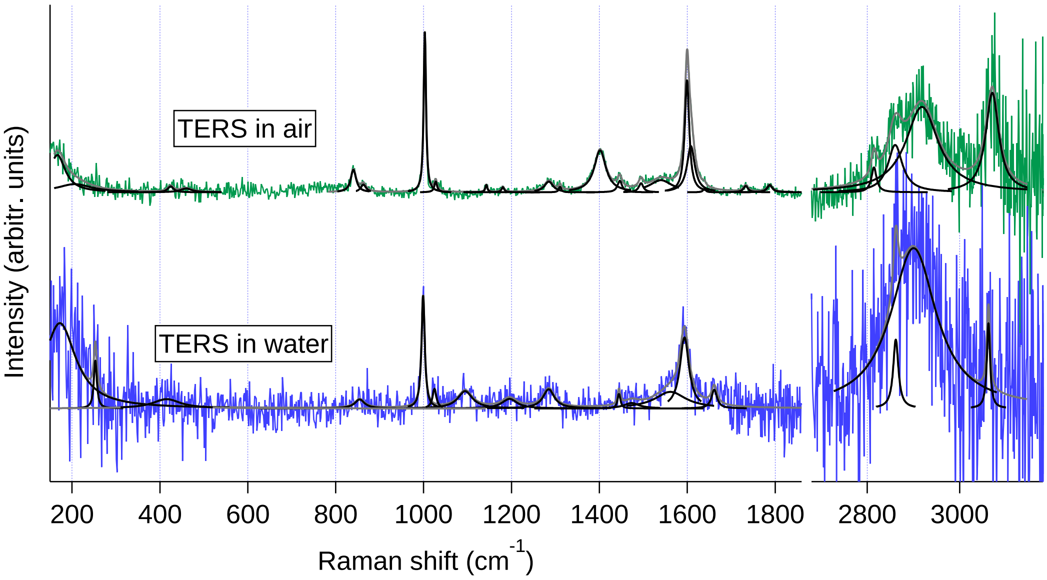

Figure 5.8.: TER spectra of BTC/CuUPD/Au(111) in air (top spectrum in green) and in water (bottom spectrum in blue) of figure 5.7 after background subtraction and scaling, as described in appendix B. Peak fits using Lorentzian lineshapes are shown in black. Spectra are normalized to the peak area of the peak at ca. 1000 cm^{-1} and y-offset for clarity. Center peak positions and band assignments are listed in figure 5.9. A full table of the fitting outcome can be found in appendix figure C.2.

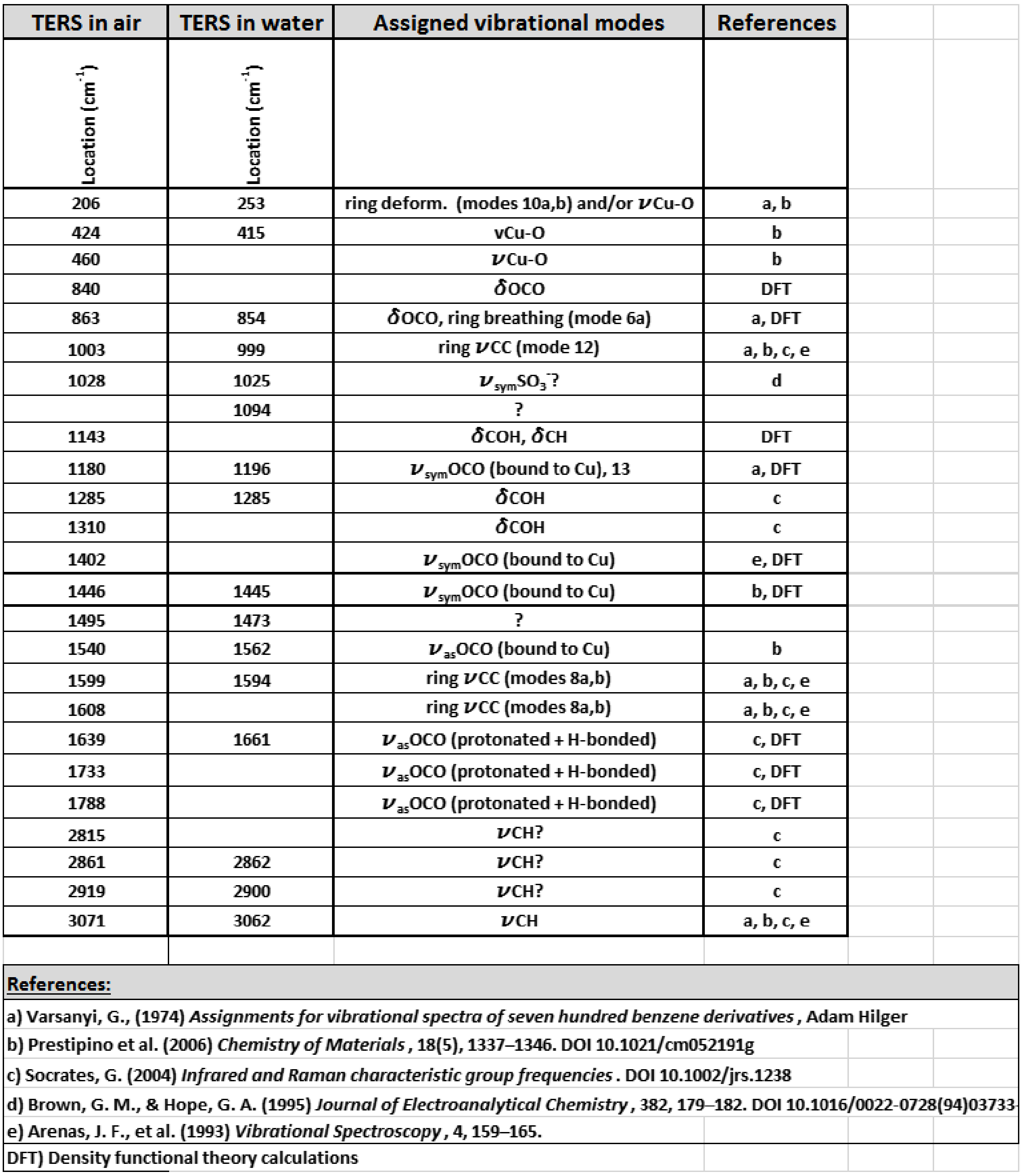

TERS in air	TERS in water	Assigned vibrational modes	References
Location (cm^{-1})	Location (cm^{-1})		
206	253	ring deform. (modes 10a,b) and/or νCu-O	a, b
424	415	vCu-O	b
460		νCu-O	b
840		δOCO	DFT
863	854	δOCO, ring breathing (mode 6a)	a, DFT
1003	999	ring νCC (mode 12)	a, b, c, e
1028	1025	$\nu_{sym}SO_3^-$?	d
	1094	?	
1143		δCOH, δCH	DFT
1180	1196	ν_{sym}OCO (bound to Cu), 13	a, DFT
1285	1285	δCOH	c
1310		δCOH	c
1402		ν_{sym}OCO (bound to Cu)	e, DFT
1446	1445	ν_{sym}OCO (bound to Cu)	b, DFT
1495	1473	?	
1540	1562	ν_{as}OCO (bound to Cu)	b
1599	1594	ring νCC (modes 8a,b)	a, b, c, e
1608		ring νCC (modes 8a,b)	a, b, c, e
1639	1661	ν_{as}OCO (protonated + H-bonded)	c, DFT
1733		ν_{as}OCO (protonated + H-bonded)	c, DFT
1788		ν_{as}OCO (protonated + H-bonded)	c, DFT
2815		νCH?	c
2861	2862	νCH?	c
2919	2900	νCH?	c
3071	3062	νCH	a, b, c, e

References:

a) Varsanyi, G., (1974) *Assignments for vibrational spectra of seven hundred benzene derivatives*, Adam Hilger
b) Prestipino et al. (2006) *Chemistry of Materials*, 18(5), 1337–1346. DOI 10.1021/cm052191g
c) Socrates, G. (2004) *Infrared and Raman characteristic group frequencies*. DOI 10.1002/jrs.1238
d) Brown, G. M., & Hope, G. A. (1995) *Journal of Electroanalytical Chemistry*, 382, 179–182. DOI 10.1016/0022-0728(94)03733-
e) Arenas, J. F., et al. (1993) *Vibrational Spectroscopy*, 4, 159–165.
DFT) Density functional theory calculations

Figure 5.9.: Peak positions of fitted peaks of TERS spectra of figure 5.8

spectrum) and measured while the substrate was immersed in water (top blue spectrum). Grey spectra are corresponding far-field Raman spectra acquired when the TERS tip is retracted from the substrate by 20 nm. From the spectra, it is clear that both the TERS spectrum in water and the far-field Raman spectrum in water show Raman bands of water (bending mode at ~1630 cm^{-1} and O-H stretch vibrations between 2950 and 3700 cm^{-1}). Furthermore, both the TER spectrum and far-field Raman spectrum in water show a large peak in the low wavenumber region (under 300 cm^{-1}). In literature reported Raman spectra of liquid water show one or more bands in the low frequency region (below 250 cm^{-1}), which find various interpretations. For example, Walrafen et al. [111] assign a vibration at 175 cm^{-1} to stretching of a hydrogen bond. On the contrary, Tominaga et al. [112] assign a band at 190 cm^{-1} to a stretching vibration of oxygen in the temporal tetrahedron of five water molecules, and a band at 70 cm^{-1} to a bending vibration of the whole water molecule. In the TER and far-field Raman spectrum in water in figure 5.7 the peak below 300 cm^{-1} is partly cut by the cut-off of the used edge filter at 156 cm^{-1}. However, even without a proper peak fit of the Raman peak below 300 cm^{-1}, we assign this peak vibrations of water, based on literature [111, 112].

The observed peaks assigned to water vibrations in the TER spectrum of BTC/CuUPD/Au(111) in water (i.e. the peaks between 2950 and 3700 cm^{-1}, at ~1630 cm^{-1} and below 300 cm^{-1}) overlap with Raman peaks of BTC vibrations. This complicates peak fitting of the peaks assigned to BTC vibrations. To get rid of the far-field water vibration contributions in the TER spectrum, the far-field Raman spectrum was withdrawn from the TER spectrum. The same procedure was followed for the TERS in air data treatment. After this first background subtraction step, a scaling step was performed to enable using peak ratio comparisons [58] (see section 2.3.2). The detailed scaling procedure of the TER spectra of figure 5.7 is discussed in appendix B. The scaled TER spectra are shown in figure 5.8 using the same color coding as the original TER spectra in figure 5.7: the top green spectrum is the scaled TER spectrum of a BTC/CuUPD/Au(111) substrate measured in air, and the bottom blue spectrum is the scaled TER spectrum of a BTC/CuUPD/Au(111) substrate measured in air. Peak positions from the fits and peak assignments are listed in figure 5.9.

Interpretation of TER spectra

Similar to the Raman spectra of BTC molecules in different environments shown in figure 5.3, the TER spectra of BTC/CuUPD/Au(111) in figure 5.8 also show a clear peak around 1000 cm^{-1} and a clear (combined) peak around 1600 cm^{-1}, respectively. These peaks are assigned to C=C stretch vibrations of the benzene ring of BTC (mode 12 and 8a,b in Wilson notation, respectively [100]) [101, 109].

Another peak that appears in both TER spectra in figure 5.8 is the peak at 3071 cm^{-1} in the TERS in air spectrum and 3062 cm^{-1} in the TERS in water spectrum. This peak is assigned to aromatic C-H stretch vibrations in the plane of the benzene ring [113, 109]. The polarizability derivatives of aromatic C-H stretch vibrational modes are non-zero in the plane of the benzene ring, while the ones out of the benzene ring plane are negligible [114]. Therefore, in a TER spectrum, an upright benzene ring would have a more intense aromatic CH stretch peak compared with the aromatic CH stretch peak of flat-lying benzene ring [114]. In both TER spectra in figure 5.8 a clear peak is assigned to aromatic CH stretch vibrations. This observation suggests that the benzene ring sits upright on the substrate when BTC is adsorbed to CuUPD/Au in air and in water.

In the TER in air spectrum in figure 5.8 two peaks appear at 424 and 460 cm^{-1}, while in the TER in water spectrum a peak appears at 415 cm^{-1}. These peaks are assigned to Cu-O stretch vibrations, based on the similar vibrational energy of the CuO stretch vibrations in CuBTC MOF [101]. These bands are a direct indication that carboxylate(s) of BTC chemisorb to Cu. However, the signal-to-noise ratio of these peaks is low. SERS spectra of BTC/CuUPD/Au in air and water (see figure A.1) show Raman bands around 420 and 460 cm^{-1}. SERS generally shows a higher Raman enhancement compared to TERS, because more hot-spots reside in the beam focus (see theory section 2.2.2).

The largest difference between the TER spectra of BTC/CuUPD/Au before and after adding water (see figure 5.8), is the disappearance of the peak at 1402 cm^{-1} with the presence of water. Based on literature [104, 115, 109] and gas-phase DFT calculations the peak at 1402 cm^1 is assigned to a ν_{sym}C-O_2 vibration of carboxylate bound to Cu. Furthermore, both TER spectra in figure 5.8 show a peak around 1445 cm^{-1}, which is also assigned to ν_{sym}C-O_2 vibration of carboxylate bound to Cu based on literature [101], the far-field Raman spectrum of CuBTC (spectrum C in figure 5.3) and gas-phase DFT calculations. Changes in ratio between ~1400 and ~1440 cm^{-1} peak of adsorbed BTC an Ag, Cu or Au, upon changing the surface potential of the metal have been observed before [104]. However, no interpretation of the reported observations was provided [104]. Gas-phase DFT calculations show that the ratio between the peaks around 1400 and 1440 cm^{-1} differ depending on the number of carboxylates of BTC binding to Cu. When BTC is bound to Cu with three carboxylates, gas-phase DFT calculations show only a ν_{sym}C-O_2 vibration at 1441 cm^{-1} (see table 5.1). When BTC binds to Cu with two carboxylates, a new peak of a ν_{sym}C-O_2 vibration appears at 1409 cm^{-1} (see table 5.1) However, care has to be taken with the calculated values for Raman activities by DFT, such as the values shown in table 5.1. The Raman activity calculated by DFT is not proportional to the Raman cross section of experimental Raman spectra. To compare the Raman activity with experimental Raman cross sections a local field correction depending on the refractive index of the medium is required [32] (see more details in appendix chapter D). Furthermore, the Raman activity values in table 5.1 do not take the directional sensitivity of TERS into account.

In both TER spectra in figure 5.8 two broad and overlapping peaks are observed at 2861 and 2919 cm^{-1} and at 2862 and 2900 cm^{-1}, respectively. The spectral region between ~2800 to 3000 cm^{-1} is characteristic for aliphatic C-H stretch vibrations [36]. However, no molecules with aliphatic chains were added to the investigated system. Therefore, the source of these peaks remains unclear.

Conclusion and outlook

Analysis of TER spectra of BTC adsorbed to CuUPD/Au suggest that BTC binds to CuUPD/Au by chemisorption of its carboxylates. Adding water to BTC chemisorbed to a Cu monolayer on Au induces changes in its TERS spectrum. One of the vibrations assigned to carboxylate binding to Cu disappears after immersing BTC/CuUPD/Au in water. This suggests a change in binding geometry of BTC to CuUPD/Au (e.g. the number of carboxylates binding to the Cu/Au substrate).

These results show that the investigation of molecular processes at solid-liquid interfaces should also be studied under such conditions, i.e. the liquid phase can not be excluded. The current status of this investigation lays the base for the *in situ* investigation of layer-by-layer epitaxial, solvothermal or electrochemical growth of CuBTC MOFs at metallic surfaces. The nanometric resolution of TERS can in such studies be used to investigate the growth process of MOF on top of a metal substrate or on top of a monolayer of organic linkers.

6. Outlook

This thesis discusses the development of a home-designed solid-liquid TER spectrometer. The solid-liquid TER spectrometer can probe the vibrational fingerprint of molecules at solid-liquid interfaces. As a first demonstration of the application of the home-build solid-liquid TER spectrometer, the binding geometry of benzene-1,3,5-tricarboxylic acid to a monolayer of Cu on a Au substrate under water was investigated. This dissertation provides an overview of solutions for technical difficulties in the design of solid-liquid TER spectrometers. However, solid-liquid TERS is still in its very early stage of development. Further developments of solid-liquid TERS and theoretical calculations of investigated systems can broaden the applicability of this tool.

Many solid-liquid interfacial processes depend on surface potential. To investigate the influence of surface potential on those processes on the nanoscale, TERS should be measured while varying the surface potential. Solid-liquid electrochemical TERS can technically be realized by the implementation of a bipotentiostat in the TER spectrometer [110]. This enables a three electrode setup where the potential of the solid surface can be controlled against a reference electrode potential.

This thesis discusses TERS results measured in a Au-Au gap mode, which generally shows a larger enhancement than TERS on other substrates than Au or other coineous metals. To enable TERS measurements on other substrates than coineous metals, the sensitivity of TERS should be increased. There are several methods to increase the sensitivity of TERS. A spatial light modulator (SLM) can be implemented in the beam path of the TER spectrometer to optimize the focusing efficiency of light to the tip. For the optimization procedure, the pixels of the SLM can be turned on or off, and the TERS intensity can be implemented as a feedback whether the pixel-combination is beneficial for the final TERS signal. This method will also help to counteract for the optical aberrations induced by the introduction of the solid-liquid TERS-cell and liquid itself into the beam path. A higher TERS enhancement could be met when the LSP resonance of the nanostructured tip apex exactly matches the incident laser wavelength. A way to accomplish this, is refining the etching procedure of TERS tips. Another way is tuning the wavelenght of the laser to match with the nanostructure of the tip. Furthermore, technical improvements could lead to a higher sensitivity of TERS, e.g. the implementation of an electron-multiplying CCD camera or using a higher NA objective.

Several improvements could be made to broaden *in situ* solid-liquid TERS measurements. Higher TERS sensitivity could be used to decrease the measurement time. This would enable measuring dynamic processes involving molecules at solid-liquid interfaces. A TERS flow-cell would enable TERS investigations of chemical reactions at solid-liquid interfaces. This would for example be useful to study the *in situ* layer-by-layer growth of metal organic frameworks (MOFs).

Implementing a sample stage in the TER spectrometer enables acquiring TERS maps larger than 1×1 µm. However, in solid-liquid TERS moving the sample means also moving the sample cell including all interfaces of different refractive index. The latter might induce focus distortions of light to the tip. Possibly a spatial light modulator can be used to refocus the incident light to the tip during movements of the sample cell.

Enabling solid-liquid TERS outside of water or aqueous electrolytes broadens the applicability of solid-liquid TERS. To accomplish freedom of choice of the liquid phase in solid-liquid TERS, the tip coating and glue for the sample cell window might have to be adapted to ensure chemical resistivity towards the liquid phase.

In this dissertation, density functional theory (DFT) calculations in gas-phase were used to analyze TER spectra. Gas-phase DFT calculations do not show a good fit with experimental TERS data, because the interaction of molecules with the solid surface is not implemented. Therefore, to simulate TER spectra, the substrate has to be implemented in theoretical calculations.

Appendices

A. SERS spectra of BTC/CuUPD/Au

SERS spectra of BTC/CuUPD/Au (see figure A.1) were acquired to support the interpretation of TER spectra in chapter 5.

SERS substrates were prepared by electrochemical roughening of polycrystalline Au electrodes (GAMEC Analysentechnik) in 0.1 M KCl. After roughening, the electrode was cleaned with ultrapure water and stored in ultrapure water until further use. CuUPD and BTC adsorption on SERS substrates were performed with the same procedures as used for the preparation of annealed Au/mica substrates (see section 5.2).

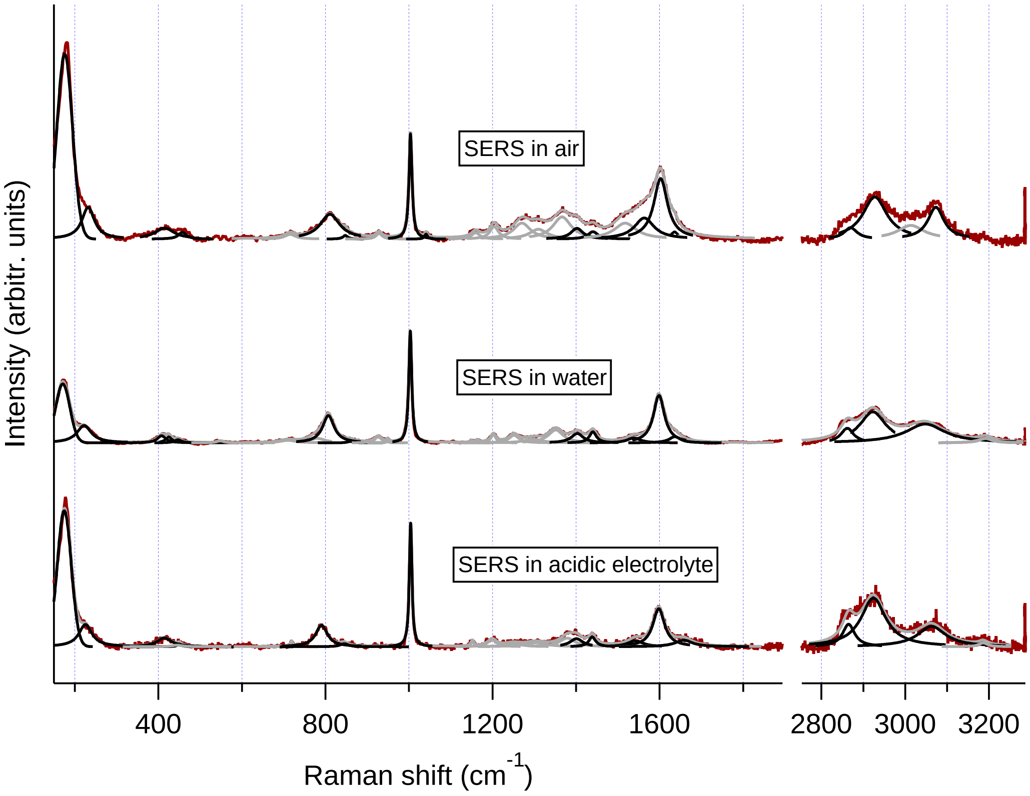

Figure A.1.: Surface-enhanced Raman spectrum of BTC/CuUPD/Au in air, in water and in aqueous 10 mM H_2SO_4. Spectra are background subtracted and scaled by their background as described by Lin et al.[58], of which an example in shown in appendix figure B.3. Spectra are normalized to the peak area of the peak at ca. 1000 cm^{-1} and y-offset for clarity. Laser power and measurement times are 0.13 mW, 3 s, respectively. Peaks are fitted with Lorentzian lineshapes. Appendix figure C.2 contains the fitting outcome and peak assignment of the spectra of this figure.

B. Background subtraction and scaling of SER and TER spectra of chapter 5

For TER spectra in chapter 5 the background subtraction and scaling procedure described by Lin et al. [58]is applied. This scaling method is shown for TER and SER spectra presented in chapter 5. In figure B.3 the scaling method is applied on a SERS in aqueous electrolyte measurement. The black spectrum in figure B.3 is raw data. The red trace is a polynomial fit of the continuum background of the raw SERS spectum (black spectrum). For the scaling procedure, first the red fit is retracted from the black spectrum (background subtraction) and after that, the resulting spectrum is divided by the red spectrum (scaling). The resulting scaled spectrum is shown in blue in figure B.3. The same procedure was applied for a TER spectrum in air (see figure B.1), and a TER spectrum in water (see figure B.2).

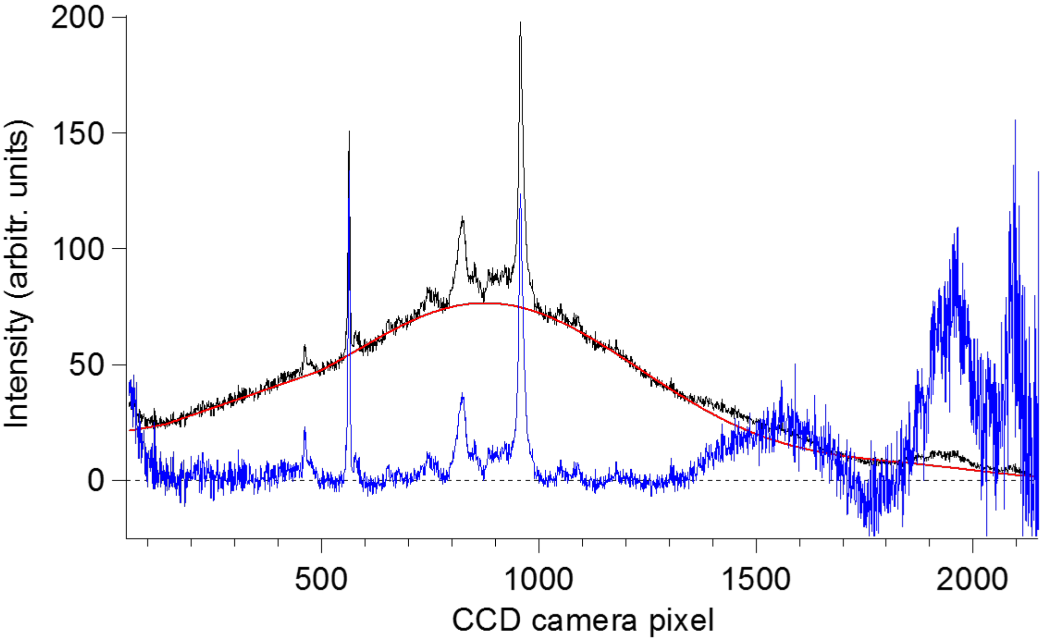

Figure B.1.: Step 2 in background subtraction and scaling procedure of a TER spectrum measured in air: scaling of the TER spectrum by its background. Black spectrum is a TER spectrum of BTC/CuUPD/Au(111) in air after subtraction of a TER spectrum with the tip 20 nm retracted (see figure 5.7 for raw data). Red trace is a polynomial fit of the background of the TER spectrum. Blue spectrum is obtained by retracting and dividing the raw TER spectrum (black spectrum) by the background fit (red trace).

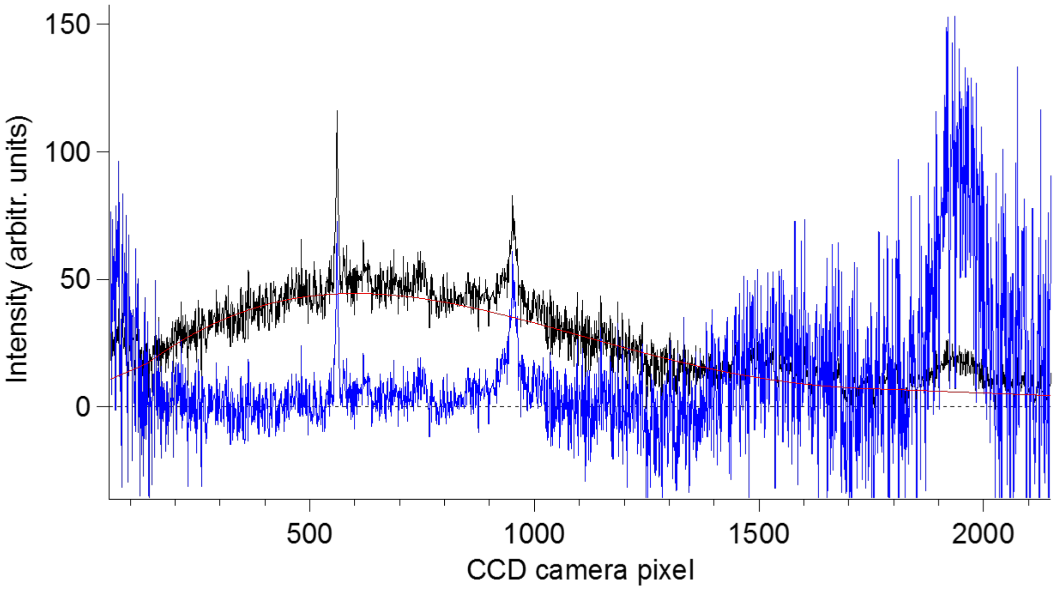

Figure B.2.: Step 2 in background subtraction and scaling procedure of a TER spectrum measured in water: scaling of the TER spectrum by its background. Black spectrum is a TER spectrum of BTC/CuUPD/Au(111) in water after subtraction of a TER spectrum with the tip 20 nm retracted (see figure 5.7 for raw data). Red trace is a polynomial fit of the background of the TER spectrum. Blue spectrum is obtained by retracting and dividing the raw TER spectrum (black spectrum) by the background fit (red trace).

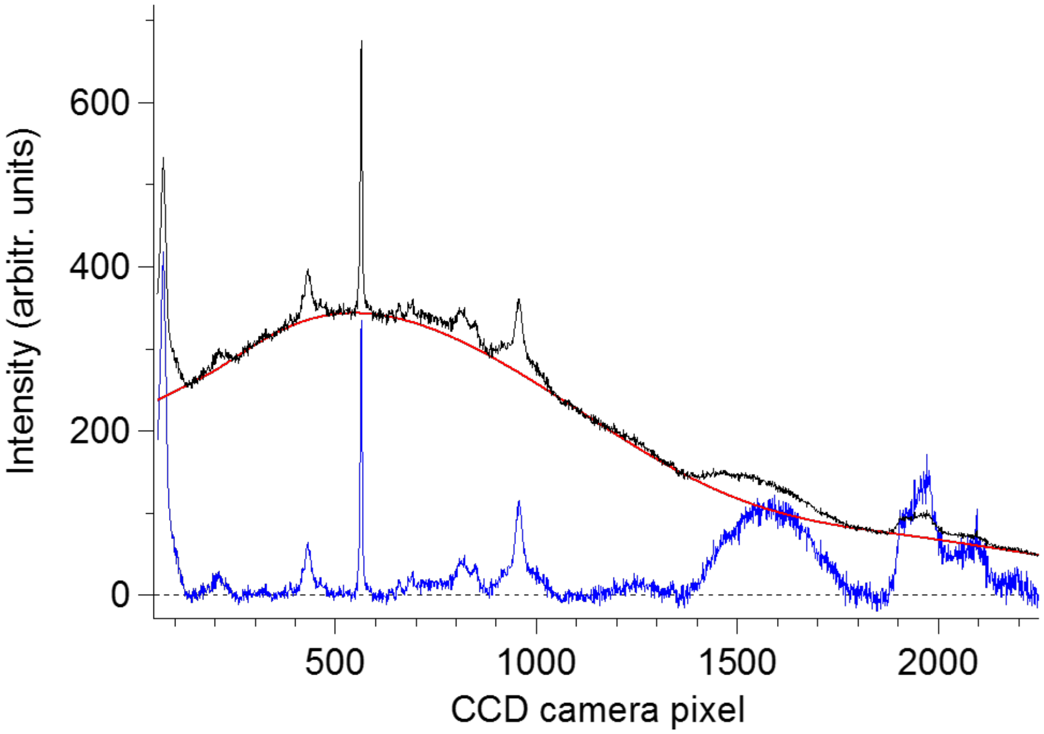

Figure B.3.: Example background subtraction and scaling procedure of a SER spectrum in aqueous electrolyte. Black spectrum is a raw SER spectrum of BTC/CuUPD/Au in 10 mM H_2SO_4 in water. Red trace is a polynomial fit of the background of the SER spectrum. Blue spectrum is obtained by retracting and dividing the raw SER spectrum (black spectrum) by the background fit (red trace).

C. Peak fitting and peak assignment of spectra of chapter 5

In table C.1fitting parameters and peak assignments of the Raman spectra of figures 5.3 are shown. In table C.2 fitting parameters and peak assignments of TER spectra of figure 5.8 and SER spectra of figure A.1, respectively, are shown.

Table C.1.: Fitting parameters and peak assignments of spectra of figure 1 of the main manuscript. Peaks were fitted with Lorentzian functions to extract peak positions, peak area and full width at half maximum (FWHM). Fitting errors are also given. Furthermore, for every spectrum the peak area is shown as percentage of the total peak area. Peak assignments are given in Wilson notation [100].

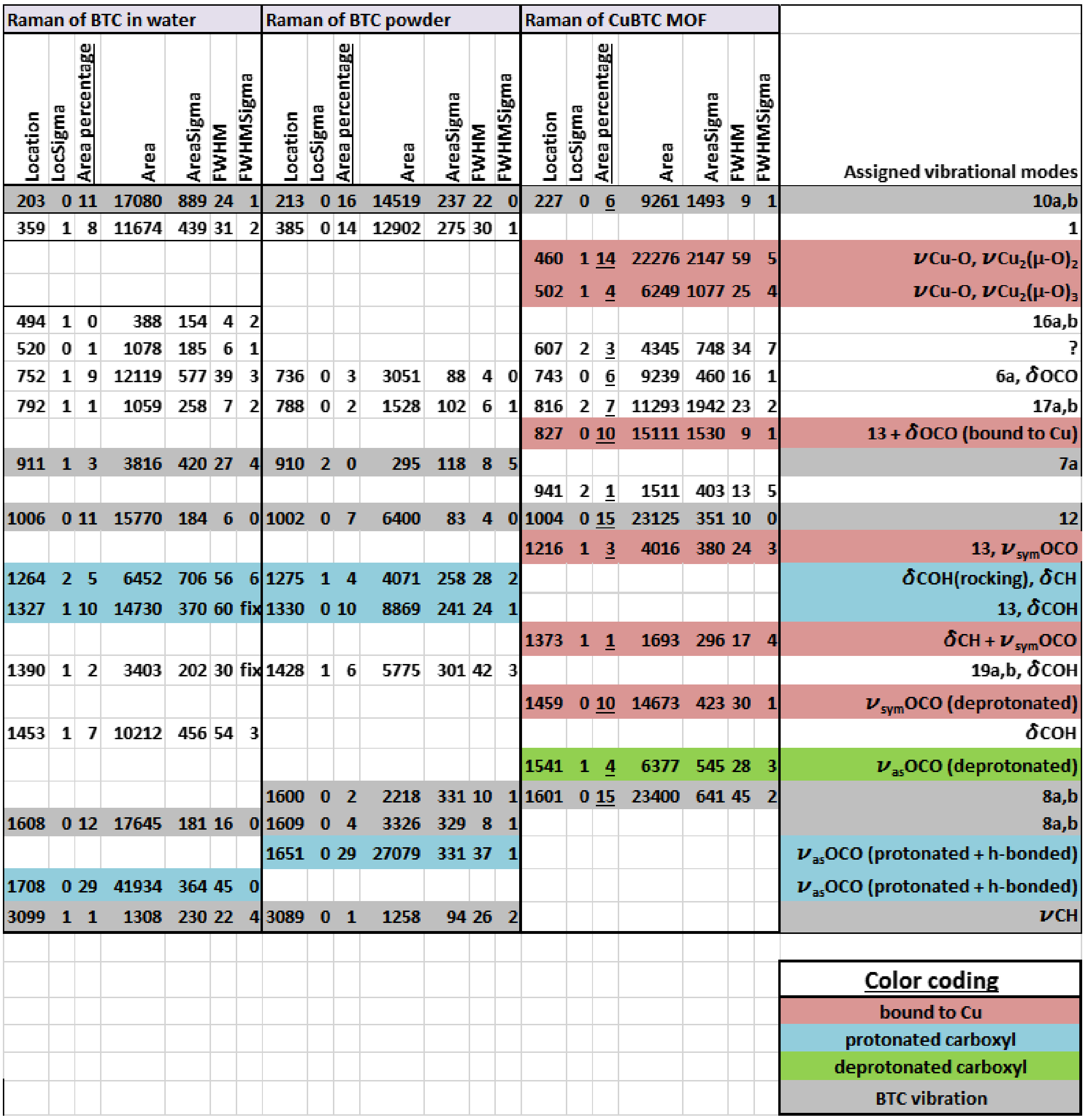

Raman of BTC in water							Raman of BTC powder							Raman of CuBTC MOF							
Location	LocSigma	Area percentage	Area	AreaSigma	FWHM	FWHMSigma	Location	LocSigma	Area percentage	Area	AreaSigma	FWHM	FWHMSigma	Location	LocSigma	Area percentage	Area	AreaSigma	FWHM	FWHMSigma	Assigned vibrational modes
203	0	11	17080	889	24	1	213	0	16	14519	237	22	0	227	0	6	9261	1493	9	1	10a,b
359	1	8	11674	439	31	2	385	0	14	12902	275	30	1								1
														460	1	14	22276	2147	59	5	νCu-O, $\nu Cu_2(\mu\text{-}O)_2$
														502	1	4	6249	1077	25	4	νCu-O, $\nu Cu_2(\mu\text{-}O)_3$
494	1	0	388	154	4	2															16a,b
520	0	1	1078	185	6	1								607	2	3	4345	748	34	7	?
752	1	9	12119	577	39	3	736	0	3	3051	88	4	0	743	0	6	9239	460	16	1	6a, δOCO
792	1	1	1059	258	7	2	788	0	2	1528	102	6	1	816	2	7	11293	1942	23	2	17a,b
														827	0	10	15111	1530	9	1	13 + δOCO (bound to Cu)
911	1	3	3816	420	27	4	910	2	0	295	118	8	5								7a
														941	2	1	1511	403	13	5	
1006	0	11	15770	184	6	0	1002	0	7	6400	83	4	0	1004	0	15	23125	351	10	0	12
														1216	1	3	4016	380	24	3	13, ν_{sym}OCO
1264	2	5	6452	706	56	6	1275	1	4	4071	258	28	2								δCOH(rocking), δCH
1327	1	10	14730	370	60	fix	1330	0	10	8869	241	24	1								13, δCOH
														1373	1	1	1693	296	17	4	δCH + ν_{sym}OCO
1390	1	2	3403	202	30	fix	1428	1	6	5775	301	42	3								19a,b, δCOH
														1459	0	10	14673	423	30	1	ν_{sym}OCO (deprotonated)
1453	1	7	10212	456	54	3															δCOH
														1541	1	4	6377	545	28	3	ν_{as}OCO (deprotonated)
							1600	0	2	2218	331	10	1	1601	0	15	23400	641	45	2	8a,b
1608	0	12	17645	181	16	0	1609	0	4	3326	329	8	1								8a,b
							1651	0	29	27079	331	37	1								ν_{as}OCO (protonated + h-bonded)
1708	0	29	41934	364	45	0															ν_{as}OCO (protonated + h-bonded)
3099	1	1	1308	230	22	4	3089	0	1	1258	94	26	2								νCH

Color coding
bound to Cu
protonated carboxyl
deprotonated carboxyl
BTC vibration

Table C.2.: Fitting parameters and peak assignments of TER spectra of figure 5.8 and SER spectra of figure A.1. Peaks were fitted with Lorentzian functions to extract peak positions, peak area and full width at half maximum (FWHM). Fitting errors are also given. Furthermore, for every spectrum the peak area is shown as percentage of the total peak area. Peak assignments are given in Wilson notation [100].

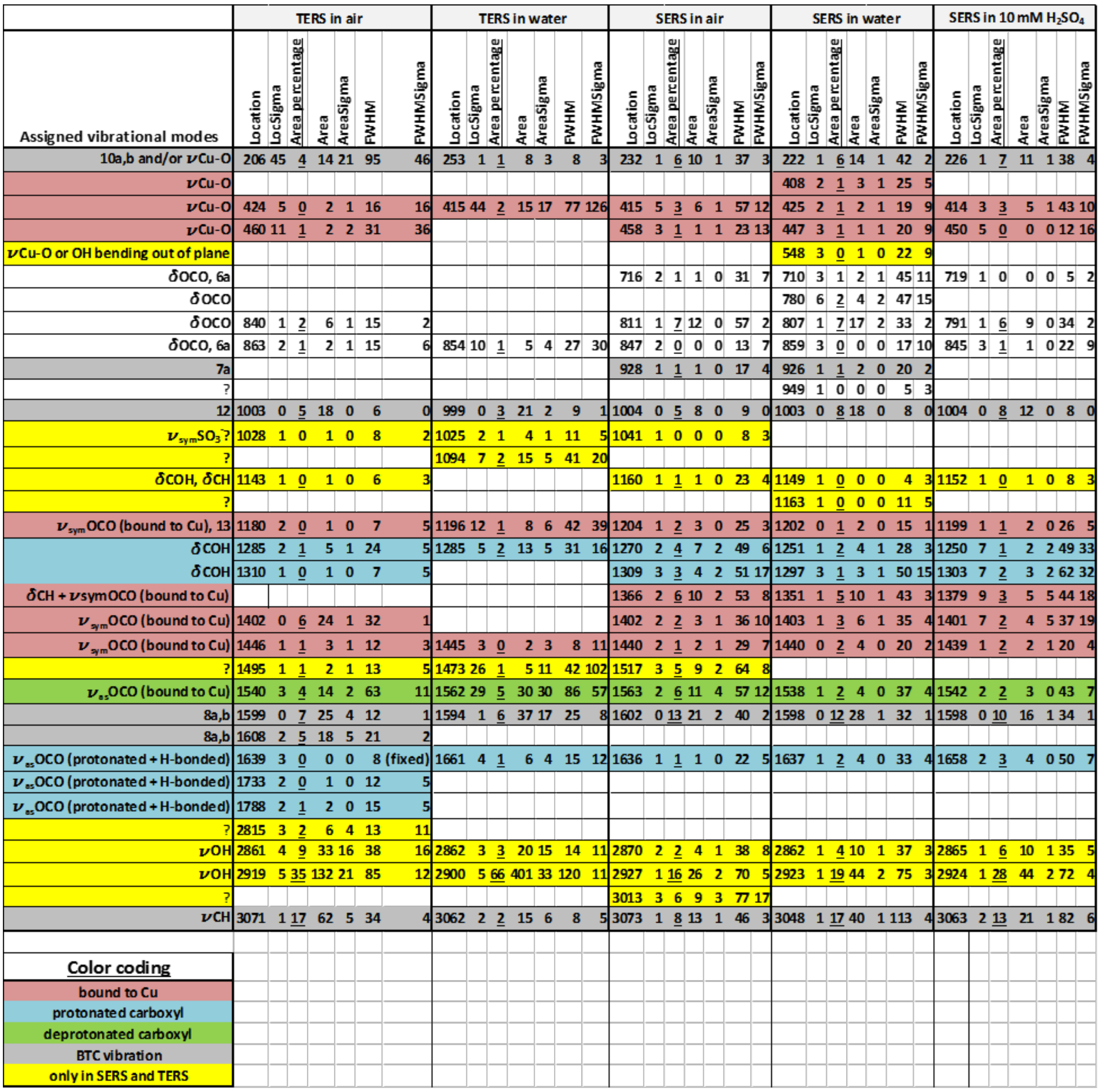

	TERS in air							TERS in water							SERS in air							SERS in water							SERS in 10 mM H_2SO_4						
Assigned vibrational modes	Location	LocSigma	Area percentage	Area	AreaSigma	FWHM	FWHMSigma	Location	LocSigma	Area percentage	Area	AreaSigma	FWHM	FWHMSigma	Location	LocSigma	Area percentage	Area	AreaSigma	FWHM	FWHMSigma	Location	LocSigma	Area percentage	Area	AreaSigma	FWHM	FWHMSigma	Location	LocSigma	Area percentage	Area	AreaSigma	FWHM	FWHMSigma
10a,b and/or νCu-O	206	45	4	14	21	95	46	253	1	1	8	3	8	3	232	1	6	10	1	37	3	222	1	6	14	1	42	2	226	1	7	11	1	38	4
νCu-O																						408	2	1	3	1	25	5							
νCu-O	424	5	0	2	1	16	16	415	44	2	15	17	77	126	415	5	3	6	1	57	12	425	2	1	2	1	19	9	414	3	3	5	1	43	10
νCu-O	460	11	1	2	2	31	36								458	3	1	1	1	23	13	447	3	1	1	1	20	9	450	5	0	0	0	12	16
νCu-O or OH bending out of plane																						548	3	0	1	0	22	9							
δOCO, 6a															716	2	1	1	0	31	7	710	3	1	2	1	45	11	719	1	0	0	0	5	2
δOCO																						780	6	2	4	2	47	15							
δOCO	840	1	2	6	1	15	2								811	1	7	12	0	57	2	807	1	7	17	2	33	2	791	1	6	9	0	34	2
δOCO, 6a	863	2	1	2	1	15	6	854	10	1	5	4	27	30	847	2	0	0	0	13	7	859	3	0	0	0	17	10	845	3	1	1	0	22	9
7a															928	1	1	1	0	17	4	926	1	1	2	0	20	2							
?																						949	1	0	0	0	5	3							
12	1003	0	5	18	0	6	0	999	0	3	21	2	9	1	1004	0	5	8	0	9	0	1003	0	8	18	0	8	0	1004	0	8	12	0	8	0
$\nu_{sym}SO_3^-$?	1028	1	0	1	0	8	2	1025	2	1	4	1	11	5	1041	1	0	0	0	8	3														
?								1094	7	2	15	5	41	20																					
δCOH, δCH	1143	1	0	1	0	6	3								1160	1	1	1	0	23	4	1149	1	0	0	0	4	3	1152	1	0	1	0	8	3
?																						1163	1	0	0	0	11	5							
ν_{sym}OCO (bound to Cu), 13	1180	2	0	1	0	7	5	1196	12	1	8	6	42	39	1204	1	2	3	0	25	3	1202	0	1	2	0	15	1	1199	1	1	2	0	26	5
δCOH	1285	2	1	5	1	24	5	1285	5	2	13	5	31	16	1270	2	4	7	2	49	6	1251	1	2	4	1	28	3	1250	7	1	2	2	49	33
δCOH	1310	1	0	1	0	7	5								1309	3	3	4	2	51	17	1297	3	1	3	1	50	15	1303	7	2	3	2	62	32
δCH + νsymOCO (bound to Cu)															1366	2	6	10	2	53	8	1351	1	5	10	1	43	3	1379	9	3	5	5	44	18
ν_{sym}OCO (bound to Cu)	1402	0	6	24	1	32	1								1402	2	2	3	1	36	10	1403	1	3	6	1	35	4	1401	7	2	4	5	37	19
ν_{sym}OCO (bound to Cu)	1446	1	1	3	1	12	3	1445	3	0	2	3	8	11	1440	2	1	2	1	29	7	1440	0	2	4	0	20	2	1439	1	2	2	1	20	4
?	1495	1	1	2	1	13	5	1473	26	1	5	11	42	102	1517	3	5	9	2	64	8														
ν_{as}OCO (bound to Cu)	1540	3	4	14	2	63	11	1562	29	5	30	30	86	57	1563	2	6	11	4	57	12	1538	1	2	4	0	37	4	1542	2	2	3	0	43	7
8a,b	1599	0	7	25	4	12	1	1594	1	6	37	17	25	8	1602	0	13	21	2	40	2	1598	0	12	28	1	32	1	1598	0	10	16	1	34	1
8a,b	1608	2	5	18	5	21	2																												
ν_{as}OCO (protonated + H-bonded)	1639	3	0	0	0	8	(fixed)	1661	4	1	6	4	15	12	1636	1	1	1	0	22	5	1637	1	2	4	0	33	4	1658	2	3	4	0	50	7
ν_{as}OCO (protonated + H-bonded)	1733	2	0	1	0	12	5																												
ν_{as}OCO (protonated + H-bonded)	1788	2	1	2	0	15	5																												
?	2815	3	2	6	4	13	11																												
νOH	2861	4	9	33	16	38	16	2862	3	3	20	15	14	11	2870	2	2	4	1	38	8	2862	1	4	10	1	37	3	2865	1	6	10	1	35	5
νOH	2919	5	35	132	21	85	12	2900	5	66	401	33	120	11	2927	1	16	26	2	70	5	2923	1	19	44	2	75	3	2924	1	28	44	2	72	4
?															3013	3	6	9	3	77	17														
νCH	3071	1	17	62	5	34	4	3062	2	2	15	6	8	5	3073	1	8	13	1	46	3	3048	1	17	40	1	113	4	3063	2	13	21	1	82	6

Color coding
bound to Cu
protonated carboxyl
deprotonated carboxyl
BTC vibration
only in SERS and TERS

D. Gas phase density functional theory calculations

D.1. Introduction

Density functional theory (DFT) calculations can be used to predict Raman and IR vibrational spectra. The aim of DFT is to calculate the electronic structure of a molecule. The DFT calculation of a Raman spectrum of a molecule is performed in two steps. The first step is called *geometry optimization*, in which the electronic 'ground state' of a molecule is obtained by finding the lowest energy state of atomic positions. In the second step the molecular vibrations and corresponding Raman activities and IR intensities are calculated. In the second step the force constants (interactions among atoms) are calculated by displacing each atom at a time. Then the linear optical polarizability tensor is calculated by recalculating the electronic structure of the optimized geometry of the first step in presence of an external EM field. From there on, the polarizability changes with respect to atomic displacements are calculated leading to the output of Raman activity per molecular vibration.

DFT was shown to very well predict the vibrations of molecules in gas phase [32]. However, one of the drawbacks of DFT is that **this method usually overestimates the frequencies of vibrations of a molecule**. If the DFT calculation is used for peak assignment of an experimental Raman spectrum, the DFT calculated vibrations can be scaled based on the experimental Raman spectrum. Usually this correction scaling is less than ∼10 percent. Furthermore, Raman scattering and IR absorption selection rules are applied in DFT, so DFT can predict well which vibrations are silent in Raman scattering and IR absorption spectroscopy. However, care has to be taken with the units of the 'Raman activity' in the output of DFT calculations. **The 'Raman activity' of Raman active modes that DFT calculates should not be directly compared with Raman cross sections of this vibration in experimental Raman spectra** [32]. The Raman activity calculated by DFT is not proportional to the Raman cross section of experimental Raman spectra. To compare the Raman activity with experimental Raman cross sections a local field correction depending on the refractive index of the medium is required [32].

D.2. Scaling factors for gas phase DFT calculations

Scaling factors for gas phase DFT calculated spectra presented in chapter 5 have been derived with the help of conventional Raman spectra. Two different scaling factors were derived for the gas-phase DFT calculations presented in chapter 5. For scaling of the gas-phase DFT calculated spectrum of a BTC tetramer, the peak positions of a Raman spectrum of BTC powder were used (see figure D.1). For scaling of all gas-phase DFT

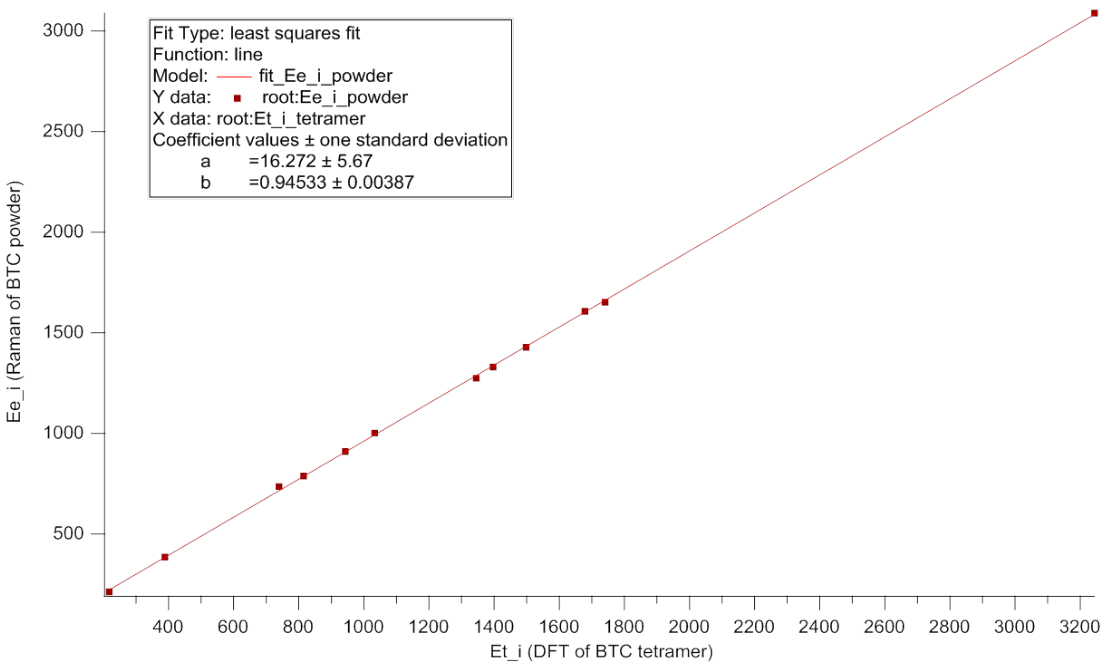

Figure D.1.: Procedure used to find the scaling factor for gas-phase DFT calculation of BTC tetramer. On the X-axis are central peak positions of a Raman spectrum of a BTC tetramer calculated by gas phase DFT. On the Y-axis are corresponding central peak positions of a Raman spectrum of BTC powder. Fitting a straight line using least squares method leads to the scaling factor 0.945 for the gas-phase DFT calculated spectrum of a BTC tetramer.

calculated spectra of BTC monomers (of which some are bound to Cu and/or hydrogen-bonded to water), the peak positions of a Raman spectrum of BTC dissolved in water were used (see figure D.2).

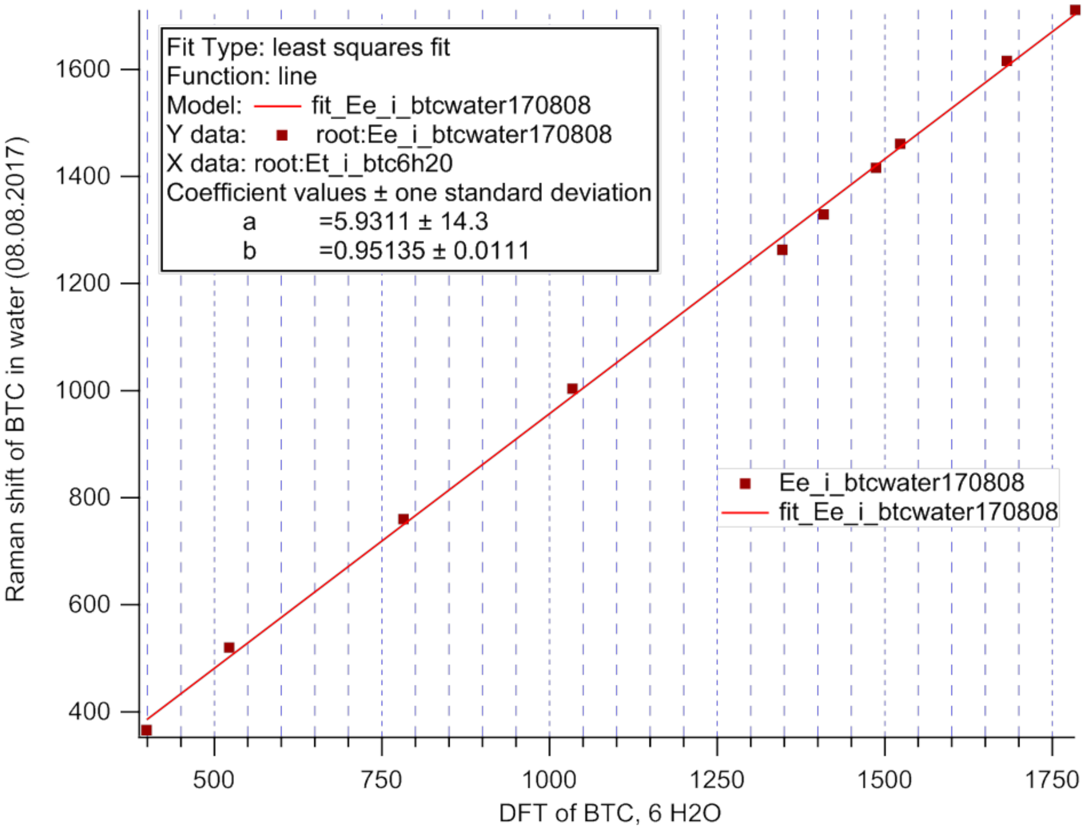

Figure D.2.: Procedure used to find the scaling factor for gas-phase DFT calculation of BTC monomers. On the X-axis are central peak positions of a Raman spectrum of a BTC monomer hydrogen-bonded to 6 water molecules, calculated by gas phase DFT. On the Y-axis are corresponding central peak positions of a Raman spectrum of BTC dissolved in water. Fitting a straight line using least squares method leads to the scaling factor 0.951 for the gas-phase DFT calculated spectra of BTC monomers.

Bibliography

[1] Yuyan Shao, Jun Wang, Hong Wu, Jun Liu, Ilhan A. Aksay, and Yuehe Lin. Graphene based electrochemical sensors and biosensors: A review. *Electroanalysis*, 22(10):1027–1036, 2010.

[2] Jiri Homola, Sinclair S. Yee, and Günter Gauglitz. Surface plasmon resonance sensors review.pdf. *Sensors and Actuators, B: Chemical*, 54:3–15, 1999.

[3] Indrani Banerjee, Ravindra C. Pangule, and Ravi S. Kane. Antifouling coatings: Recent developments in the design of surfaces that prevent fouling by proteins, bacteria, and marine organisms. *Advanced Materials*, 23(6):690–718, 2011.

[4] Akira Fujishima and Kenichi Honda. Electrochemical Photolysis of Water at a Semiconductor Electrode. *Nature*, 238:37–38, 1972.

[5] Federico Calle-Vallejo, Marc T.M. Koper, and Aliaksandr S. Bandarenka. Tailoring the catalytic activity of electrodes with monolayer amounts of foreign metals. *Chemical Society Reviews*, 42(12):5210–5230, 2013.

[6] Chun Li, Hua Bai, and Gaoquan Shi. Conducting polymer nanomaterials: Electrosynthesis and applications. *Chemical Society Reviews*, 38(8):2397–2409, 2009.

[7] Simon G. Patching. Surface plasmon resonance spectroscopy for characterisation of membrane protein-ligand interactions and its potential for drug discovery. *Biochimica et Biophysica Acta - Biomembranes*, 1838(1 PARTA):43–55, 2014.

[8] Bo Liedberg, Claes Nylander, and Ingemar Lundstrom. Surface plasmon resonance for gas detection and biosensing. *Sensors and Actuators*, 4:299–304, 1983.

[9] Noémie Elgrishi, Kelley J. Rountree, Brian D. McCarthy, Eric S. Rountree, Thomas T. Eisenhart, and Jillian L. Dempsey. A Practical Beginner's Guide to Cyclic Voltammetry. *Journal of Chemical Education*, 95(2):197–206, 2018.

[10] Stefan Bergner, Preety Vatsyayan, and Frank Michael Matysik. Recent advances in high resolution scanning electrochemical microscopy of living cells - A review. *Analytica Chimica Acta*, 775:1–13, 2013.

[11] Stefan W. Hell and Jan Wichmann. Breaking the diffraction resolution limit by stimulated emission: stimulated-emission-depletion fluorescence microscopy. *Opt. Lett.*, 19(US20080160042A1):780–782, 1994.

[12] E Betzig, G H Patterson, R Sougrat, O W Lindwasser, S Olenych, J S Bonifacino, M W Davidson, J Lippincott-Schwartz, and H F Hess. Imaging Intracellular Fluorescent Proteins at Nanometer Resolution. *Science*, 313(5793):1642–1645, 2006.

[13] Michael J. Rust, Mark Bates, and Xiaowei Zhuang. Sub-diffraction-limit imaging by stochastic optical reconstruction microscopy (STORM). *Nature Methods*, 3(10):793–795, 2006.

[14] K. Wandelt and S. Thurgate. Solid-liquid interfaces, macroscopic phenomena - microscopic understanding, 2003.

[15] Steven De Feyter and Frans C. De Schryver. Self-assembly at the liquid/solid interface: STM reveals. *Journal of Physical Chemistry B*, 109(10):4290–4302, 2005.

[16] Julie V. Macpherson and Patrick R. Unwin. Combined scanning electrochemical-atomic force microscopy. *Analytical Chemistry*, 72(2):276–285, 2000.

[17] Sarah M. Rehn and Matthew R. Jones. New Strategies for Probing Energy Systems with in Situ Liquid-Phase Transmission Electron Microscopy. *ACS Energy Letters*, 3(6):1269–1278, 2018.

[18] Cheng Hao Wu, Robert S. Weatherup, and Miquel B. Salmeron. Probing electrode/electrolyte interfaces in situ by X-ray spectroscopies: Old methods, new tricks. *Physical Chemistry Chemical Physics*, 17(45):30229–30239, 2015.

[19] G. Binnig and C. F. Quate. Atomic Force Microscope. *Physical Review Letters*, 56(9):930–933, 1986.

[20] G. Binnig, H. Rohrer, C. Gerber, and E. Weibel. Surface Studies by Scanning Tunneling Microscopy. *Physical Review Letters*, 49(I):57–61, 1993.

[21] A S Dakkouri, M Dietterle, and D M Kolb. The study of solid-liquid interfaces by in-situ STM. *Festkörperprobleme*, 36:1–31, 1996.

[22] Toshio Ando, Takayuki Uchihashi, and Takeshi Fukuma. High-speed atomic force microscopy for nano-visualization of dynamic biomolecular processes. *Progress in Surface Science*, 83(7-9):337–437, 2008.

[23] M. J. Williamson, R. M. Tromp, P. M. Vereecken, R. Hull, and F. M. Ross. Dynamic microscopy of nanoscale cluster growth at the solid-liquid interface. *Nature Materials*, 2(8):532–536, 2003.

[24] Joseph I. Goldstein, Dale E. Newbury, Patrick Echlin, David C. Joy, A. D. RomigJr., Charles E. Lyman, Charles Fiori, and Eric Lifshin. *Scanning Electron Microcopy and X-Ray Microanalysis.* 1992.

[25] R.F. Egerton. *Electron Energy-Loss Spectrocopy in the Electron Microscope*, volume 3. 2011.

[26] Hai Tao Rong, Stefan Frey, Yong Jie Yang, Michael Zharnikov, Manfred Buck, Mario Wühn, Christof Wöll, and Günter Helmchen. On the importance of the headgroup substrate bond in thiol monolayers: A study of biphenyl-based thiols on gold and silver. *Langmuir*, 17(5):1582–1593, 2001.

[27] Li-Jun Wan, Mimi Terashima, Hiroyuki Noda, and Masatoshi Osawa. Molecular Orientation and Ordered Structure of Benzenethiol Adsorbed on Gold(111). *The Journal of Physical Chemistry B*, 104(15):3563–3569, 2000.

[28] Dan Lis, Ellen H.G. Backus, Johannes Hunger, Sapun H. Parekh, and Mischa Bonn. Liquid flow along a solid surface reversibly alters interfacial chemistry. *Science*, 344(6188):1138–1142, 2014.

[29] Zhong-Qun Tian and Bin Ren. Adsorption and Reaction At Electrochemical Interfaces As Probed By Surface-Enhanced Raman Spectroscopy. *Annual Review of Physical Chemistry*, 55(1):197–229, 2004.

[30] Thomas Schmid, Boon Siang Yeo, Grace Leong, Johannes Stadler, and Renato Zenobi. Performing tip-enhanced Raman spectroscopy in liquids. *Journal of Raman Spectroscopy*, 2009.

[31] Derek A. Long. *The Raman Effect.* Wiley, 1 edition, 2002.

[32] Eric C. Le Ru and Pablo G. Etchegoin. *Principles of Surface-Enhanced Raman Spectroscopy.* Elsevier, 1 edition, 2009.

[33] Peter Atkins and Julio de Paula. *Atkins physical chemistry.* Oxford, 7 edition, 2002.

[34] Satyaprakash Sahoo, R. Palai, and R. S. Katiyar. Polarized Raman scattering in monolayer, bilayer, and suspended bilayer graphene. *Journal of Applied Physics*, 110(4), 2011.

[35] Ewen Smith and Geoffrey Dent. *Modern Raman Spectroscopy*, volume 1. 2005.

[36] George Socrates. *Infrared and Raman Characteristic Group Frequencies.* Wiley, 3 edition, 2004.

[37] M. Fleischmann, P. J. Hendra, and A. J. McQuillan. Raman spectra of pyridine adsorbed at a silver electrode. *Chemical Physics Letters*, 26(2):163–166, 1974.

[38] David L. Jeanmaire and Richard P. Van Duyne. Surface raman spectroelectrochemistry: Part I. Heterocyclic, aromatic, and aliphatic amines adsorbed on the anodized silver electrode. *Journal of Electroanalytical Chemistry*, 84(1):1–20, 1977.

[39] M. Moskovits. Surface roughness and the enhanced intensity of Raman scattering by molecules adsorbed on metals. *The Journal of Chemical Physics*, 69(9):4159–4161, 1978.

[40] Satoshi Kawata, Yasushi Inouye, and Prabhat Verma. Plasmonics for near-field nano-imaging and superlensing. *Nature Photonics*, 3(7):388–394, 2009.

[41] K. Lance Kelly, Eduardo Coronado, Lin Lin Zhao, and George C. Schatz. The optical properties of metal nanoparticles: The influence of size, shape, and dielectric environment. *Journal of Physical Chemistry B*, 2003.

[42] Song-Yuan Ding, Jun Yi, Jian-Feng Li, Bin Ren, De-Yin Wu, Rajapandiyan Panneerselvam, and Zhong-Qun Tian. Nanostructure-based plasmon-enhanced Raman spectroscopy for surface analysis of materials. *Nature Reviews Materials*, 1(6):16021, 2016.

[43] Tanja Deckert-Gaudig, Atsushi Taguchi, Satoshi Kawata, and Volker Deckert. Tip-enhanced Raman spectroscopy from early developments to recent advances. *Chem. Soc. Rev.*, 2017.

[44] Samuel L. Kleinman, Renee R. Frontiera, Anne Isabelle Henry, Jon A. Dieringer, and Richard P. Van Duyne. Creating, characterizing, and controlling chemistry with SERS hot spots. *Physical Chemistry Chemical Physics*, 15(1):21–36, 2013.

[45] Ying Fang, Nak-Hyun Seong, and Dana D. Dlott. Measurement of the Distribution of Site Enhancements in Surface-Enhanced Raman Scattering. *Science*, (December):388–393, 2008.

[46] John Wessel. Surface-enhanced optical microscopy. *J. Opt. Soc. Am. B*, 2:1538–1541, 1985.

[47] Mark S. Anderson. Locally enhanced Raman spectroscopy with an atomic force microscope. *Applied Physics Letters*, 76(21):3130–3132, 2000.

[48] Norihiko Hayazawa, Yasushi Inouye, Zouheir Sekkat, and Satoshi Kawata. Metallized tip amplification of near-field Raman scattering. *Optics Communications*, 183(1):333–336, 2000.

[49] Raoul M. Stöckle, Yung Doug Suh, Volker Deckert, and Renato Zenobi. Nanoscale chemical analysis by tip-enhanced Raman spectroscopy. *Chemical Physics Letters*, 318(1-3):131–136, 2000.

[50] Bruno Pettinger, Gennaro Picardi, Rolf Schuster, and Gerhard Ertl. Surface enhanced Raman Spectroscopy: Towards Single Molecule Spectroscopy. *Electrochemistry*, 68(12):942–949, 2000.

[51] Feng Shao and Renato Zenobi. Tip-enhanced Raman spectroscopy: principles, practice, and applications to nanospectroscopic imaging of 2D materials. *Analytical and Bioanalytical Chemistry*, 2018.

[52] Chi Chen, Norihiko Hayazawa, and Satoshi Kawata. A 1.7 nm resolution chemical analysis of carbon nanotubes by tip-enhanced Raman imaging in the ambient. *Nature Communications*, 5:1–5, 2014.

[53] Xiu-Mei Lin, Tanja Deckert-Gaudig, Prabha Singh, Michael Siegmann, Stephan Kupfer, Zhenglong Zhang, Stefanie Gräfe, and Volker Deckert. Direct Base-to-Base Transitions in ssDNA Revealed by Tip-Enhanced Raman Scattering. pages 1–28, 2016.

[54] Bruno Pettinger, Katrin F. Domke, Dai Zhang, Gennaro Picardi, and Rolf Schuster. Tip-enhanced Raman scattering: Influence of the tip-surface geometry on optical resonance and enhancement. *Surface Science*, 603(10-12):1335–1341, 2009.

[55] Natalia Martin Sabanes, Amala Elizabeth, Jonas H. K. Pfisterer, and Katrin Domke. FDSERS17 The effect of STM parameters on tip-enhanced Raman spectra. *Faraday Discuss.*, 2017.

[56] Lukas Novotny and Bert Hecht. *Principles of Nano-Optics*. Elsevier, 1 edition, 2006.

[57] Jianhua Dai, Frantisek Ajko, Igor Tsukerman, and Mark I. Stockman. Electrodynamic effects in plasmonic nanolenses. *Physical Review B - Condensed Matter and Materials Physics*, 77(11):1–5, 2008.

[58] Kai-Qiang Lin, Jun Yi, Jin-Hui Zhong, Shu Hu, Bi-Ju Liu, Jun-Yang Liu, Cheng Zong, Zhi-Chao Lei, Xiang Wang, Javier Aizpurua, Rubén Esteban, and Bin Ren. Plasmonic photoluminescence for recovering native chemical information from surface-enhanced Raman scattering. *Nature Communications*, 8:14891, 2017.

[59] G. T. Boyd, Z. H. Yu, and Y. R. Shen. Photoinduced luminescence from the noble metals and its enhancement on roughened surfaces. *Physical Review B*, 33(12):7923–7936, 1986.

[60] Prabhat Verma. Tip-Enhanced Raman Spectroscopy: Technique and Recent Advances. *Chemical Reviews*, (117):6447–6466, 2017.

[61] Robert Meyer, Xiaobin Yao, and Volker Deckert. Latest instrumental developments and bioanalytical applications in tip-enhanced Raman spectroscopy. *TrAC - Trends in Analytical Chemistry*, 102:250–258, 2018.

[62] Dmitry Kurouski, Michael Mattei, and Richard P. Van Duyne. Probing Redox Reactions at the Nanoscale with Electrochemical Tip-Enhanced Raman Spectroscopy. *Nano Letters*, 15(12):7956–7962, 2015.

[63] Zhi-Cong Zeng, Sheng-Chao Huang, De-Yin Wu, Ling-Yan Meng, Mao-Hua Li, Teng-Xiang Huang, Jin-Hui Zhong, Xiang Wang, Zhi-Lin Yang, and Bin Ren. Electrochemical Tip-Enhanced Raman Spectroscopy. *Journal of the American Chemical Society*, 137(37):11928–11931, 2015.

[64] Natalia Martín Sabanés, Leonie M. A. Driessen, and Katrin F. Domke. Versatile Side-Illumination Geometry for Tip-Enhanced Raman Spectroscopy at Solid/Liquid Interfaces. *Analytical Chemistry*, 2016.

[65] Nastaran Kazemi-Zanjani, Sylvain Vedraine, and François Lagugné-Labarthet. Localized enhancement of electric field in tip-enhanced Raman spectroscopy using radially and linearly polarized light. *Optics Express*, 21(21):25271, 2013.

[66] Naresh Kumar, Weitao Su, Martin Veselý, Bert M. Weckhuysen, Andrew J. Pollard, and Andrew J. Wain. Nanoscale chemical imaging of solid–liquid interfaces using tip-enhanced Raman spectroscopy. *Nanoscale*, 2018.

[67] Thomas Touzalin, Suzanne Joiret, Emmanuel Maisonhaute, and Ivan T. Lucas. Complex Electron Transfer Pathway at a Microelectrode Captured by in Situ Nanospectroscopy. *Analytical Chemistry*, 89(17):8974–8980, 2017.

[68] Bergin Gjonaj, Patrick Johnson, Mischa Bonn, and Katrin F. Domke. Index mismatch aberration correction over long working distances using spatial light modulation. *Applied Optics*, 51(33):8034, 2012.

[69] Natalia Martín Sabanés. *Electrochemical Tip-Enhanced Raman Spectroscopy.* 2017.

[70] Ya Ping Huang, Sheng Chao Huang, Xiang Jie Wang, Nataraju Bodappa, Chao Yu Li, Hao Yin, Hai Sheng Su, Meng Meng, Hua Zhang, Bin Ren, Zhi Lin Yang, Renato Zenobi, Zhong Qun Tian, and Jian Feng Li. Shell-Isolated Tip-Enhanced Raman and Fluorescence Spectroscopy. *Angewandte Chemie - International Edition*, 57(25):7523–7527, 2018.

[71] Arnold Adams, J. C. Wyss, and P. K. Hansma. Possible observation of local plasmon modes excited by electrons tunneling through junctions. *Physical Review Letters*, 42(14):912–915, 1979.

[72] Bin Ren, Gennaro Picardi, and Bruno Pettinger. Preparation of gold tips suitable for tip-enhanced Raman spectroscopy and light emission by electrochemical etching. *Review of Scientific Instruments*, 75(4):837–841, 2004.

[73] Noriko N. Horimoto, Shigeru Tomizawa, Yasuhiko Fujita, Shinji Kajimoto, and Hiroshi Fukumura. Nano-scale characterization of binary self-assembled monolayers under an ambient condition with STM and TERS. *Chemical Communications*, 50(69):9862–9864, 2014.

[74] Wan Ing Lin, Feng Shao, Bruno Stephanidis, and Renato Zenobi. Tip-enhanced Raman spectroscopic imaging shows segregation within binary self-assembled thiol monolayers at ambient conditions. *Analytical and bioanalytical chemistry*, 407(27):8197–8204, 2015.

[75] J. Christopher Love, Lara A. Estroff, Jennah K. Kriebel, Ralph G. Nuzzo, and George M. Whitesides. Self-Assembled Monolayers of Thiolates on Methals as a Form of Nanotechnology. 105:1103–1169, 2005.

[76] Taka Aki Yano, Prabhat Verma, Yuika Saito, Taro Ichimura, and Satoshi Kawata. Pressure-assisted tip-enhanced Raman imaging at a resolution of a few nanometres. *Nature Photonics*, 3(8):473–477, 2009.

[77] Johanna E Bohn, Pablo G Etchegoin, Eric C Le Ru, Rong Xiang, Shohei Chiashi, and Shigeo Maruyama. Estimating the {Raman} {Cross} {Sections} of {Single} {Carbon} {Nanotubes}. *ACS Nano*, 4(6):3466–3470, 2010.

[78] Gennaro Picardi, Marc Chaigneau, and Razvigor Ossikovski. High resolution probing of multi wall carbon nanotubes by Tip Enhanced Raman Spectroscopy in gap-mode. *Chemical Physics Letters*, 469(1-3):161–165, 2009.

[79] Nikolaos Nianias. Patchy surfaces. *Thesis*, 2018.

[80] Danielle M. Fitzgerald, Emily K. Krisanda, Colleen G. Szypko, and L. Gaby Avila-Bront. Ambient STM study of sequentially adsorbed octanethiol and biphenylthiol monolayers on Au(111). *Surface Science*, 662(August 2016):102–112, 2017.

[81] Nan Jiang, Naihao Chiang, Lindsey R. Madison, Eric A. Pozzi, Michael R. Wasielewski, Tamar Seideman, Mark A. Ratner, Mark C. Hersam, George C. Schatz, and Richard P. Van Duyne. Nanoscale chemical imaging of a dynamic molecular phase boundary with ultrahigh vacuum tip-enhanced raman spectroscopy. *Nano Letters*, 16(6):3898–3904, 2016.

[82] Susumu Kitagawa and Ryotaro Matsuda. Chemistry of coordination space of porous coordination polymers, 2007.

[83] Christopher H. Hendon, Adam J. Rieth, Maciej D. Korzyński, and Mircea Dincă. Grand Challenges and Future Opportunities for Metal-Organic Frameworks. *ACS Central Science*, 2017.

[84] Stephen S Y Chui, Samuel M F Lo, Jonathan P H Charmant, a Guy Orpen, and Ian D Williams. A Chemically Functionalizable Nanoporous Material [Cu_3(TMA)_2(H_2O)_3]_n. *Science*, 283(February):1148–1150, 1999.

[85] Jin Liang Zhuang, Andreas Terfort, and Christof Wöll. Formation of oriented and patterned films of metal-organic frameworks by liquid phase epitaxy: A review. *Coordination Chemistry Reviews*, 307:391–424, 2015.

[86] Carmen Munuera, Osama Shekhah, Hui Wang, Christof Wöll, and Carmen Ocal. The controlled growth of oriented metal-organic frameworks on functionalized surfaces as followed by scanning force microscopy. *Physical chemistry chemical physics : PCCP*, 10:7257–7261, 2008.

[87] Enrica Biemmi, Camilla Scherb, and Thomas Bein. Oriented Growth of the Metal Organic Framework $Cu_3(BTC)_2(H_2O)_3{\cdot}x(H_2O)$ Tunable with Functionalized Self-Assembled Monolayers. *Journal of the American Chemical Society*, 129(26):8054–8055, 2007.

[88] Osama Shekhah, Hui Wang, Denise Zacher, Roland A. Fischer, and Christof Wöll. Growth mechanism of metal-organic frameworks: Insights into the nucleation by employing a step-by-step route. *Angewandte Chemie - International Edition*, 48(27):5038–5041, 2009.

[89] Alex Summerfield, Izabela Cebula, Martin Schröder, and Peter H. Beton. Nucleation and Early Stages of Layer-by-Layer Growth of Metal Organic Frameworks on Surfaces. *Journal of Physical Chemistry C*, 119(41):23544–23551, 2015.

[90] Guusje Delen, Zoran Ristanović, Laurens D.B. Mandemaker, and Bert M. Weckhuysen. Mechanistic Insights into Growth of Surface-Mounted Metal-Organic Framework Films Resolved by Infrared (Nano-) Spectroscopy. *Chemistry - A European Journal*, 24(1):187–195, 2018.

[91] Philipp Schäfer, Anusha Lalitha, Paula Sebastian, Santosh Kumar Meena, Juan Feliu, Marialore Sulpizi, Monique A. van der Veen, and Katrin F. Domke. Trimesic acid on Cu in ethanol: Potential-dependent transition from 2-D adsorbate to 3-D metal-organic framework. *Journal of Electroanalytical Chemistry*, pages 1–9, 2017.

[92] Izabela Cebula, Cai Shen, and Manfred Buck. Isophthalic acid: A basis for highly ordered monolayers. *Angewandte Chemie - International Edition*, 49(35):6220–6223, 2010.

[93] C Shen, I Cebula, C Brown, J L Zhao, M Zharnikov, and M Buck. Structure of isophthalic acid based monolayers and its relation to the initial stages of growth of metal-organic coordination layers. *Chemical Science*, 3(111):1858–1865, 2012.

[94] Izabela Cebula, Hao Lu, Michael Zharnikov, and Manfred Buck. Monolayers of trimesic and isophthalic acid on Cu and Ag: the influence of coordination strength on adsorption geometry. *Chemical Science*, 4(12):4455, 2013.

[95] D. J. Duchamp and R. E. Marsh. The crystal structure of trimesic acid (benzene-1,3,5-tricarboxylic acid). *Acta Crystallographica Section B Structural Crystallography and Crystal Chemistry*, 25(1):5–19, 1969.

[96] Alexander Apelblat, Emanuel Manzurola, and Nazmia Abo Balal. The solubilities of benzene polycarboxylic acids in water. *Journal of Chemical Thermodynamics*, 38(5):565–571, 2006.

[97] J.A. Dean. Lange's handbook of chemistry. *McGraw-Hill*, 13th edition, 1985.

[98] G. B. Deacon and R. J. Phillips. Relationships between the carbon-oxygen stretching frequencies of carboxylate complexes and the type of carboxylate coordination. *Coordination Chemistry Reviews*, 33:227–250, 1980.

[99] Michael J. Zaworotko. Superstructural diversity in two dimensions: crystal engineering of laminated solids. *Chemical Communications*, (1):1–9, 2001.

[100] E. Bright Wilson. The normal modes and frequencies of vibration of the regular plane hexagon model of the benzene molecule. *Physical Review*, 45(10):706–714, 1934.

[101] C. Prestipino, L. Regli, J. G. Vitillo, F. Bonino, A. Damin, C. Lamberti, A. Zecchina, P. L. Solari, K. O. Kongshaug, and S. Bordiga. Local structure of framework Cu(II) in HKUST-1 metallorganic framework: Spectroscopic characterization upon activation and interaction with adsorbates. *Chemistry of Materials*, 18(5):1337–1346, 2006.

[102] Shu-Yi Lin, Tung-Ku Tsai, Chia-Mei Lin, Chun-hsien Chen, Yang-Chiang Chan, and Hsiu-Wei Chen. Structures of Self-Assembled Monolayers of n -Alkanoic Acids on Gold Surfaces Modified by Underpotential Deposition of Silver and Copper: Odd-Even Effect. *Langmuir*, 18(14):5473–5478, 2002.

[103] Yu Tai Tao. Structural Comparison of Self-Assembled Monolayers of n-Alkanoic Acids on the Surfaces of Silver, Copper, and Aluminum. *Journal of the American Chemical Society*, 115(10):4350–4358, 1993.

[104] Youngmin Kim, Kyungnam Cho, Kangtaek Lee, Jaebum Choo, Myoung seon Gong, and Sang Woo Joo. Electric field-induced adsorption change of 1,3,5-benzenetricarboxylic acid on gold, silver, and copper electrode surfaces investigated

by surface-enhanced Raman scattering. *Journal of Molecular Structure*, 878(1-3):155–161, 2008.

[105] M. A. Schneeweiss and D. M. Kolb. The Initial Stages of Copper Deposition on Bare and Chemically Modified Gold Electrodes. *Physica Status Solidi (a)*, 173:51–71, 1999.

[106] Kai D. Etzel, Katrin R. Bickel, and Rolf Schuster. Heat effects upon electrochemical copper deposition on polycrystalline gold. *ChemPhysChem*, 11(7):1416–1424, 2010.

[107] Enrique Herrero, Lisa J. Buller, and Héctor D. Abruña. Underpotential deposition at single crystal surfaces of Au, Pt, Ag and other materials. *Chemical Reviews*, 101(7):1897–1930, 2001.

[108] Hidetoshi Honbo, Shizuo Sugawara, and Kingo Itaya. Detailed in-situ scanning tunneling microscopy of single crystal planes of gold (111) in aqueous solutions. *Analytical chemistry*, 62(34):2424–2429, 1990.

[109] J F Arenas, M A Montaiiez, J C Otero, and J I Marcos. Surface enhanced raman spectra of benzene tricarboxylate anions on silver sols. *Vibrational Spectroscopy*, 4:159–165, 1993.

[110] Natalia Martín Sabanés, Tatsuhiko Ohto, Denis Andrienko, Yuki Nagata, and Katrin F. Domke. Electrochemical TERS Elucidates Potential-Induced Molecular Reorientation of Adenine/Au(111). *Angewandte Chemie - International Edition*, 56(33):9796–9801, 2017.

[111] G. E. Walrafen. Raman spectral studies of water structure. *The Journal of Chemical Physics*, 40(11):3249–3256, 1964.

[112] Yasunori Tominaga, Aiko Fujiwara, and Yuko Amo. Dynamical structure of water by Raman spectroscopy. *Fluid Phase Equilibria*, 144(1-2):323–330, 1998.

[113] G. Varsanyi. *Assignments for vibrational spectra of seven hundred benzene derivatives.* Adam Hilger, 1974.

[114] M. Moskovits and Jung Sang Suh. Surface Geometry Change in 2-Naphthoic Acid Adsorbed on Silver. *The Journal of Physical Chemistry*, 92(22):6327–6329, 1988.

[115] Y J Kwon, D H Son, S J Ahn, M S Kim, and K Kim. Vibrational Spectroscopic Investigation of Benzoic-Acid Adsorbed on Silver. *Journal of Physical Chemistry*, 98:8481–8487, 1994.